AERODYNAMIC MODELING OF POST-STALL AND SPIN DYNAMICS OF LARGE TRANSPORT AIRPLANES

A Thesis
Presented to
The Academic Faculty

by

Austin Matthew Murch

In Partial Fulfillment
Of the Requirements for the Degree
Master of Science in Aerospace Engineering

Georgia Institute of Technology
August 2007

AERODYNAMIC MODELING OF POST-STALL AND SPIN DYNAMICS OF LARGE TRANSPORT AIRPLANES

Approved by:

Dr. Alan W. Wilhite, Advisor
School of Aerospace Engineering
Georgia Institute of Technology

Dr. Amy R. Pritchett
School of Aerospace Engineering
Georgia Institute of Technology

Dr. Eric N. Johnson
School of Aerospace Engineering
Georgia Institute of Technology

Date Approved: June 20th, 2007

ACKNOWLEDGEMENTS

Although only my name appears on the cover, there were many that made invaluable contributions during the course of this research. I would like to extend my thanks to all of those at NASA Langley Research Center who have taught me so much in the past two years. Specifically, I wish to thank my mentor John Foster for countless bits of advice and for reviewing and editing this thesis. I would also like to thank Kevin Cunningham for taking the time to sit through reviews of endless amounts of data. Thanks to Dan Murri for helping me begin my career as NASA researcher and for reviewing and editing this thesis. I wish to thank Mike Fremaux, Gene Adams, and Earl Harris for their skill and patience in conducting the free-spin test. Thanks to Gene Morelli for help with SIDPAC functions and post-processing of the free-spin data. I would also like to thank Lee Pollard for supplying and creating excellent graphics.

I would like to thank my thesis committee members at Georgia Tech, Dr. Alan Wilhite, Dr. Amy Pritchett, and Dr. Eric Johnson, for taking the time to be on my committee.

I would be remiss not to mention my family who has always supported me in my career ambitions and pursuit of higher education. I must also thank my lovely wife Melissa, who has endured my late nights at work and for trying to understand exactly what I have been trying to accomplish.

TABLE OF CONTENTS

Page

LIST OF TABLES

Page

LIST OF FIGURES

Page

NOMENCLATURE

α	angle of attack, degrees
$\dot{\alpha}$	time derivative of α
β	angle of sideslip, degrees
$\dot{\beta}$	time derivative of β
p_b	body-axis roll rate, degrees per second or radians per second
q_b	body-axis pitch rate, degrees per second or radians per second
r_b	body-axis yaw rate, degrees per second or radians per second
$\dot{p}_b$	body-axis roll acceleration, degrees per second^2 or radians per second^2
$\dot{q}_b$	body-axis pitch acceleration, degrees per second^2 or radians per second^2
$\dot{r}_b$	body-axis yaw acceleration, degrees per second^2 or radians per second^2
ϕ	Euler roll angle, degrees or radians
θ	Euler pitch angle, degrees or radians
ψ	Euler yaw angle, degrees or radians
$\dot{\phi}$	Euler roll rate, degrees per second or radians per second
$\dot{\theta}$	Euler pitch rate, degrees per second or radians per second
$\dot{\psi}$	Euler yaw rate, degrees per second or radians per second
$\ddot{\phi}$	Euler roll acceleration, degrees per second^2 or radians per second^2
$\ddot{\theta}$	Euler pitch acceleration, degrees per second^2 or radians per second^2
$\ddot{\psi}$	Euler yaw acceleration, degrees per second^2 or radians per second^2
X	aircraft lateral position in wind tunnel, feet

Y	aircraft lateral position in wind tunnel, feet
Z	aircraft vertical position in wind tunnel, feet
$\dot{X}$	aircraft lateral velocity in wind tunnel, feet per second
$\dot{Y}$	aircraft lateral velocity in wind tunnel, feet per second
$\dot{Z}$	aircraft vertical velocity in wind tunnel, feet per second
$\ddot{X}$	aircraft lateral acceleration in wind tunnel, feet per second^2
$\ddot{Y}$	aircraft lateral acceleration in wind tunnel, feet per second^2
$\ddot{Z}$	aircraft vertical acceleration in wind tunnel, feet per second^2
u_b	body-axis velocity along the *x*-axis, feet per second
v_b	body-axis velocity along the *y*-axis, feet per second
w_b	body-axis velocity along the *z*-axis, feet per second
$\dot{u}_b$	body-axis acceleration along the *x*-axis, feet per second^2
$\dot{v}_b$	body-axis acceleration along the *y*-axis, feet per second^2
$\dot{w}_b$	body-axis acceleration along the *z*-axis, feet per second^2
$\bar{\Omega}$	total angular rate, degrees per second
$\bar{\Omega}_{xz}$	projection of the total angular rate into the body-axis *xz*-plane, degrees per second
ω	wind-axis (velocity-vector) roll rate, degrees per second or radians per second
b	wingspan, feet
$\bar{c}$	mean aerodynamic chord, feet
V	airspeed, feet per second
$\hat{p}_b$	nondimensional body-axis roll rate, $\frac{p_b b}{2V}$

$\hat{q}_b$	nondimensional body-axis pitch rate, $\frac{q_b \bar{c}}{2V}$
$\hat{r}_b$	nondimensional body-axis yaw rate, $\frac{r_b b}{2V}$
p_{osc}	oscillatory component assigned to body-axis roll rate, degrees per second
q_{osc}	oscillatory component assigned to body-axis pitch rate, degrees per second
r_{osc}	oscillatory component assigned to body-axis yaw rate, degrees per second
$\bar{\Omega}_{osc}$	total oscillatory angular rate component, degrees per second
ω_{ss}	steady-state component assigned to wind-axis roll rate, degrees per second
$\hat{p}_{osc}$	nondimensional oscillatory roll rate component, $\frac{p_{osc} b}{2V}$
$\hat{q}_{osc}$	nondimensional oscillatory pitch rate component, $\frac{q_{osc} \bar{c}}{2V}$
$\hat{r}_{osc}$	nondimensional oscillatory yaw rate component, $\frac{r_{osc} b}{2V}$
$\hat{\omega}_{ss}$	nondimensional steady-state wind-axis roll rate component, $\frac{\omega_{ss} b}{2V}$
C_X	aerodynamic force coefficient along body x-axis
C_Y	aerodynamic force coefficient along body y-axis
C_Z	aerodynamic force coefficient along body z-axis
C_l	aerodynamic rolling moment coefficient about body x-axis
C_m	aerodynamic pitching moment coefficient about body y-axis
C_n	aerodynamic yawing moment coefficient about body z-axis

C_L	aerodynamic lift coefficient, in wind axes
C_D	aerodynamic drag coefficient, in stability axes
Δ	denotes increment
δ	control surface deflections: rudder, aileron, elevator
δ_r	rudder deflection, positive trailing edge left, degrees
δ_e	elevator deflection, positive trailing edge down, degrees
δ_{a_R}	right aileron deflection, positive trailing edge down, degrees
δ_{a_L}	left aileron deflection, positive trailing edge down, degrees
I_{xx}	moment of inertia about body *x*-axis, slug-ft^2
I_{yy}	moment of inertia about body *y*-axis, slug-ft^2
I_{zz}	moment of inertia about body *z*-axis, slug-ft^2
I_{xz}	moment of inertia about body *xz*-plane, slug-ft^2
X_{CG}	position of center of gravity along body *x*-axis, %MAC
Y_{CG}	position of center of gravity along body *y*-axis, %MAC
Z_{CG}	position of center of gravity along body *z*-axis, %MAC
m	mass, slug
$\mathbf{F}$	vector of body-axis forces, lbs
$\mathbf{M}$	vector of body-axis moments, lb-ft
$\mathbf{V}$	vector of body-axis velocities, feet per second
$\boldsymbol{\omega}$	vector of body-axis angular rates, radians per second
$\dot{\mathbf{V}}$	vector of body-axis accelerations, feet per second^2
$\dot{\boldsymbol{\omega}}$	vector of body-axis angular accelerations, radians per second^2
$\mathbf{I}$	matrix of body-axis moments of inertia, slug-ft^2

k	nondimensional oscillation frequency
A	oscillation amplitude, radians
$\bar{q}$	average dynamic pressure, pounds per square foot
V_T	corrected wind tunnel air velocity, feet per second
$\dot{V}_T$	time derivative of V_T, feet per second^2
V_{p-s}	wind tunnel velocity from pitot-static probe, feet per second
g	acceleration due to gravity, feet per second^2
L_{bT}	transformation matrix between the wind tunnel and aircraft body axes
$\dot{L}_{bT}$	time derivative of L_{bT}
CG	center of gravity, percent mean aerodynamic chord
DIR	direct resolution blending method
2D-KAL	2D Kalviste blending method
HY-KAL	Hybrid Kalviste blending method
EXRR	Excess Roll Rate blending method
FOO	forced oscillation only
RBO	rotary balance only
TED	trailing edge down
TEL	trailing edge left
RMS	root mean square
AoA	angle of attack, α
NASA	National Aeronautics and Space Administration
LaRC	Langley Research Center
SIDPAC	System IDentification Programs for AirCraft
DCM	direction cosine matrix

SUMMARY

This work addressed aerodynamic modeling methods for prediction of post-stall flight dynamics of large transport aircraft. This was accomplished by applying historically successful modeling methods used on high-performance military aircraft to a transport configuration. The overall research approach involved integrating forced oscillation and rotary balance wind tunnel data into an aerodynamic model using several methods of blending these data. The complete aerodynamic model was integrated into a six degree-of-freedom simulation. Experimental data from free-spin wind tunnel testing was used to validate the aerodynamic modeling methods by comparing aerodynamic force and moment coefficients and also to validate the simulation performance by comparing spin mode characteristics and time histories.

The aerodynamic model prediction of spin dynamics was generally very good using each of the blending methods. In addition, key spin mode characteristics were predicted with a high degree of accuracy. Overall, using the Hybrid Kalviste method of blending forced oscillation and rotary balance data produced the closest match to the free-spin data when comparing aerodynamic coefficients and spin mode characteristics.

Several issues with the blending methods were exacerbated by nonlinearities and asymmetries in the dynamic aerodynamic data. A new method of referencing dynamic aerodynamic data is proposed to address shortcomings in the blending methods and recommendations are provided for issues with the dynamic aerodynamic data.

CHAPTER 1

INTRODUCTION

Few events garner media attention and fuel public fears like commercial aviation accidents, largely due to the potential for catastrophic loss of life. The causes of such accidents have been separated into a number of categories, with in-flight loss-of-control recognized in the mid-1990s as the leading cause of fatal commercial aviation accidents[1]. Despite several research efforts focused on loss-of-control in the past decade[2,3,4,5], broadly applicable solutions have been elusive, and loss-of-control continues to be a leading cause of fatalities in commercial jet transport[6].

In the late 1990s the Commercial Aviation Safety Team identified simulation as one of several key intervention strategies for reducing the loss-of-control accident rate[7]. Simulations that are accurate outside of the normal flight envelope (e.g., for stall and post-stall flight) would enable realistic upset training, accident reconstruction, and advanced control system analysis. Joint NASA/Boeing studies found that the aerodynamic databases for large transport airplanes are insufficient for accurate prediction of the dynamic post-stall flight conditions often experienced during loss-of-control accidents[8,9]. In an effort to address this problem, research has been in progress as part of the NASA Aviation Safety Program to develop aerodynamic modeling methods for simulations that accurately predict the flight dynamics of large transport airplanes in upset conditions[10,11].

The traditional approach to developing accurate aerodynamic models for post-stall motions uses experimental data from static and dynamic wind tunnel tests. To be applicable to loss-of-control flight, wind tunnel test conditions must include the high wind angles and high angular rates often encountered in loss-of-control accidents. A series of such tests has been conducted at the NASA Langley Research Center using a generic commercial jet transport configuration[12]. Research performed under the NASA Aviation Safety Program has developed high-fidelity aerodynamic models for the stall regime that were effective in predicting stalls and some departure motions[10].

The focus of this thesis is on aerodynamic modeling of dynamic post-stall motions of large transport aircraft, including post-stall gyrations, incipient spins, and fully developed spins. While the likelihood of a large transport aircraft reaching a fully developed spin in flight is small, a spin is one of the few out-of-control flight motions that have readily obtainable validation data from free-spin wind tunnel testing as well as a number of analytical tools supported by significant prior research. Past experience with fighter aircraft also suggests that if the stall, departure, and spin regimes can be modeled successfully, most other loss-of-control motions can also be modeled well.

The goal of this thesis is to advance the state-of-the-art of aerodynamic modeling of dynamic post-stall motions of large transport aircraft so that loss-of-control motions can be better understood, enabling technology and practices that may contribute to reducing the fatal accident rate of large transport aircraft. To achieve this goal, modeling methods effective for modeling post-stall motions of high-performance aircraft were applied to a generic large transport configuration. A review of the traditional aerodynamic modeling practices for large transport aircraft and high-performance

military aircraft, in addition to a comparison of loss-of-control motion for these configurations, is presented in Chapter 2. These modeling methods were then used to create an aerodynamic model from experimental wind tunnel data that was implemented in a full six degree-of-freedom simulation. The aerodynamic modeling methods were then evaluated using experimental data from a free-spin wind tunnel test. A detailed description of this approach, the aerodynamic model structure, the free-spin test technique, and the validation process is given in Chapter 3. The results from this research are presented and discussed in Chapter 4, and a summary of conclusions and recommendations is given in Chapters 5 and 6.

CHAPTER 2

BACKGROUND

The traditional approach to aerodynamic modeling typically involves summation of static effects (e.g. angle of attack, control surface deflections) with dynamic effects (e.g. angular rate), the latter often referred to as rate damping effects. The desired range of validity for the aerodynamic model largely determines the required complexity and fidelity. Models range from simple linear functions to complex, nonlinear time-dependent algorithms.

Aerodynamic modeling of highly dynamic maneuvers such as post-stall gyrations, spins, and other out-of-control motions has been a research topic since the early days of aviation when Lindemann first analyzed the spin in 1916. In the past three decades, out–of-control motions have been successfully modeled for numerous high-performance military aircraft[13,14,15,16,17]. NASA studies[18] were a part of the general aviation aircraft modeling research in the 1980's that was motivated by stall/spin accidents. In the majority of studies, modeling the angular rate effects relied on two existing experimental test methods; oscillatory motion rigs (i.e. forced oscillation) and steady motion rigs (i.e. rotary balance).

However, loss-of-control motions often involve a combination of large amplitude, uncoordinated (i.e., the angular rate vector is not closely aligned with the velocity vector), and coupled motions which are difficult to replicate with traditional wind tunnel motion rigs. As a result, previous research has focused on methods to blend data from

oscillatory and steady motion rigs. Additional research has been aimed at development of new motion rigs designed to more closely simulate real flight motions.

The approach of this thesis was to apply effective modeling methods previously used on fighter aircraft to transport configurations. This chapter first compares the loss-of-control motions for a fighter aircraft and a large transport aircraft, highlighting similarities between the two. Section 2.2 then details the traditional aerodynamic modeling practices for transport aircraft and why they are inadequate for modeling post-stall motions. Finally, Section 2.3 describes the traditional aerodynamic modeling practices for fighter aircraft that were applied to the large transport configuration.

2.1 Comparison of Fighter and Transport Aircraft Loss-of-Control Motion

Experience with out-of-control flight motions of transport airplanes is very limited and it is unclear what sort of loss-of-control characteristics should be expected. Caution must be exercised when using information gleaned from past experience with fighter aircraft, as a NASA study has shown significant differences in dynamic wind tunnel test results between fighter and transport configurations[19]. Despite these differences, there are similarities between the flight data from loss-of-control motions of fighter aircraft[20] and a commercial transport[8], as shown in Table 2.1.

Table 2.1: Loss-of-control motions of fighter and transport aircraft.

Configuration	α_{max}	β_{max}	$\hat{p}_{max}$	$\hat{q}_{max}$	$\hat{r}_{max}$
Fighter	70°	45°	0.129	0.0062	0.043
Transport	47°	20°	0.126	0.0045	0.047

These data show that transport configurations can reach high post-stall wind incidence angles and high nondimensional rates during loss-of-control motions, a flight

condition often thought to be exclusive to fighter aircraft. This comparison indicates that the aerodynamic modeling methods that have been effective for modeling highly dynamic post-stall motions of high-performance aircraft may be effective at modeling similar motions of large transport aircraft. The following two sections describe the traditional modeling practices for large transports and high-performance aircraft.

2.2 Traditional Aerodynamic Modeling Approach for Large Transport Aircraft

A common practice used today for aerodynamic modeling for simulation of large transport aircraft is that static effects are normally based on wind tunnel measurements but prediction of the dynamic effects is usually accomplished using empirical methods or small-amplitude flight test maneuvers[8]. Simulation models of large transport flight behavior developed using this approach are therefore limited to the normal flight envelope below stall angles of attack. This limitation is strongly driven by the lack of certification requirements for flight outside of the normal flight envelope. A joint NASA/Boeing analysis of loss-of-control accidents[9] revealed that the normal flight envelope was often exceeded during loss-of-control accidents, and angles of attack well beyond stall were observed. Further simulation studies[8] have also shown that accurate modeling of angular rate effects for large transports had a significant effect on the predicted aircraft behavior. A key conclusion drawn from these studies was that *traditional aerodynamic models and simulations of large transport aircraft are not adequate for prediction of post-stall motions*.

2.3 Traditional Aerodynamic Modeling Approach for High-Performance Aircraft

The traditional approach to aerodynamic modeling for high-performance aircraft is to combine experimentally derived static and dynamic effects. Static effects are

modeled using standard static wind tunnel tests, while dynamic effects are typically modeled using forced oscillation and/or rotary balance tests. These dynamic tests are described in Section 2.3.1.

As noted previously, loss-of-control accidents often involve motion that is not represented well by either forced oscillation or rotary balance motion. One approach to addressing this issue is to combine the forced oscillation and rotary balance data sets based on the characteristics of aircraft motion. The underlying assumption in this approach is that data from two fundamentally different dynamic wind tunnel test motions can be combined vectorially to approximate arbitrary dynamic motion of aircraft. While this approach presents many challenges in terms of modeling and similitude requirements, several different blending methods using this vectorial technique have been used effectively on fighter aircraft in the past. Application of these methods to large transport configurations has been limited and was a motivating factor for this research. A description of blending methods is given in Section 2.3.2.

2.3.1 Dynamic Wind Tunnel Testing

Dynamic wind tunnel testing typically involves a similar model-strain gauge balance-sting setup found in static wind tunnel tests, except the entire apparatus is moved in some fashion. The standard dynamic tests are forced oscillation and rotary balance testing. Research has been in progress to develop advanced motion rigs (e.g., combined motion, a superposition of forced oscillation and rotary balance motion) that better emulate the complex nature of loss-of-control motions. This research utilized forced oscillation data taken in the NASA LaRC 14x22 Ft Wind Tunnel and rotary balance data taken in NASA LaRC 20 Ft Vertical Spin Tunnel.

2.3.1.1 Forced Oscillation Testing

Forced oscillation testing consists of moving the model in a sinusoidal fashion independently about each of the roll, pitch, and yaw axes. The angle of attack, amplitude, and frequency of the oscillation are all typically independent variables during the test. Additional variables may include sideslip angle, control surface deflections, and aircraft configuration.

Data from forced oscillation testing can be used in several ways. A common use is to derive the linear damping derivatives (e.g., C_{l_p}, C_{m_q}). Other data reduction methods seek to capture nonlinearities in angle of attack, frequency, amplitude, or nondimensional rate.

2.3.1.2 Rotary Balance Testing

Rotary balance testing usually consists of rotating the model at a steady rate about an axis parallel with the free-stream velocity vector. This type of motion is also called "coning". Typical independent parameters are the angle of attack, sideslip angle, and rotation rate, but may include control surface deflections and aircraft configuration. Angle of attack and sideslip angle are normally held constant during the rotation.

Rotary balance data is normally used for prediction of spin modes, as the rotary balance motion is very similar to a nonoscillatory steady spin, but can also be used to generate look-up tables of aerodynamic coefficient increments.

2.3.2 Description of Blending Methods

As neither forced oscillation nor rotary balance data fully represent the motions often experienced during loss-of-control, these data are often blended together in a way

that represents the overall aircraft motion. As illustrated in Figure 2.1, the most common blending approach is to partition the total angular rate vector ($\bar{\Omega}$) into a "steady-state" component (ω_{ss}) along the velocity vector (corresponding to rotary balance motion) and "oscillatory" components ($\bar{\Omega}_{osc}$) along the aircraft body axes (corresponding to forced oscillation motion). These components are then used with forced oscillation and rotary balance data to determine the total dynamic contribution to the aerodynamic forces and moments.

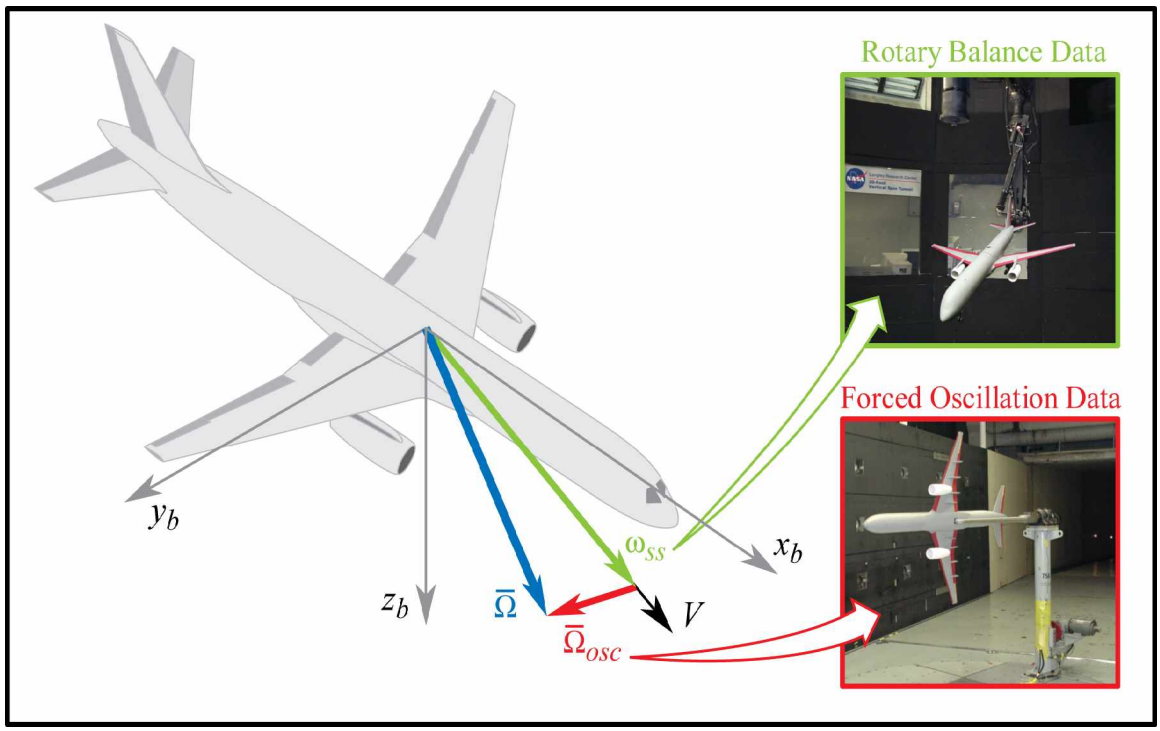

Figure 2.1: Decomposition of the total angular rate vector into steady state and oscillatory components.

The specific assignments of the steady and oscillatory rate components vary from method to method, and limitations have been noted for each. The most commonly used blending methods are the Direct Resolution method (DIR), the Hybrid Kalviste method

(HY-KAL), the 2D-Kalviste method (2D-KAL), the Excess Roll Rate method (EXRR), and using forced oscillation data only (FOO). Using rotary balance data only (RBO) is often used for modeling spins, but not for simulation of general aircraft motion. A brief description of each method used in this research is as follows:

2.3.2.1 Direct Resolution Method

Direct resolution is perhaps the simplest blending method[21]. The total angular rate vector is decomposed into the wind-axis roll rate (the steady-state component) and a residual component orthogonal to the velocity vector, which is further resolved into body-axis oscillatory components. This method is accurately depicted in Figure 2.1, and is implemented using the following equations:

$$\omega_{ss} = p_b \cos\alpha \cos\beta + q_b \sin\beta + r_b \sin\alpha \cos\beta \tag{2.1}$$

$$p_{osc} = p_b - \omega_{ss} \cos\alpha \cos\beta \tag{2.2}$$

$$q_{osc} = q_b - \omega_{ss} \sin\beta \tag{2.3}$$

$$r_{osc} = r_b - \omega_{ss} \sin\alpha \cos\beta \tag{2.4}$$

One issue with this method is the oscillatory roll and yaw components often have opposite signs of the corresponding body-axis roll and yaw rates. For highly uncoordinated maneuvers at higher angles of attack, this anomaly can be a significant problem as the forced oscillation data can be highly nonlinear and/or asymmetric with respect to angular rate.

2.3.2.2 Kalviste Methods

Since Kalviste's original formulation[22] (often called 3D Kalviste), at least two additional variants have been used; 2D Kalviste and Hybrid Kalviste. The latter two methods have seen the most use in recent years due to shortcomings of the original 3D Kalviste method, and were the only Kalviste methods used in this research. The 2D Kalviste and Hybrid Kalviste methods are similar, using the position of the angular rate vector relative to the velocity vector to determine the steady-state and oscillatory components.

The Kalviste methods use three possible cases, as illustrated in Figure 2.2.

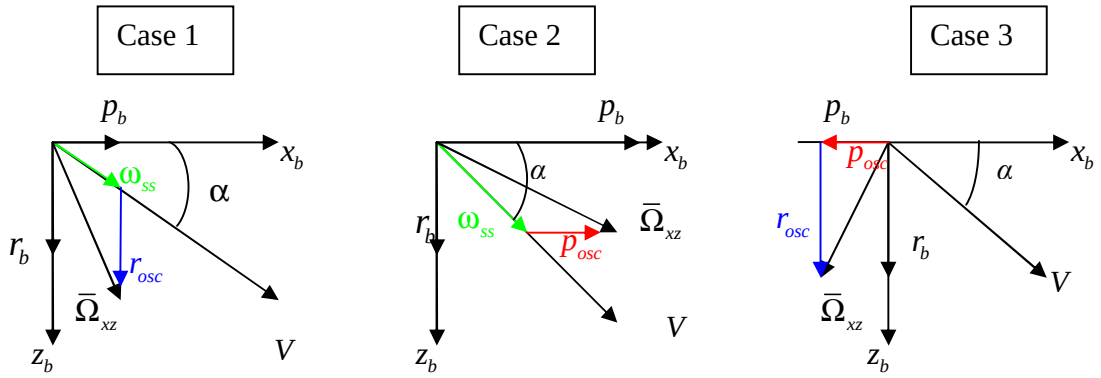

Figure 2.2: Three decomposition schemes used with the Kalviste methods.

In case 1, the projection of the total angular rate vector into the x-z plane ($\bar{\Omega}_{xz}$) is closer to the body *z*-axis, and is decomposed into a steady-state component and an oscillatory yaw component; the oscillatory roll component is not used. In case 2, the total angular rate vector is closer to the body *x*-axis, and is decomposed into a steady-state component and an oscillatory roll component; the oscillatory yaw component is not used. In case 3,

the angular rate is highly uncoordinated (roll and yaw have opposite signs), no steady-state component is used, and the method uses oscillatory components only.

The 2D and Hybrid methods differ only in the equations used to compute the various components. The Hybrid Kalviste method includes the effect of sideslip angle, while the 2D Kalviste method does not. The Hybrid Kalviste equations are given in Table 2.2.

Table 2.2: Equations used in the Hybrid Kalviste method.

Angular RateTerm	Case 1	Case 2	Case 3
$\omega_{ss} =$	$\frac{p_b}{\cos\alpha \cos\beta}$	$\frac{r_b}{\sin\alpha \cos\beta}$	0
$p_{osc} =$	0	$p_b - \omega_{ss} \cos\alpha \cos\beta$	p_b
$q_{osc} =$	$q_b - \omega_{ss} \sin\beta$	$q_b - \omega_{ss} \sin\beta$	q_b
$r_{osc} =$	$r_b - \omega_{ss} \sin\alpha \cos\beta$	0	r_b

The 2D Kalviste equations can be obtained by setting the sideslip angle equal to zero in the Hybrid Kalviste equations, and are shown in Table 2.3.

Table 2.3: Equations used in the 2D Kalviste method.

Angular Rate Term	Case 1	Case 2	Case 3
$\omega_{ss} =$	$\frac{p_b}{\cos\alpha}$	$\frac{r_b}{\sin\alpha}$	0
$p_{osc} =$	0	$p_b - \omega_{ss} \cos\alpha$	p_b
$q_{osc} =$	q_b	q_b	q_b
$r_{osc} =$	$r_b - \omega_{ss} \sin\alpha$	0	r_b

Previous research efforts[14] found the Kalviste methods to be sensitive to slightly uncoordinated maneuvers at very high angles of attack, which can cause the method to abruptly switch to using forced oscillation data only (i.e. Case 3). Due to the lower magnitude of angles of attack experienced with transports, this sensitivity was not expected in this research.

2.3.2.3 Excess Roll Rate Method

The Excess Roll Rate method[14] does not use an oscillatory yaw component at any time. This method is identical to Case 2 of the Hybrid Kalviste method (see Figure 2.2) and uses the same equations, which are repeated below for clarity.

$$\omega_{ss} = \frac{r_b}{\sin\alpha \cos\beta} \tag{2.5}$$

$$p_{osc} = p_b - \omega_{ss} \cos\alpha \cos\beta \tag{2.6}$$

$$q_{osc} = q_b - \omega_{ss} \sin\beta \tag{2.7}$$

$$r_{osc} = 0 \tag{2.8}$$

This approach was intended to model roll rate-dominated motions and avoids complexities associated with using yaw forced oscillation data. One significant drawback of this method is the presence of a singularity at $\alpha = 0°$, which necessitates a different approach at low angles of attack. For this research, the Hybrid Kalviste method was used if the angle of attack was less than 15°.

2.3.2.4 Forced Oscillation Method

This method uses only forced oscillation data; no rotary balance data is used. The nondimensional body-axis angular rates are used directly with the forced oscillation database. The relevant equations are listed below.

$$\omega_{ss} = 0 \tag{2.9}$$

$$p_{osc} = p_b \tag{2.10}$$

$$q_{osc} = q_b \tag{2.11}$$

$$r_{osc} = r_b \tag{2.12}$$

Previous research on blending methods used for high-performance aircraft found that using forced oscillation data alone was not adequate to model highly dynamic post-stall motions[13,14].

2.3.2.5 Rotary Balance Method

This method uses only rotary balance data; no forced oscillation data is used. The steady wind-axis roll rate is calculated via Equation (2.13), nondimensionalized, and used directly with the rotary balance database. The relevant equations are listed below.

$$\omega_{ss} = p_b \cos\alpha \cos\beta + q_b \sin\beta + r_b \sin\alpha \cos\beta \tag{2.13}$$

$$p_{osc} = 0 \tag{2.14}$$

$$q_{osc} = 0 \tag{2.15}$$

$$r_{osc} = 0 \tag{2.16}$$

This method is not viable for six degree-of-freedom simulation of the complete range of aircraft dynamic motion, but should provide good results for nonoscillatory spin motions, which are nearly identical to the rotary balance test motion.

CHAPTER 3

APPROACH

3.1 Overall Research Approach

The overall approach of this thesis was to apply modeling methods used to successfully predict out-of-control motions of fighter aircraft to a transport aircraft configuration and use these methods to model spins. This was done by creating an aerodynamic model using static wind tunnel test data and blending together forced oscillation and rotary balance wind tunnel test data via the blending methods discussed in Section 2.3.2. The aerodynamic model structure is described in Section 3.2. This aerodynamic model was then implemented into a MATLAB/Simulink-based simulation that was used to simulate incipient and fully developed spins. A description of the simulation is given in Section 3.3. Finally, the modeling methods were validated using data from a free-spin wind tunnel test, described in Section 3.4. The aerodynamic model was compared to the computed aerodynamic coefficients and the simulated spin characteristics were compared to the free-spin data. The validation procedure is discussed in Section 3.5.

3.2 Description of the Aerodynamic Model

3.2.1 Aerodynamic Model Structure

The aerodynamic model consists of a summation of static and dynamic effects derived from wind tunnel test data. The model is constructed using six degree-of-freedom nondimensional force and moment coefficients arranged in lookup tables. The overall model functionality is given by

$$C_i = C_i\left(\alpha, \beta, \delta, \hat{p}_{osc}, \hat{q}_{osc}, \hat{r}_{osc}, \hat{\omega}_{ss}\right) \tag{3.1}$$

where $i = X, Y, Z, l, m, n$. The model is broken into a summation of a baseline static coefficient and increments for control surface deflections and dynamic effects, summarized below.

$$\begin{aligned} C_i = {} & C_{i,Static}\left(\alpha, \beta\right) + \Delta C_{i,\delta}\left(\alpha, \beta, \delta\right) \\ & + \Delta C_{i,\hat{q}_{osc}}\left(\alpha, \hat{q}_{osc}\right) + \Delta C_{i,\hat{\omega}_{ss}}\left(\alpha, \beta, \hat{\omega}_{ss}\right) \end{aligned} \tag{3.2}$$

where $i = X, Z, m$ and δ includes elevator, aileron, and rudder deflections, and

$$\begin{aligned} C_j = {} & C_{j,Static}\left(\alpha, \beta\right) + \Delta C_{j,\delta}\left(\alpha, \beta, \delta\right) \\ & + \Delta C_{j,\hat{p}_{osc}}\left(\alpha, \hat{p}_{osc}\right) + \Delta C_{j,\hat{r}_{osc}}\left(\alpha, \hat{r}_{osc}\right) + \Delta C_{j,\hat{\omega}_{ss}}\left(\alpha, \beta, \hat{\omega}_{ss}\right) \end{aligned} \tag{3.3}$$

where $j = Y, l, n$ and δ includes aileron and rudder deflections.

3.2.2 Aerodynamic Model Databases

Each term in the aerodynamic model (Equations (3.2) and (3.3)) has a database that is arranged in an *n*-dimensional lookup table, where *n* is equal to the number of independent variables for that term. Linear interpolation was used to compute the coefficient increment for values of the independent variables that were between table breakpoints, while linear extrapolation was used for values outside of the table breakpoints.

3.2.2.1 Static Database

The static database was created in previous modeling research under the NASA Aviation Safety Program from data taken in the NASA LaRC 14x22 Ft Wind Tunnel using a 5.5% scale model, shown in Figure 3.1.

Figure 3.1: 5.5% model in the NASA LaRC 14x22 Ft Wind Tunnel.

The database is a function of angle of attack and sideslip angle, which span the following ranges:

$$\alpha = \left[-5^{\circ}, 85^{\circ} \right] \tag{3.4}$$

$$\beta = \left[-45^{\circ}, 45^{\circ} \right] \tag{3.5}$$

The side force, rolling moment, and yawing moment coefficients were made symmetric with respect to sideslip angle. While asymmetries in these coefficients are often real, they are difficult to model and are beyond the scope of this research.

3.2.2.2 Control Deflections Database

The database of control effects was created in previous modeling research under the NASA Aviation Safety Program from data taken in the NASA LaRC 14x22 Ft Wind Tunnel using a 5.5% scale model (see Figure 3.1). The database is also a function of angle of attack and sideslip angle, spanning the same range as the static database described in the previous section. The aileron effects are assumed to be symmetric, as only one aileron was moved during wind tunnel testing. Likewise, the rudder effects are assumed to be symmetric as only left deflections were tested in the wind tunnel. The physical limits of the control deflections are:

$$\delta_{e,\,\text{Limits}} = -30^{\circ} / +20^{\circ} \tag{3.6}$$

$$\delta_{a_L,\,\text{Limits}} = \delta_{a_R,\,\text{Limits}} = \pm 20^{\circ} \tag{3.7}$$

$$\delta_{r,\,\text{Limits}} = \pm 30^{\circ} \tag{3.8}$$

3.2.2.3 Forced Oscillation Database

The forced oscillation database was developed as part of this research from data taken in the NASA LaRC 14x22 Ft Wind Tunnel using a 5.5% scale model on an oscillation rig, shown in Figure 3.2.

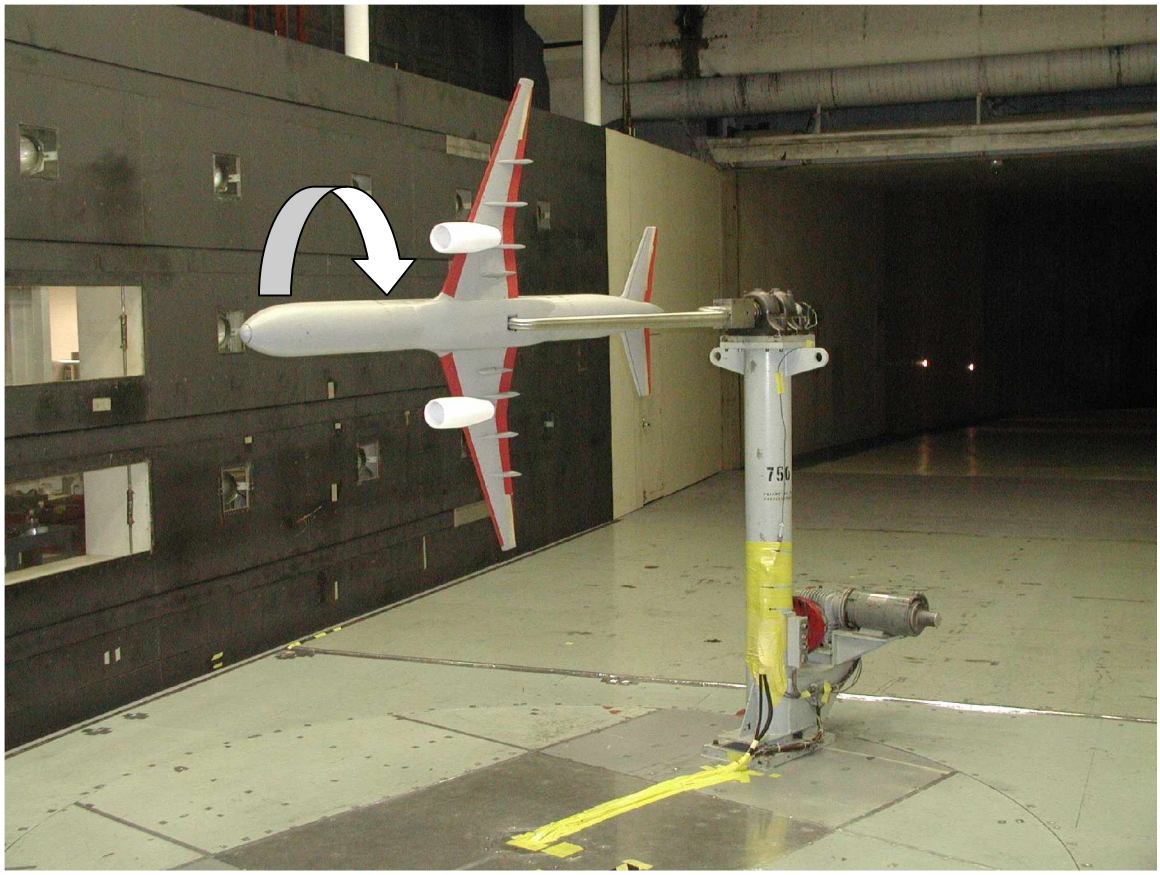

Figure 3.2: 5.5% model on roll forced oscillation rig, NASA LaRC 14x22 Ft Tunnel.

This data is associated with the $\hat{p}_{osc}$, $\hat{q}_{osc}$, and $\hat{r}_{osc}$ terms in Equations (3.2) and (3.3). A separate database was created for each of the roll, pitch, and yaw axes as a function of angle of attack and nondimensional rate. The limits of each database are as follows:

Roll Axis:

$$\alpha = \left[-10^{\circ}, 90^{\circ}\right] \tag{3.9}$$

$$\hat{p}_{osc} = \left[-0.107, 0.107\right] \tag{3.10}$$

Pitch Axis:

$$\alpha = \left[-30^{\circ}, 50^{\circ}\right] \tag{3.11}$$

$$\hat{q}_{osc} = \left[-0.0075, 0.0075\right] \tag{3.12}$$

Yaw Axis:

$$\alpha = \left[-30^{\circ}, 60^{\circ}\right] \tag{3.13}$$

$$\hat{r}_{osc} = \left[-0.112, 0.112\right] \tag{3.14}$$

The incremental databases were created by subtracting the static value of the appropriate coefficient at the same angle of attack from the forced oscillation data, e.g., for the pitch forced oscillation pitching moment coefficient:

$$\Delta C_{m,\hat{q}_{osc}}\left(\alpha_j, \hat{p}_{osc}\right) = C_{m,\hat{q}_{osc}}\left(\alpha_j, \hat{q}_{osc}\right) - C_{m,\hat{q}_{osc}}\left(\alpha_j, \hat{q}_{osc} = 0\right) \tag{3.15}$$

Note that, for the rolling moment, yawing moment, and side force coefficients, the static (i.e. zero rate) coefficient value was assumed to be zero, as expected for a symmetric aircraft. However, this is not always the case due to aerodynamic asymmetries, a difficulty encountered with the rotary balance data. Appendix A gives more detail on the creation of these databases.

3.2.2.4 Rotary Balance Database

The rotary balance database was developed as part of this research from data taken in the NASA LaRC 20 Ft Vertical Spin Tunnel using a 3.5% scale model on a rotating balance, shown in Figure 3.3.

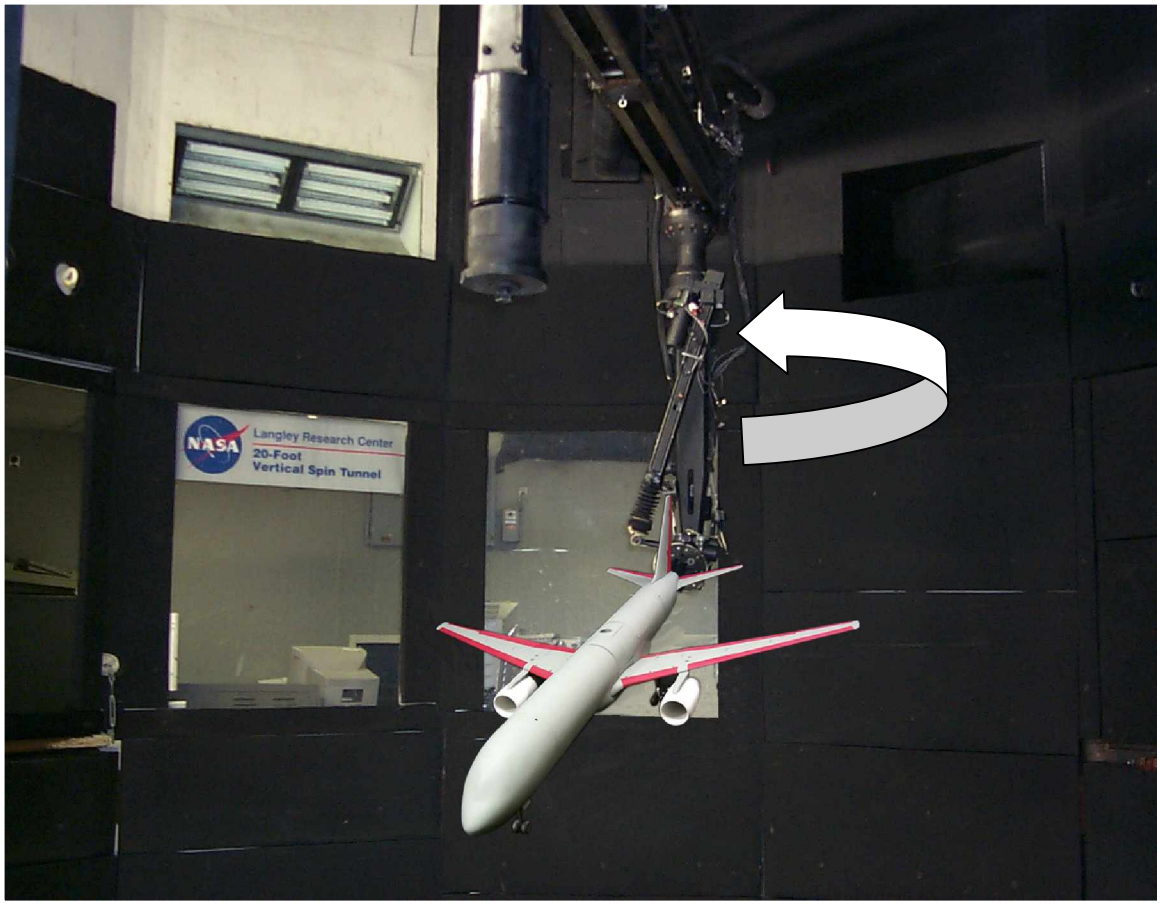

Figure 3.3: 3.5% model on rotary balance rig, NASA LaRC 20 Ft Vertical Spin Tunnel.

The rotary balance data is associated with the $\hat{\omega}_{ss}$ term in Equations (3.2) and (3.3). The database is a function of angle of attack, sideslip angle, and nondimensional angular rate, spanning the following ranges:

$$\alpha = \left[0^{\circ}, 90^{\circ}\right] \tag{3.16}$$

$$\beta = \left[-40^{\circ}, 40^{\circ}\right] \tag{3.17}$$

$$\hat{\omega}_{ss} = \left[-0.5, 0.5\right] \tag{3.18}$$

The incremental database was created by subtracting the zero-rate coefficient value (i.e., the static value) at a particular angle of attack and sideslip angle from the non-zero rate

coefficient values at that same angle of attack and sideslip angle. In equation form, using rolling moment as an example, this process is simply

$$\Delta C_l\left(\alpha_i, \beta_j, \hat{\omega}_{ss}\right) = C_l\left(\alpha_i, \beta_j, \hat{\omega}_{ss}\right) - C_l\left(\alpha_i, \beta_j, \hat{\omega}_{ss} = 0\right) \tag{3.19}$$

Difficulties can arise with this method when there are asymmetries present in the static data. The database was not made symmetric with respect to angular rate or sideslip angle. Appendix A gives more detail on the creation of this database.

3.3 MATLAB/Simulink Simulation

The aerodynamic model described in Section 3.2 was implemented into a MATLAB/Simulink-based batch simulation. Fourth order Runge-Kutta was used for integration with a fixed timestep of 0.00667 sec (150 Hz).

3.3.1 Simulation of Spins

Several approaches were used to simulate spins. The first approach was to initialize the simulation at an angle of attack beyond stall and then apply pro-spin control inputs. A second approach attempted to simulate the free-spin test conditions by initializing the simulation at a high angle of attack and with an initial rotation rate. The goal of both approaches was to determine if a developed spin mode could be reached with a particular set of control inputs. Spin modes predicted from rotary balance data analysis were used as a starting point for both approaches. If a developed spin mode was attained, data describing the characteristics of the mode were recorded, including average values of angle of attack, sideslip angle, velocity, and spin rate. Also important is the oscillatory character of the spin; however, a standardized method for quantifying the oscillatory characteristics of a spin does not exist. For this research, the root mean square

(RMS) deviation about the mean of each parameter was used to quantify the oscillatory character of the spin.

3.4 Aerodynamic Model Validation

Validation is a very important part of any aerodynamic modeling activity. Aerodynamic models are often validated by comparing the model outputs and/or simulation time histories to flight test data. Validation of aerodynamic models of transport aircraft in the post-stall regime presents several unique challenges. First, full-scale flight test data is severely limited due to the unacceptable flight safety risks involved in acquiring these data. Second, precise simulator time history matching is unrealistic for nonlinear, coupled, long-duration motions such as spins. To address these challenges, validation data was obtained from free-spin testing of a dynamically-scaled model. This data was used to validate the aerodynamic modeling methods using three methods and the validation results are presented in Chapter 4:

1. The appropriate motion parameters from the free-spin test were input into the aerodynamic model and the outputs were compared with the aerodynamic coefficients extracted directly from the free-spin test data. This method offers the most direct validation of the aerodynamic model as a whole; unfortunately, the free-spin test technique cannot provide validation for the individual terms of each aerodynamic coefficient.
2. Simulation time histories were compared to free-spin time histories to verify the general characteristics of the motion. The intent was not to precisely match the free-spin time histories, but to verify the simulation captured the general orientation and oscillatory nature of the spin.

3. Simulated spin modes were compared to the spin modes obtained in the free-spin test. The spin mode characteristics compared included the average values of angle of attack, sideslip angle, spin rate, and velocity, as well the RMS deviation about the mean of each parameter as means to describe the degree of oscillation.

3.5 Free-Spin Wind Tunnel Testing

The free-spin testing for this research was conducted in the NASA LaRC 20 Ft Vertical Spin Tunnel, a closed-return tunnel which has a vertical 20-foot diameter test section with a near-infrared digital photogrammetry data system. Maximum test velocity is ~85 feet/sec. Tests were conducted using a 1/49th dynamically-scaled model, shown in Figure 3.4.

Figure 3.4: 1/49th dynamically-scaled free-spin model.

3.5.1 Free-Spin Test Technique

The free-spin test technique involves hand-launching an uninstrumented dynamically-scaled model into a vertically rising airstream at a high angle of attack and rotation rate. The model will typically enter a stable spin mode if one or more exist for the given configuration and control surface deflections. The test is terminated via remote control surface actuation, deployment of a spin chute, or stopping the airstream.

3.5.1.1 Model Construction and Ballasting

The free-spin models are constructed out of polyethylene using rapid-prototyping manufacturing techniques. This method has the advantage of rapid production and repair, but the models are more fragile than traditional fiberglass models. The model is normally fitted with servos and radio control equipment for applying spin recovery inputs. The body axis moments of inertia, I_{xx}, I_{yy}, and I_{zz}, are measured on a swing rig (I_{xz} is not measured). Ballast is then added in appropriate positions and amounts to adjust the model weight and inertias to meet dynamic scaling targets.

Two models were used in the free-spin test. Table 3.1 details the weights, moment of inertia loadings ("swings"), and CG positions used during the test and the corresponding dynamically scaled targets.

Table 3.1: Free-spin model weights and inertia loadings

Model #	Target	1	2	2
Swing	-	9	2	4
Weight, lbs	3.19	3.27	3.21	3.17
I_{xx} **, slg-ft^2**	0.0118	0.0117	0.0119	0.0118
I_{yy} **, slg-ft^2**	0.0378	0.0381	0.038	0.0388
I_{zz} **, slg-ft^2**	0.0484	0.0482	0.0482	0.0486
X_{CG} **, %MAC**	-	15.15	15.02	25.07
Y_{CG} **, %MAC**	0	0.3	-0.11	0.32
Z_{CG} **, %MAC**	0	-5.4	-7.27	-7.06

3.5.1.2 Use of a Tether During Testing

A lightweight tether is often attached to the model during preliminary testing to prevent the model from impacting the tunnel wall if the model does not enter or remain in a stable spin mode. If the spin modes obtained are stable enough, the tether will be removed. For this test, the only spin mode obtained was a steep, oscillatory mode which was difficult to reach and sustain, requiring the tether to remain attached for the entire test. To minimize the effect of the tether, data was only used when the model was within a prescribed test volume in the wind tunnel. This volume is approximately enclosed by the red dashed line around the model in Figure 3.5. The dimensions were selected by observing video of the free-spin test and noting the tether was noticeably slack when the model was approximately within 9 feet of the tether ring and within 6 feet of the tunnel centerline.

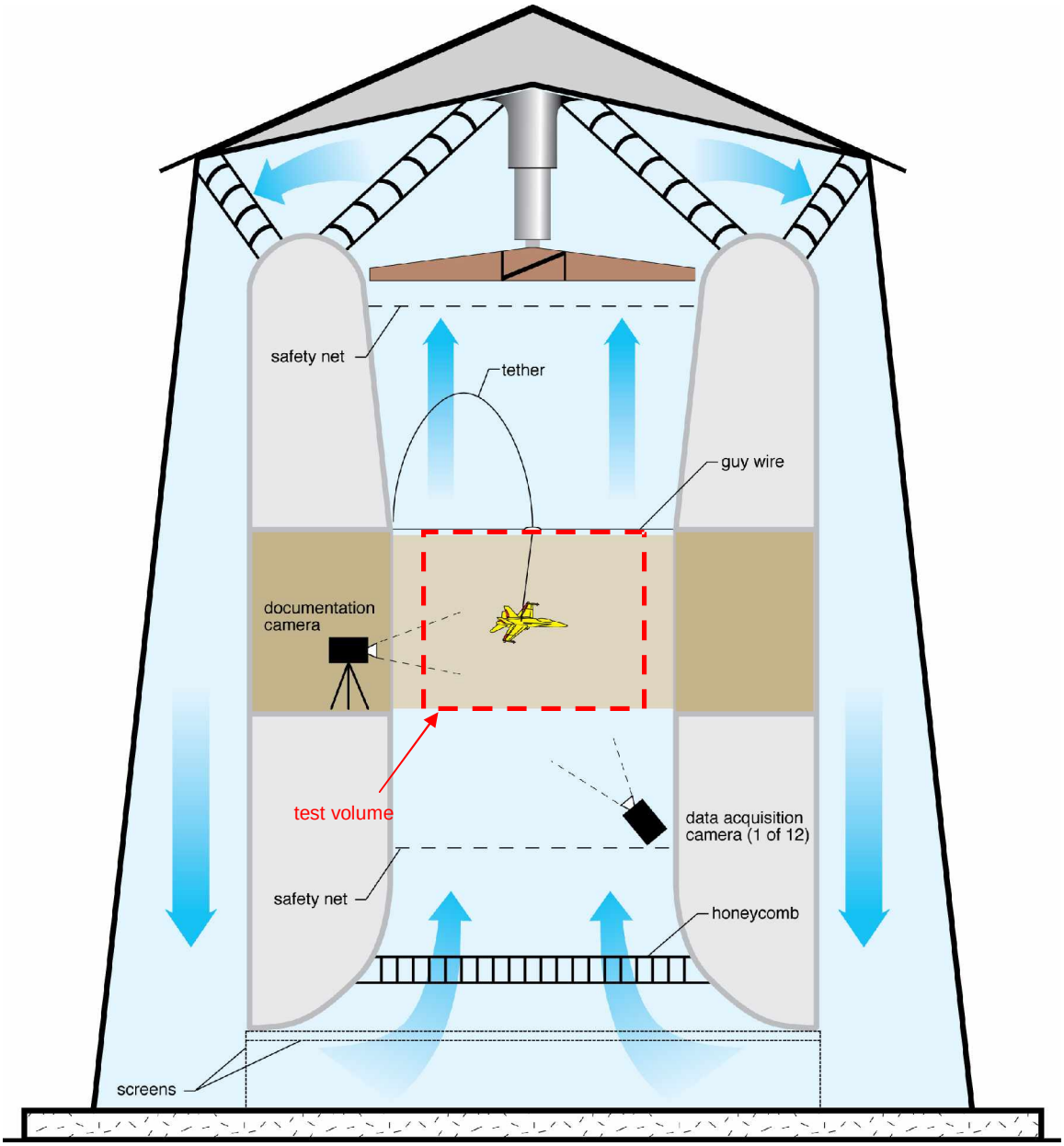

Figure 3.5: Diagram of free-spin test in the NASA LaRC 20 Ft Vertical Spin Tunnel.

Figure 3.6 and Figure 3.7 show a sample free-spin time history of the distance between the model and tether ring as well as the distance between the model and the centerline of the tunnel. The red dashed lines indicate the 9 foot and 6 foot boundaries; free-spin data was considered valid only when the model was within these boundaries.

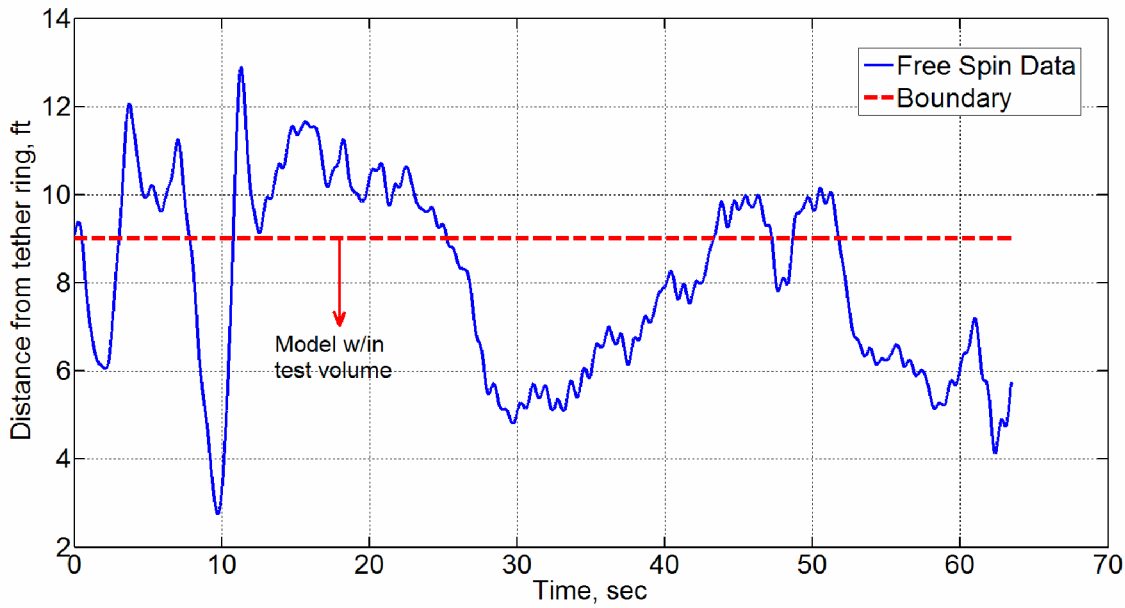

Figure 3.6: Model distance from tether ring during a free-spin test run.

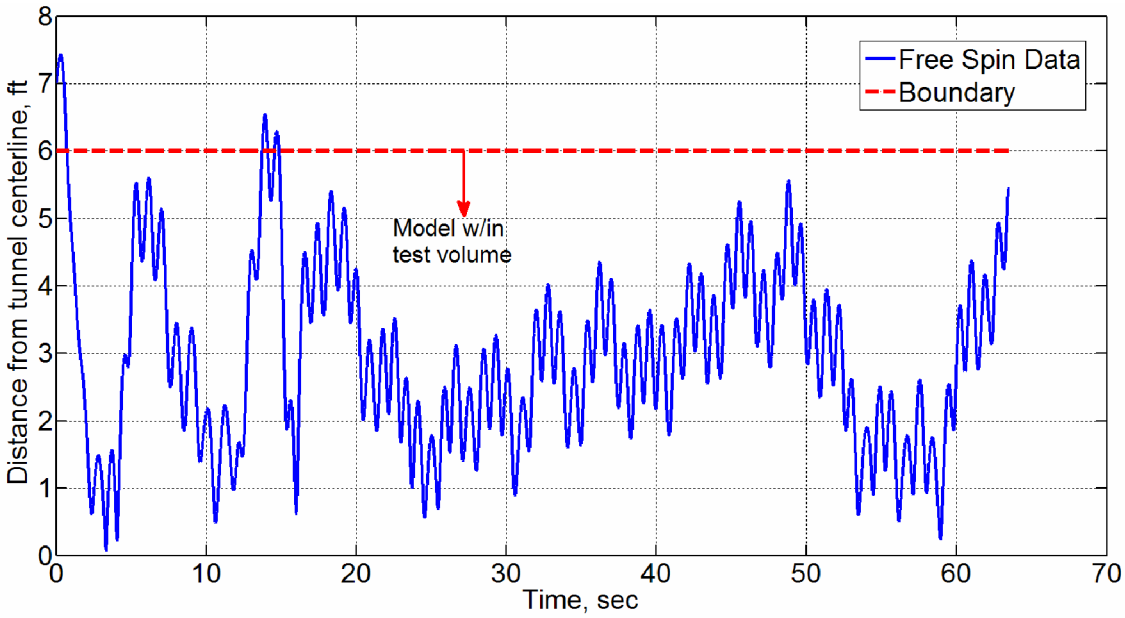

Figure 3.7: Model distance from centerline of tunnel during a free-spin test run.

Figure 3.8 shows a sample pitch angle time history with the useable data denoted by the shaded regions. Only portions of these data were selected for validating the aerodynamic model and simulation.

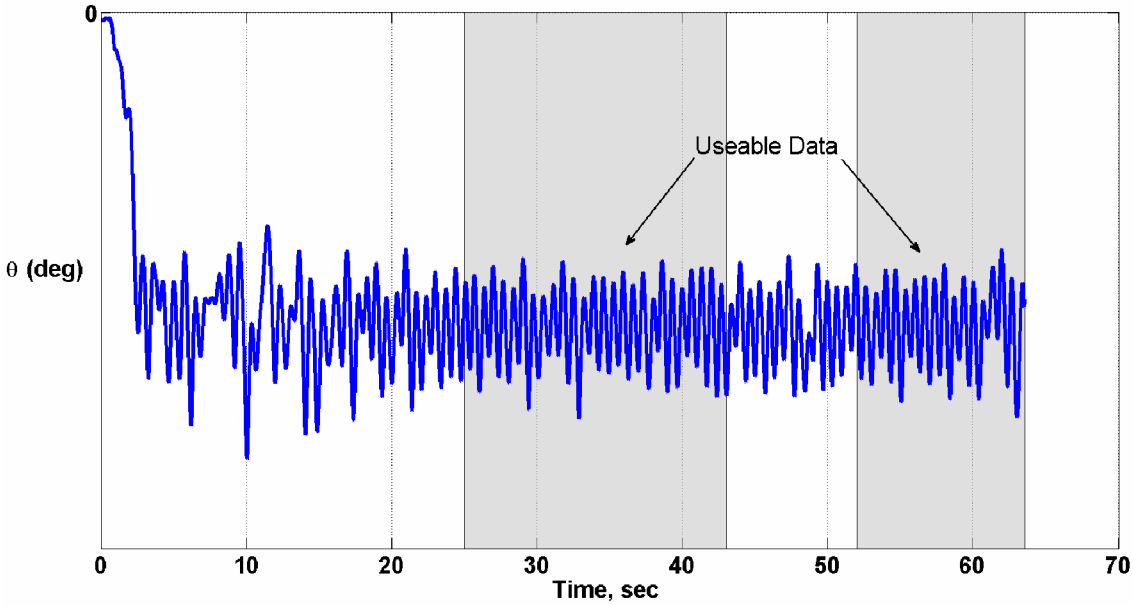

Figure 3.8: Sample free-spin time history of pitch angle showing useable data.

3.5.1.3 Reynold's Number Considerations

Reynold's number effects are often a concern when comparing free-spin test results to other data. For this research, the free-spin results were compared to other relatively low Reynold's number subscale data. Table 3.2 shows the Reynold's numbers based on mean aerodynamic chord and fuselage diameter for the free-spin test compared to the static, forced oscillation, and rotary balance tests, as well as full-scale.

Table 3.2: Reynold's number for subscale wind tunnel tests and full-scale aircraft

Test	Scale	Reynold's Number (MAC), 10^6	Reynold's Number (Fuselage Dia.), 10^6
Free-spin	2.041%	0.127	0.0940
Rotary balance	3.5%	0.107	0.0792
Forced oscillation	5.5%	0.533	0.395
Static	5.5%	0.533	0.395
Full-scale	100%	24.1	17.9

Any Reynold's number effects between the subscale tests are likely to be minimal since the Reynold's numbers of these data are fairly similar. Reynold's number effects on airplanes during a spin primarily relate to the point where the flow separates from the wing and/or fuselage, and consequently are largely configuration dependent. Prior research[23],[24] has found Reynold's number effects to generally be the strongest for squared fuselage, thick airfoil, straight wing configurations (i.e. general aviation aircraft) and relatively minimal for sharp-nosed, swept wing, thin airfoil configurations (i.e. military fighter aircraft). In terms of these descriptors, the transport configuration tested is essentially between a fighter configuration and a general aviation configuration, so further research is recommended to address the applicability of the subscale test data to full-scale aircraft.

3.5.2 Free-Spin Data System

Data collected during the free-spin test includes position and Euler angle data gathered via a near-infrared digital photogrammetry system. This system uses a group of eight near-infrared digital cameras located on the lower walls of the vertical tunnel that track the position and orientation of the model via reflective markers that are placed on the lower surfaces of the model fuselage, wings, nose, and tail. Data is collected at 150 Hz.

In addition, four digital video cameras located on the lower walls of the tunnel as well as one additional camera located in the control room record the test. Tunnel velocity data is measured via a pitot-static sensor in the tunnel and is synchronized with the position and orientation data. The tunnel velocity is an analog signal that is taken at 1

Hz, which is then sampled at 150 Hz in order to synchronize this signal with the position and orientation data.

3.5.3 Free-Spin Data Post-Processing

The position, orientation, and tunnel velocity data obtained during the free-spin test can be used to calculate all of the relevant aircraft motion parameters and aerodynamic coefficients. Position and Euler angle data is smoothed using optimal global Fourier smoothing, which removes all portions of the data above a selected frequency. The data can then be numerically differentiated to obtain velocities and accelerations in the tunnel reference frame. By assuming the tunnel airstream is exactly vertical (i.e., along the tunnel *z*-axis), body-axis velocities, accelerations, and wind angles can be calculated. The total forces and moments can be calculated using the standard rigid-body equations of motion for an aircraft. Assuming a flat, nonrotating earth, constant mass properties, these equations (written in body-axes) are given by

$$\mathbf{F} = m\dot{\mathbf{V}} + \boldsymbol{\omega} \times m\mathbf{V} \tag{3.20}$$

$$\mathbf{M} = \mathbf{I}\dot{\boldsymbol{\omega}} + \boldsymbol{\omega} \times \mathbf{I}\boldsymbol{\omega} \tag{3.21}$$

Each term on the right-hand side of Equations (3.20) and (3.21) is either measured or can be calculated. The only forces and moments acting on the body are assumed to be gravity and aerodynamics, so the aerodynamic force and moment coefficients can then be calculated. Appendix A contains the detailed derivation for this process.

3.5.4 Free-Spin Test Plan

A simulation study of spin entries with varying control inputs and CG locations was conducted prior to the free-spin test in order to guide the test planning. This activity identified control inputs and configurations that were not likely to produce a developed

spin or would be unattainable during the free-spin test. Theoretically, any developed spin mode with a spin radius and steady airspeed within the tunnel constraints could be achieved during testing. In practice, extremely steep spin modes are difficult to obtain due the corresponding high test velocity, which also greatly increases the possibility of model damage.

Simulation testing and rotary balance analysis identified two primary spin modes, a steep oscillatory mode and a very steep nonoscillatory mode. Although the very steep nonoscillatory mode was not likely to be achieved in the free-spin test, the configurations leading to the mode were attempted. Table 3.3 describes the control inputs and CG positions used in the free-spin test and the corresponding result of simulation tests. A list of the successful test points is given in Chapter 4.

Table 3.3: Free-spin test matrix.

Block	CG, % MAC	Rudder, +TEL	L Aileron, +TED	R Aileron, +TED	Elevator, +TED	Simulation Outcome
23	15	0°	0°	0°	0°	No Spin
25	15	30°	0°	0°	0°	Oscillatory spin
26	15	30°	0°	0°	-30°	Oscillatory spin
27	15	30°	0°	0°	20°	Oscillatory spin
28	15	30°	20°	-20°	0°	Oscillatory spin
29	15	30°	0°	0°	0°	Oscillatory spin
30	15	-30°	0°	0°	0°	Oscillatory spin
31	15	-15°	0°	0°	0°	Oscillatory spin
32	15	-30°	20°	-20°	0°	Nonoscillatory spin
33	15	30°	-20°	20°	0°	Nonoscillatory spin
34	15	15°	0°	0°	0°	Oscillatory spin
35	15	-30°	-20°	20°	0°	Oscillatory spin
36	25	30°	0°	0°	0°	Oscillatory spin
37	25	-30°	0°	0°	0°	Oscillatory spin
38	25	30°	0°	0°	-30°	Oscillatory spin
39	25	30°	0°	0°	20°	Oscillatory spin
40	25	30	20°	-20°	0°	Oscillatory spin
41	25	30	-20°	20°	0°	Nonoscillatory spin
42	25	-30	20°	-20°	0°	Nonoscillatory spin

CHAPTER 4

RESULTS

This chapter details the results of this research. The results from the free-spin testing are given in Section 4.1. Selected test results are then compared to the aerodynamic model using coefficient matching in Section 4.2. Finally, Section 4.3 compares the free-spin data to simulation results.

4.1 Free-Spin Test Results

Nearly all of the test points outlined in Section 3.5.4 were attempted in the free-spin test. However, not all of the test points reached a stable spin mode. Some configurations were too oscillatory to stabilize and others simply never developed into a spin. Others still had poor data due to being near the sides of the tunnel or hanging on the tether low in the tunnel. Table 4.1 lists the configurations where a developed spin was obtained and the recorded data was of acceptable quality. Each data set is labeled using "bXXrXX" format, where "bXX" denotes the test "block" or configuration, and "rXX" denotes the run number for that test block.

Table 4.1: Free-spin test results.

Run	Model & Swing	CG, %MAC	Rudder, +TEL	L/R Aileron, +TED	Elevator, +TED	Outcome
b25r4	m1s9	15.15	30°	0°	0°	Oscillatory spin
b27r5	m1s9	15.15	30°	0°	20°	Oscillatory spin
b27r9	m1s9	15.15	30°	0°	20°	Oscillatory spin
b29r11	m2s2	15.02	30°	0°	0°	Oscillatory spin
b32r2	m2s2	15.02	-30°	+20°/-20°	0°	Oscillatory spin
b33r4	m2s2	15.02	30°	-20°/+20°	0°	Oscillatory spin
b34r7	m2s2	15.02	15°	0°	0°	Oscillatory spin
b36r9	m2s4	25.07	30°	0°	0°	Oscillatory spin
b36r12	m2s4	25.07	30°	0°	0°	Oscillatory spin
b38r5	m2s4	25.07	30°	0°	-30°	Oscillatory spin
b42r7	m2s4	25.07	-30°	+20°/-20°	0°	Oscillatory spin
b42r9	m2s4	25.07	-30°	+20°/-20°	0°	Oscillatory spin

Runs b27r5, b29r11, b32r2, and b36r9 were selected to be used for coefficient matching based on the quality of the data and the configurations represented.

4.2 Aerodynamic Coefficient Matching

In this section, the output of the aerodynamic model using various blending methods will be compared to aerodynamic coefficients extracted from free-spin data. Numerical values for coefficient data are suppressed due to proprietary data restrictions.

4.2.1 Rolling Moment Coefficient

This section shows comparisons of the rolling moment coefficient between the free-spin data and the aerodynamic model using various blending schemes. Figure 4.1 shows a 6 second portion of the free-spin rolling moment coefficient from run b29r11 compared to the aerodynamic model using Direct Resolution.

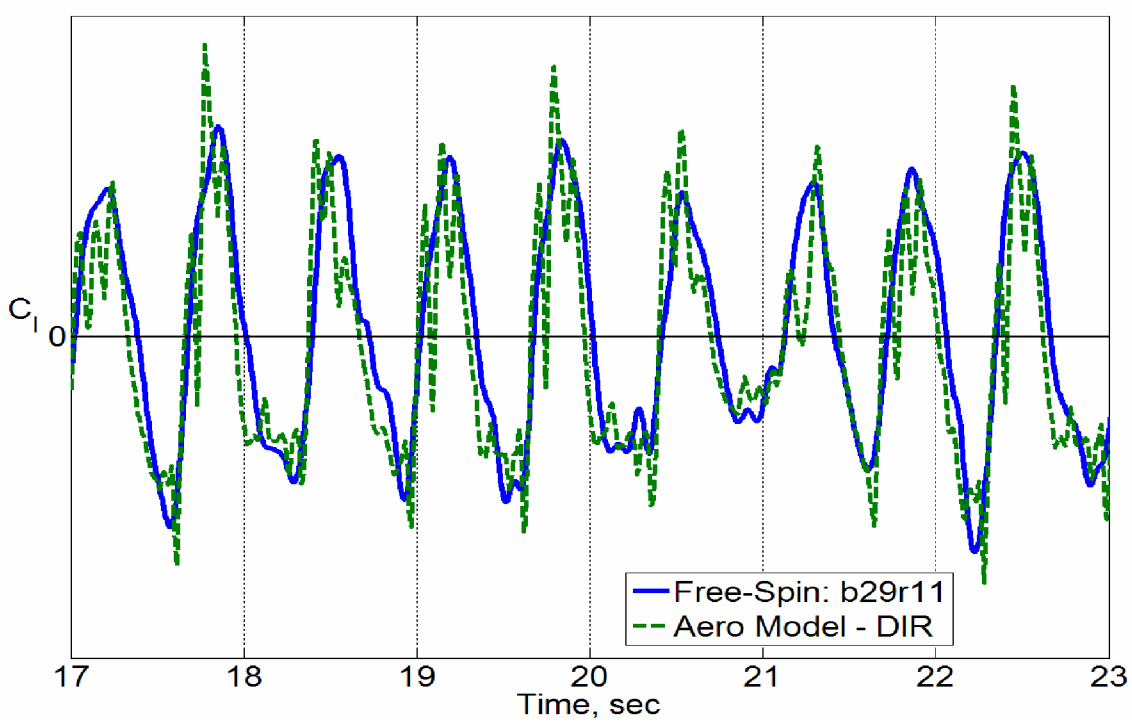

Figure 4.1: Comparison of rolling moment coefficient for free-spin data b29r11 and aerodynamic model using Direct Resolution blending.

The most important feature of Figure 4.1 is the good overall match of the aerodynamic model to the free-spin data. Both the frequency of oscillation and the approximate peak amplitudes are captured by the aerodynamic model. All of the blending methods tested achieved a similarly good match, evidenced by Figure 4.2 through Figure 4.4. Aerodynamic model results using Direct Resolution are also depicted on each figure as a baseline for comparison.

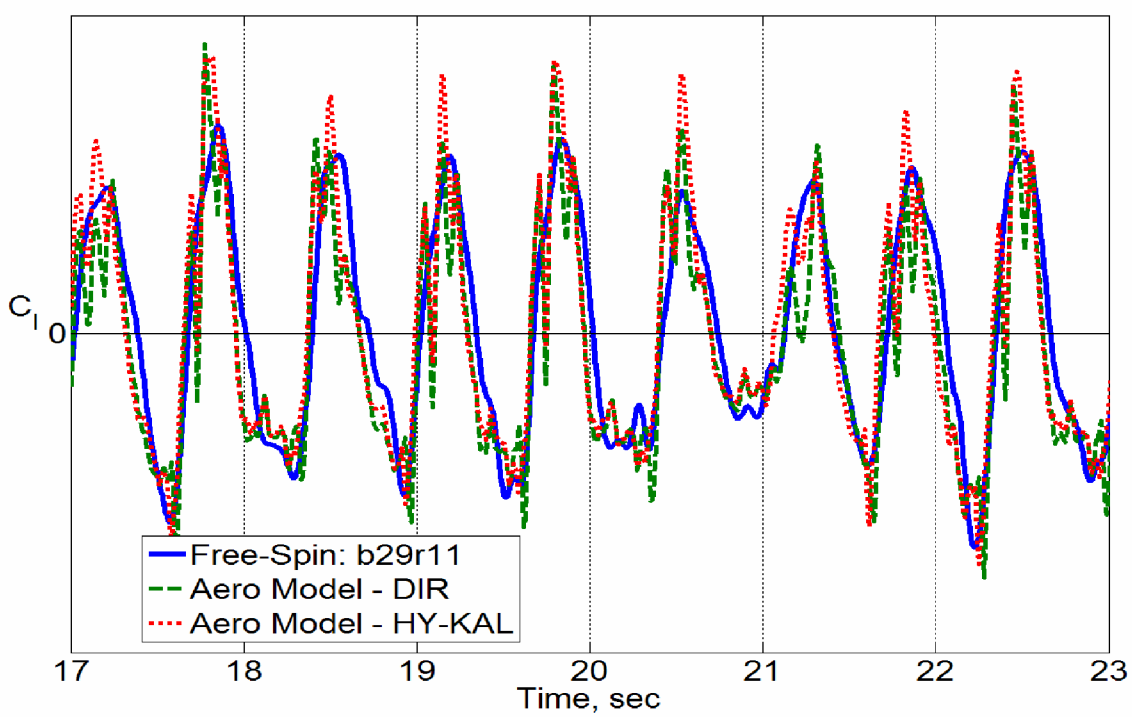

Figure 4.2: Comparison of rolling moment coefficient for free-spin data b29r11 and aerodynamic model using Direct Resolution and Hybrid Kalviste blending.

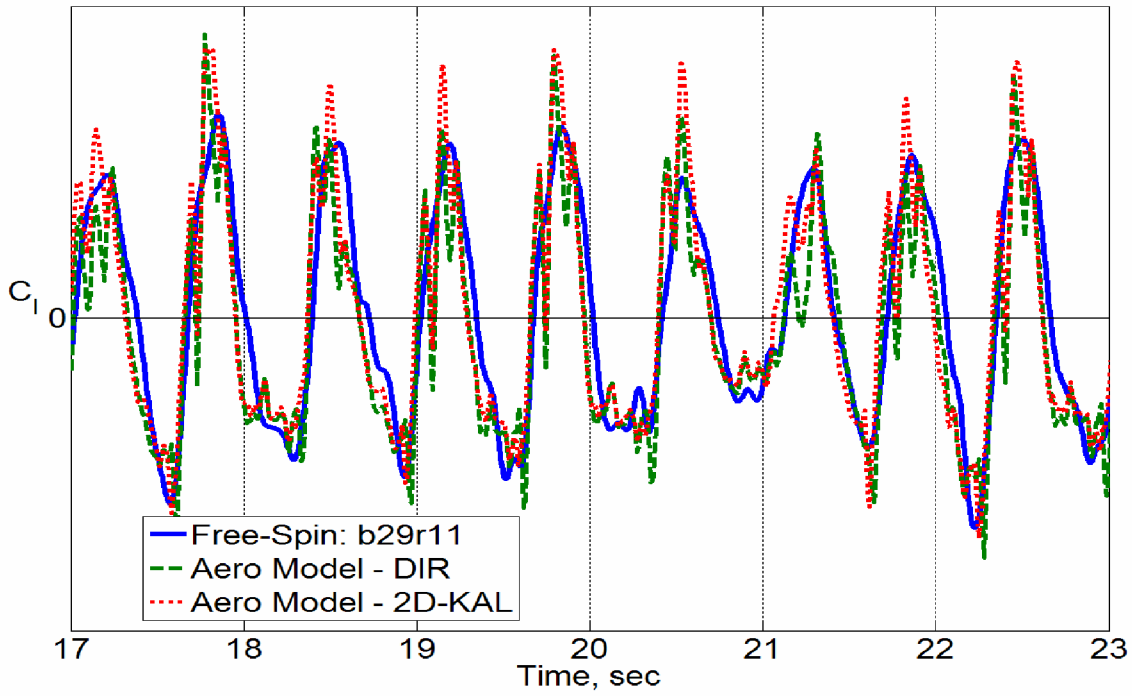

Figure 4.3: Comparison of rolling moment coefficient for free-spin data b29r11 and aerodynamic model using Direct Resolution and 2D Kalviste blending.

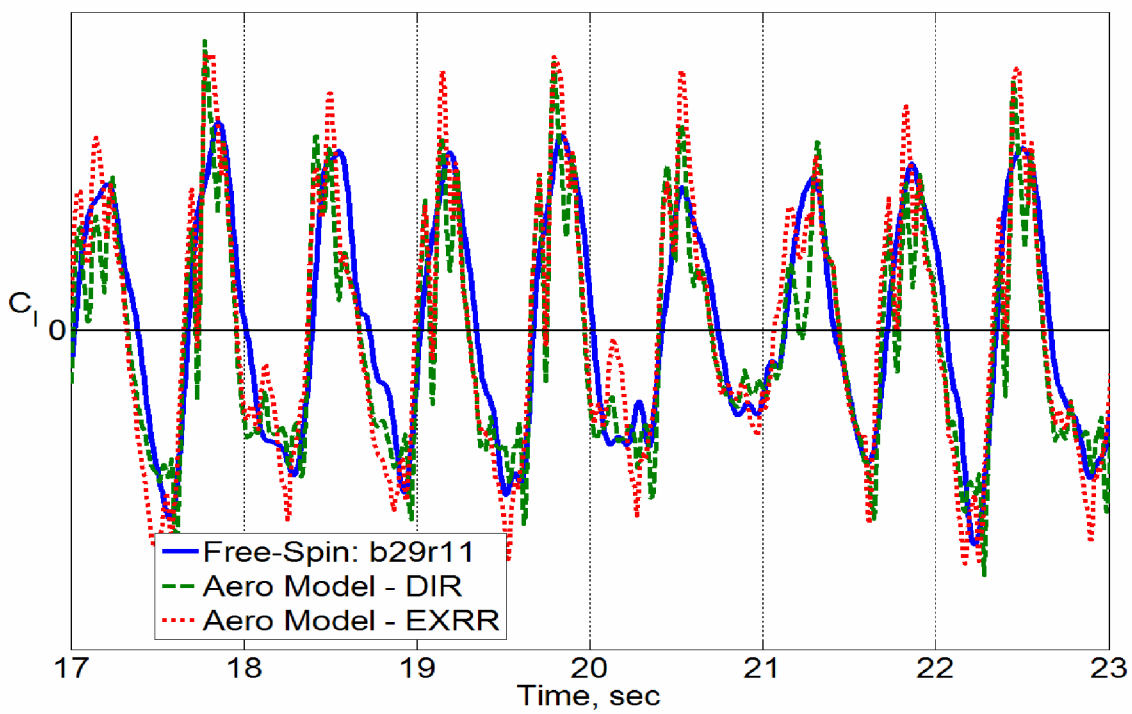

Figure 4.4: Comparison of rolling moment coefficient for free-spin data b29r11 and aerodynamic model using Direct Resolution and Excess Roll Rate blending.

The aerodynamic model prediction using only forced oscillation data or only rotary balance data is shown in Figure 4.5, along with results using Direction Resolution for comparison.

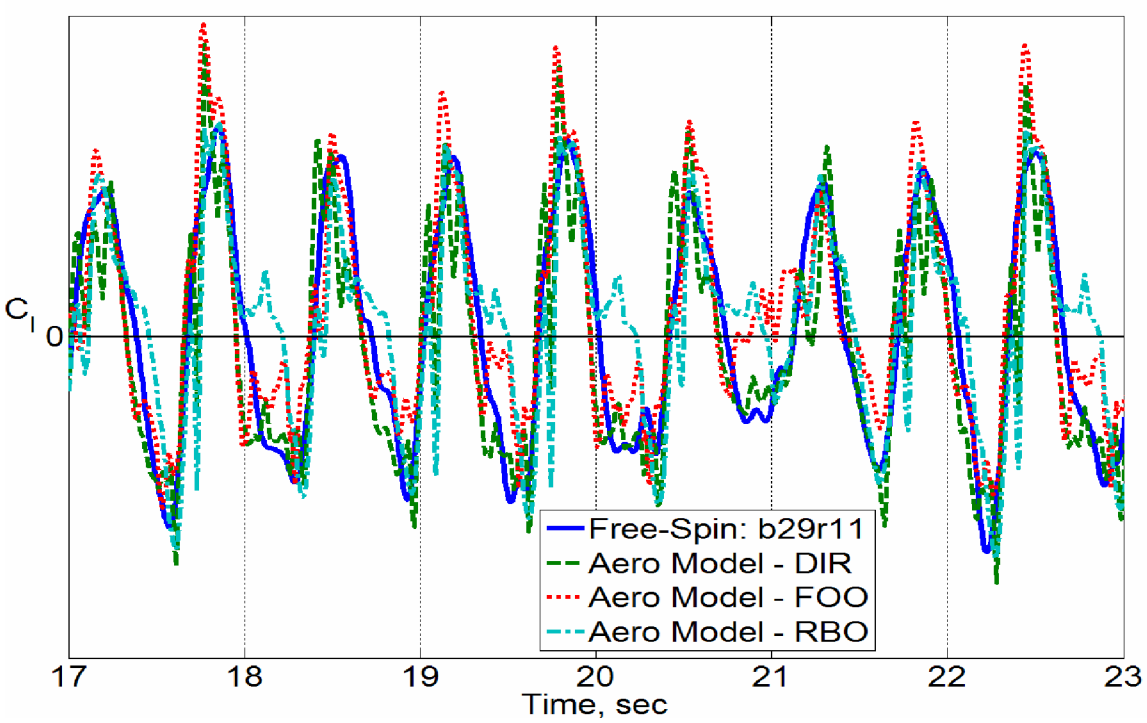

Figure 4.5: Comparison of rolling moment coefficient for free-spin data b29r11 and aerodynamic model using Direct Resolution blending and using forced oscillation data only and using rotary balance data only.

It is clear in Figure 4.5 that the aerodynamic model using Direct Resolution blending offers a superior match versus using forced oscillation or rotary balance data alone. However, the angular roll and yaw rates reached during the spin were greater than the roll and yaw forced oscillation database limits, meaning significant extrapolation was required to predict the aerodynamic response. The superior match using the blending techniques was found to be true for the majority of data runs examined, and was in agreement with previous research on fighter aircraft.

The results shown in Figure 4.1 through Figure 4.5 are similar to those obtained in other free-spin data runs. A sampling of these results is given in Figure 4.6 through Figure 4.8:

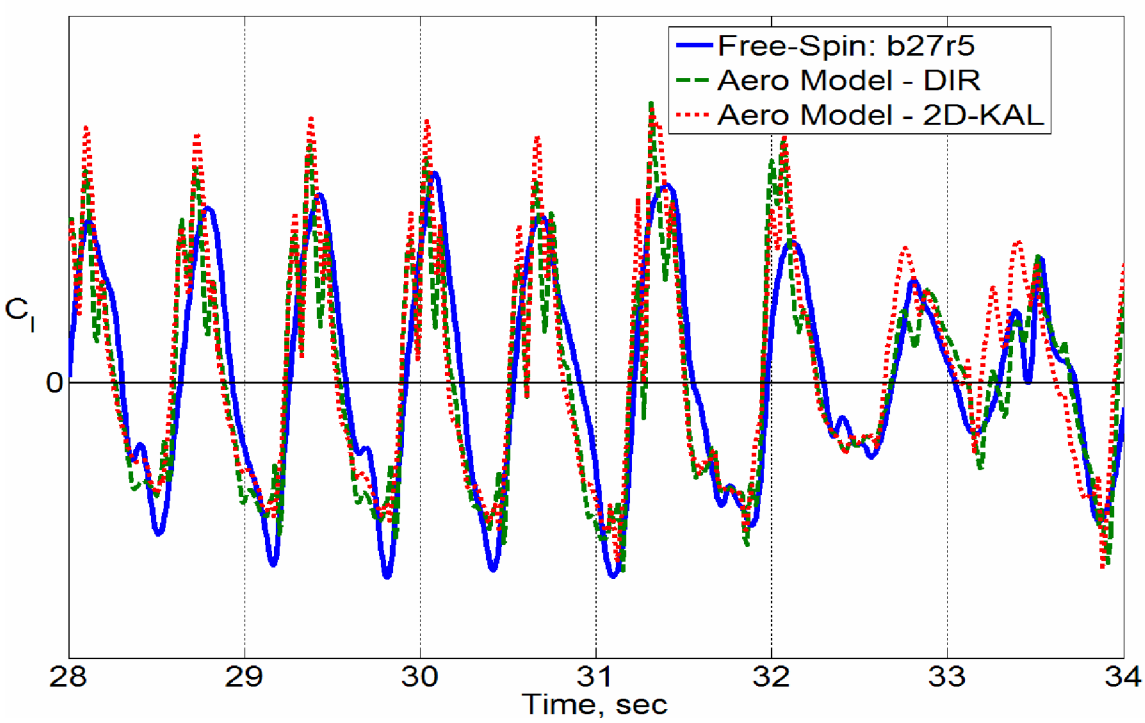

Figure 4.6: Comparison of rolling moment coefficient for free-spin data b27r5 and aerodynamic model using Direct Resolution and 2D Kalviste blending.

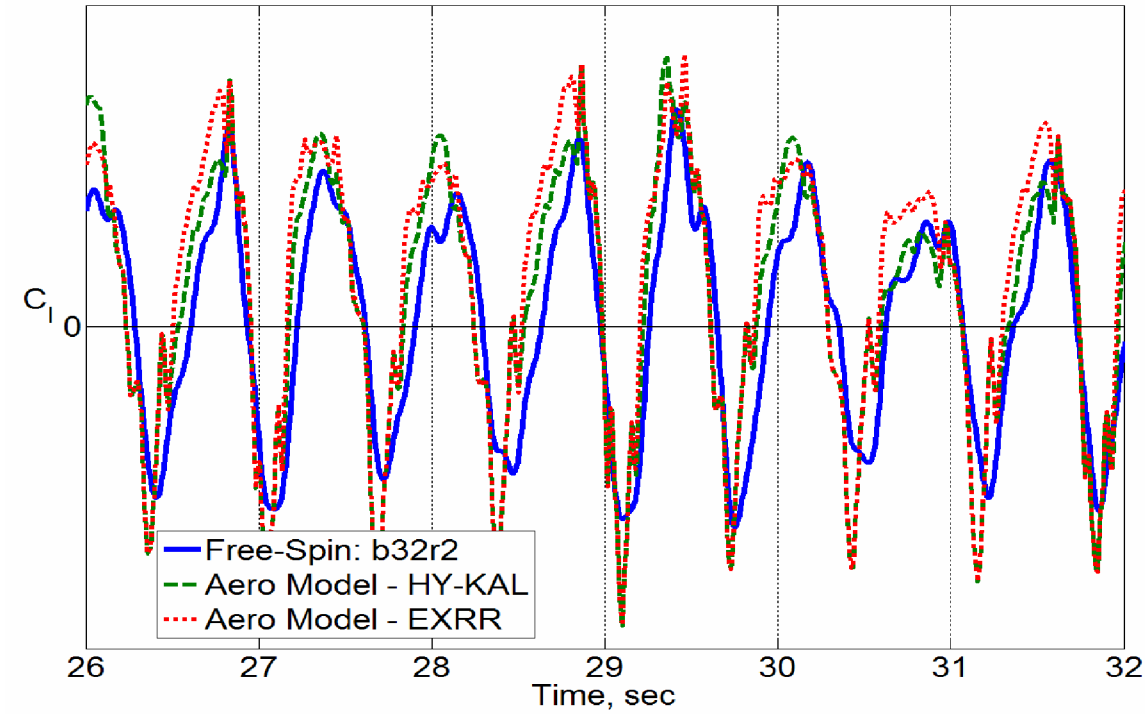

Figure 4.7: Comparison of rolling moment coefficient for free-spin data b32r2 and aerodynamic model using Hybrid Kalviste and Excess Roll Rate blending.

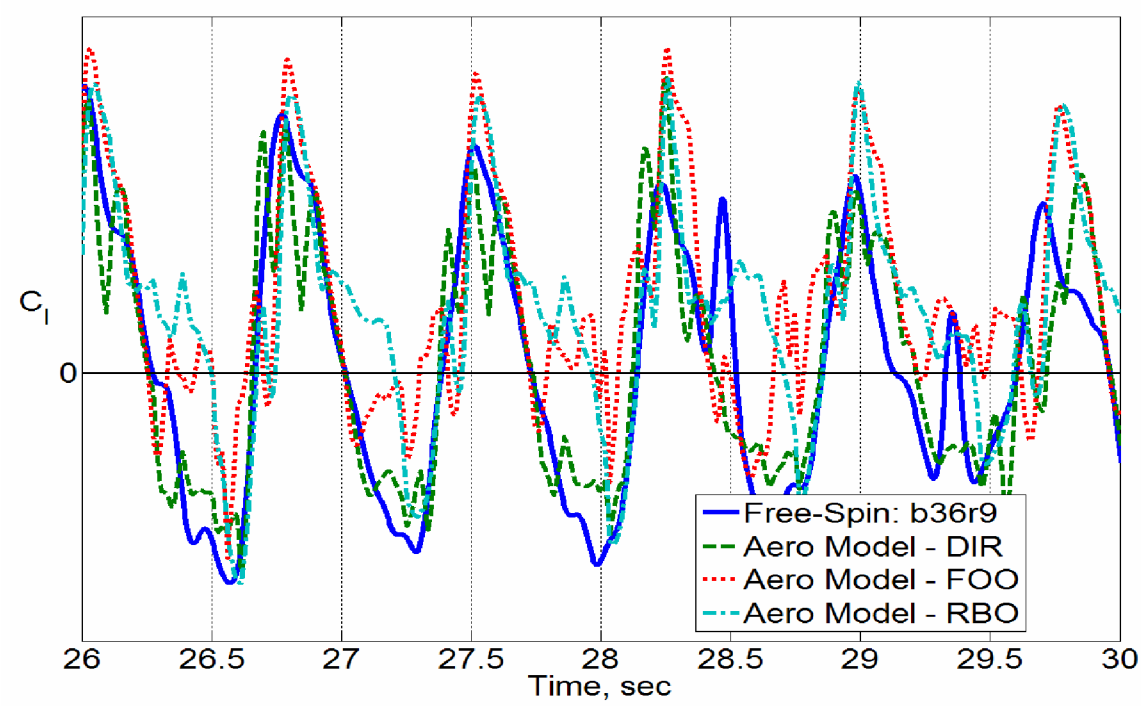

Figure 4.8: Comparison of rolling moment coefficient for free-spin data b36r9 and aerodynamic model using Direct Resolution blending and using forced oscillation data only and using rotary balance data only.

The predictions from the aerodynamic model in Figure 4.1 through Figure 4.8 have a high-frequency component not seen in the free-spin data. This high-frequency component is due in part to the nature of the blending methods and the forced oscillation database, and in part to the reduction method of the rotary balance wind tunnel data. Figure 4.9 shows a subset of Figure 4.1 to highlight these dynamics and their sources.

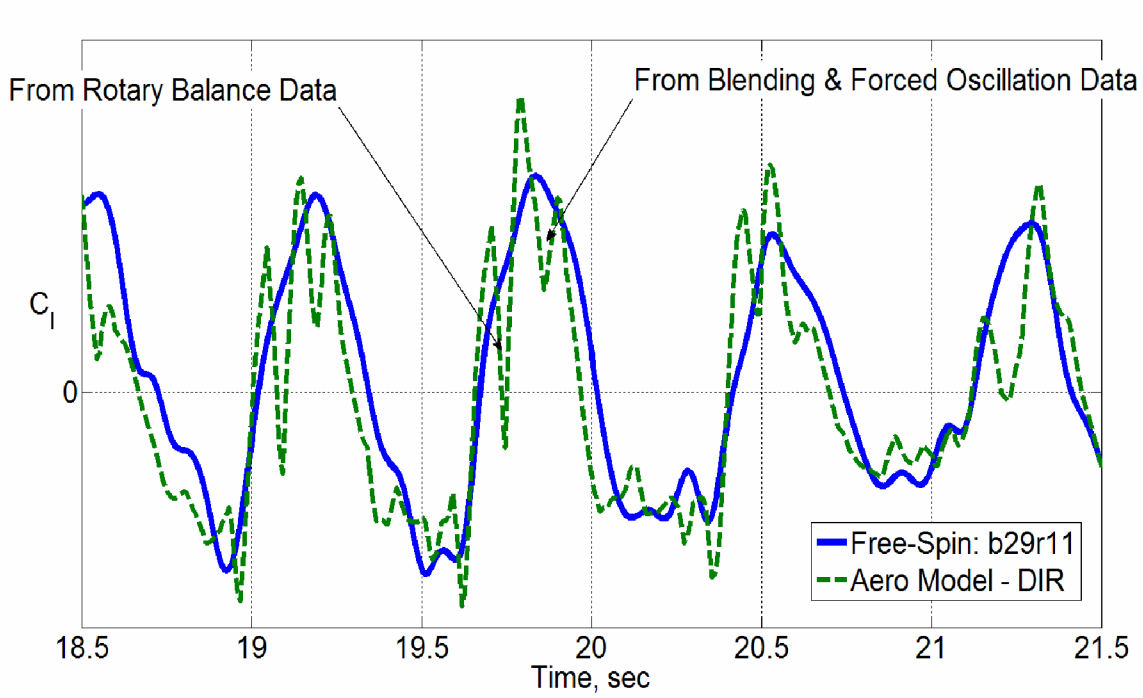

Figure 4.9: Comparison of rolling moment coefficient for free-spin data b29r11 and aerodynamic model using Direct Resolution blending highlighting sources of high-frequency dynamics.

Recall from Section 2.3.2, all of the blending methods compute the oscillatory body-axis rate components by subtracting a portion of the steady-state wind-axis roll component; e.g., for Direct Resolution

$$p_{osc} = p_b - \omega_{ss} \cos\alpha \cos\beta \tag{4.1}$$

Essentially, the oscillatory components are perturbations relative to zero body-axis angular rate. This is not an accurate representation of the aircraft motion in spin, where the body-axis angular rates can be quite large. This mismatch becomes an issue if the aerodynamic effect of angular rate is nonlinear or asymmetric, as was the forced oscillation data used in this research. Figure 4.10 shows the increments to the rolling moment coefficient due to oscillatory roll and yaw rates at $\alpha = 40^{\circ}$.

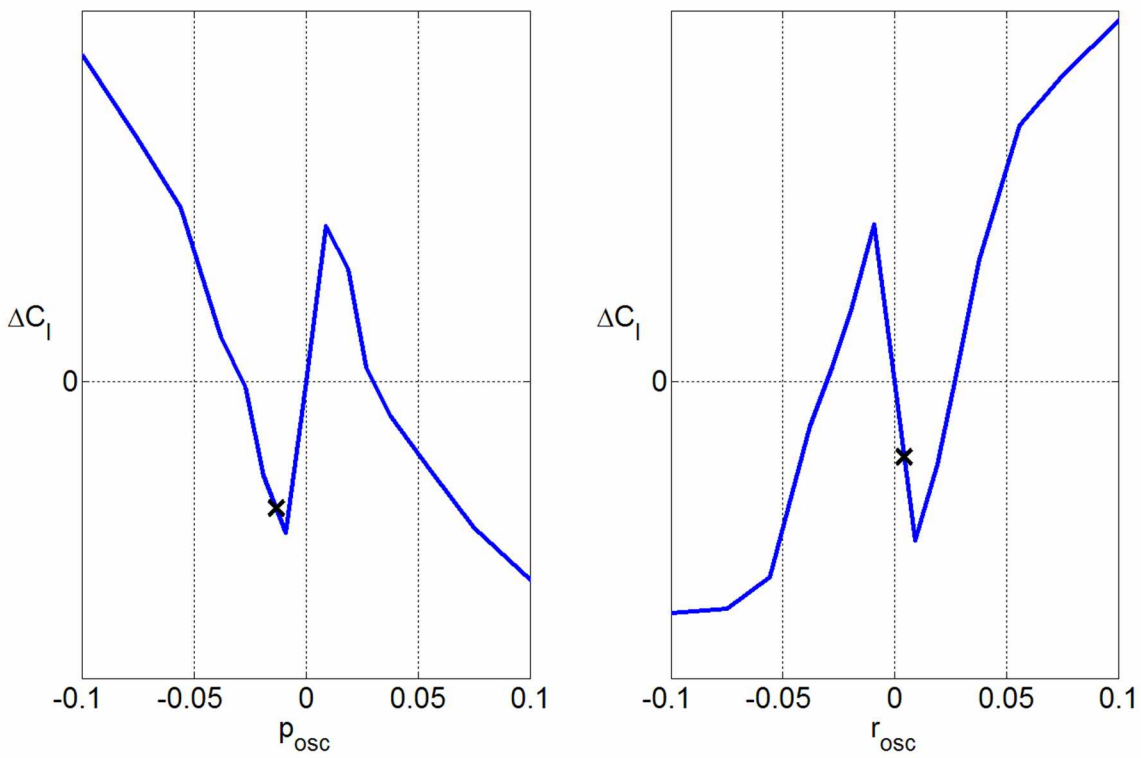

Figure 4.10: Increments to rolling moment coefficient due to oscillatory roll and yaw rates at $\alpha = 40^{\circ}$.

The high-frequency dynamics attributed to the blending method and forced oscillation data in Figure 4.9 are a direct result of the blending method causing the oscillatory components to pass through these nonlinear regions. In addition, the blending methods often simultaneously use data in the nonlinear regions of the roll and yaw oscillatory data, further exacerbating the nonlinearity. Two "X"s in Figure 4.10 represent the simultaneous oscillatory roll and yaw rates approximately at the peak of the oscillation in Figure 4.9.

While it may be possible that the nonlinear behavior of the database is not a realistic representation of the actual aerodynamics, more pertinent is the fact that the blending method is using data at an angular rate not representative of the actual aircraft motion. A more realistic representation of the aircraft motion would be to use the forced

oscillation data near the actual body-axis angular rates of the aircraft. A new lookup method using this philosophy is discussed in Chapter 6.

An additional source of high-frequency dynamics shown in Figure 4.9 is from the rotary balance database. As described in Section 3.2.2.4, the incremental rotary database was created by subtracting the zero-rate coefficient value (i.e., the static value) at a particular angle of attack and sideslip angle from the non-zero rate coefficient values at that same angle of attack and sideslip angle. In equation form, using rolling moment as an example, this process is simply

$$\Delta C_l\left(\alpha_i, \beta_j, \hat{\omega}_{ss}\right) = C_l\left(\alpha_i, \beta_j, \hat{\omega}_{ss}\right) - C_l\left(\alpha_i, \beta_j, \hat{\omega}_{ss} = 0\right) \tag{4.2}$$

Difficulties can arise with this method when there are asymmetries present in the static data, since this method assumes any difference between the static and dynamic values is entirely due to the angular rate. "Aerodynamic asymmetries" is a somewhat general term often used to describe certain nonlinear effects in experimental data. The most common form is non-zero values for side force, rolling moment, and yawing moment when the sideslip angle is zero, i.e.

$$\begin{aligned} C_Y(\alpha, \beta = 0^-) &\neq 0 \\ C_l(\alpha, \beta = 0^-) &\neq 0 \\ C_n(\alpha, \beta = 0^-) &\neq 0 \end{aligned} \tag{4.3}$$

For an aircraft symmetric about the *xz* – plane, these values are normally expected to be zero. This type of aerodynamic asymmetry is a known phenomenon that can be caused by artificial means (e.g., wind tunnel model flaws, inaccurate sting positioning), unsteady aerodynamic flows (e.g., vortices shedding off the aircraft forebody), and/or other unmodeled aerodynamic phenomena.

This presents a unique challenge for reducing the rotary balance data, since when an asymmetry is present in the static data at $\beta = 0$ it is propagated to the rest of the dynamic data via Equation (4.2). This data reduction method assumes any asymmetry present at zero rate is also present at non-zero rate. This is exactly what occurred for the rotary balance data in this research. Figure 4.11 shows the rotary data before and after reduction for $\alpha = 50^{-}$ and $\beta = 0^{-}$ showing how the asymmetry at $\hat{\omega}_{ss} = 0$ was propagated to the rest of the data.

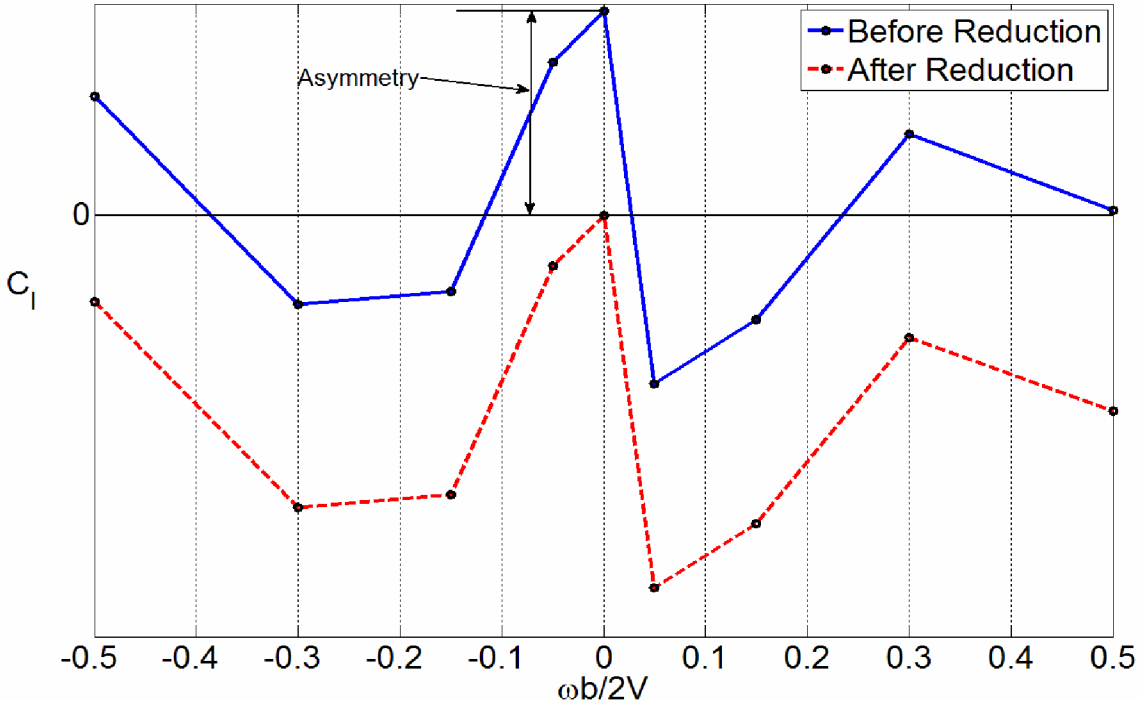

Figure 4.11: Rotary balance data at $\alpha = 50^{-}$ and $\beta = 0^{-}$, before and after data reduction showing propagation of static asymmetry.

This phenomenon occurred at other angles of attack as well. Figure 4.12 shows the static asymmetries in the rolling moment coefficient for the rotary balance data, which were also propagated through the dynamic data during the reduction process.

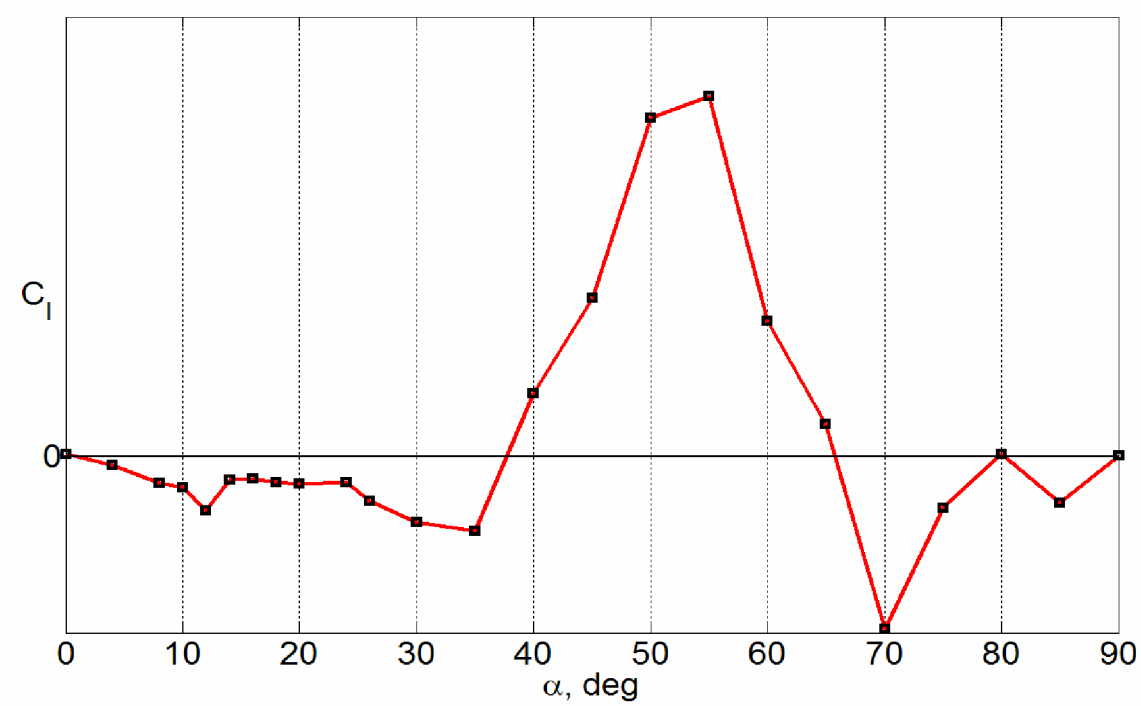

Figure 4.12: Rolling moment coefficient asymmetry from rotary balance data, $\beta = 0^-$, $\hat{\omega}_{ss} = 0$.

The high-frequency dynamic attributed to the rotary balance data in Figure 4.9 occurs just as the aircraft is passing through $\beta = 0^-$, and is a direct result of the asymmetry shown above. Figure 4.13 shows the rolling moment increment plotted versus sideslip angle for $\alpha = 50^-$ and $\hat{\omega}_{ss} = -0.15$, which shows how the asymmetry at $\beta = 0^-$ can exaggerate nonlinear behavior near $\beta = 0^-$.

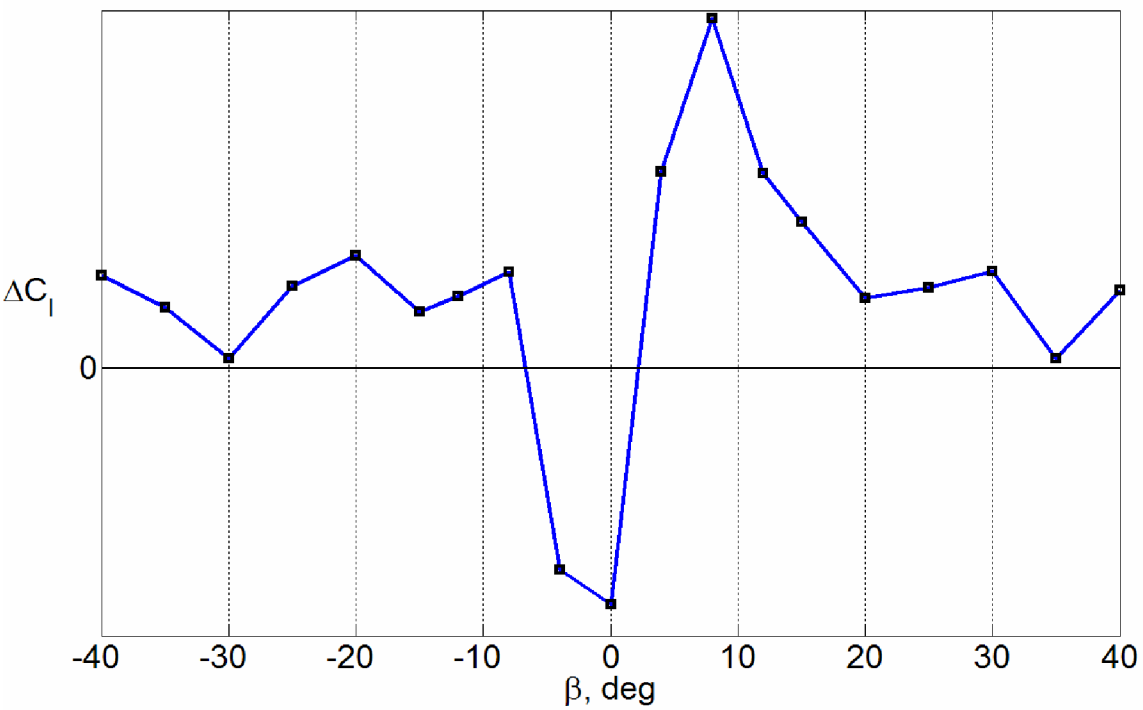

Figure 4.13: Rolling moment coefficient increment from rotary balance data for $\alpha = 50^{\circ}$ and $\hat{\omega}_{ss} = -0.15$.

A better understanding of the true nature and causes of aerodynamic asymmetries is needed to properly address this issue. One possible way of dealing with the effect of asymmetries on data reduction is to make the aerodynamic data symmetric, which is discussed in Chapter 6. However, this does not address the fundamental issue of identifying what causes aerodynamic asymmetries and whether the asymmetries remain when the aircraft is rotating.

Finally, returning to the high-frequency dynamics in the aerodynamic model output, the post-processing of the free-spin data must also be considered. Recall from Section 3.5.3 that the free-spin data is smoothed using an optimal global Fourier algorithm, which removed all portions of the signal above 7 Hz. The high-frequency dynamics seen in the aerodynamic model output are around 10-20 Hz; therefore, even if

these dynamics were present in the free-spin data they would have been removed during the smoothing process. Higher cutoff frequencies for the smoothing process were attempted, but any noise in the signal is amplified by numerical differentiation that is part of the data post-processing. Moving the cutoff frequency to 10 Hz only appeared to add noise to the data. Finally, the vast majority of rigid-body dynamics for full-scale aircraft are below 1 Hz (7 Hz for the free-spin scale). While nonlinear and unsteady aerodynamic effects can occur at higher frequencies, it is likely the high-frequency dynamics seen in the aerodynamic model output are simply an artifact of the blending methods and dynamic wind tunnel data reduction rather than a realistic representation of the spin dynamics.

In summary for this section, the aerodynamic model using any of the blending methods produced a good match to the free-spin rolling moment. Use of forced oscillation or rotary balance data alone yielded poorer results. High-frequency dynamics in the aerodynamic model output were a result of the blending methods and nonlinearities in the forced oscillation database as well as the data reduction method propagating asymmetries through the rotary balance database. Recommendations on these issues are discussed in Chapter 6.

4.2.2 Pitching Moment Coefficient

The following section shows results for the pitching moment coefficient. Overall, the match between the free-spin data and the aerodynamic model was not as good as the rolling moment coefficient. The first set of figures is intended to compare the modeling methods to free-spin data and to each other. Free-spin data from run b29r11 is used.

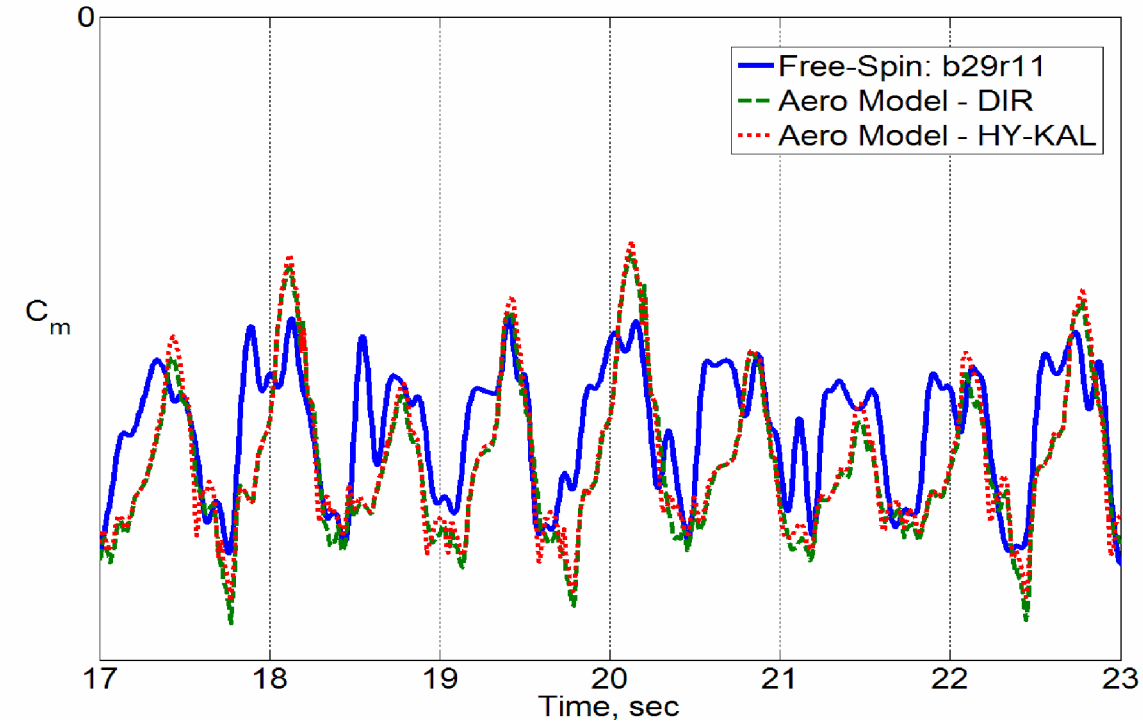

Figure 4.14: Comparison of pitching moment coefficient for free-spin data b29r11 and aerodynamic model using Direct Resolution and Hybrid Kalviste blending.

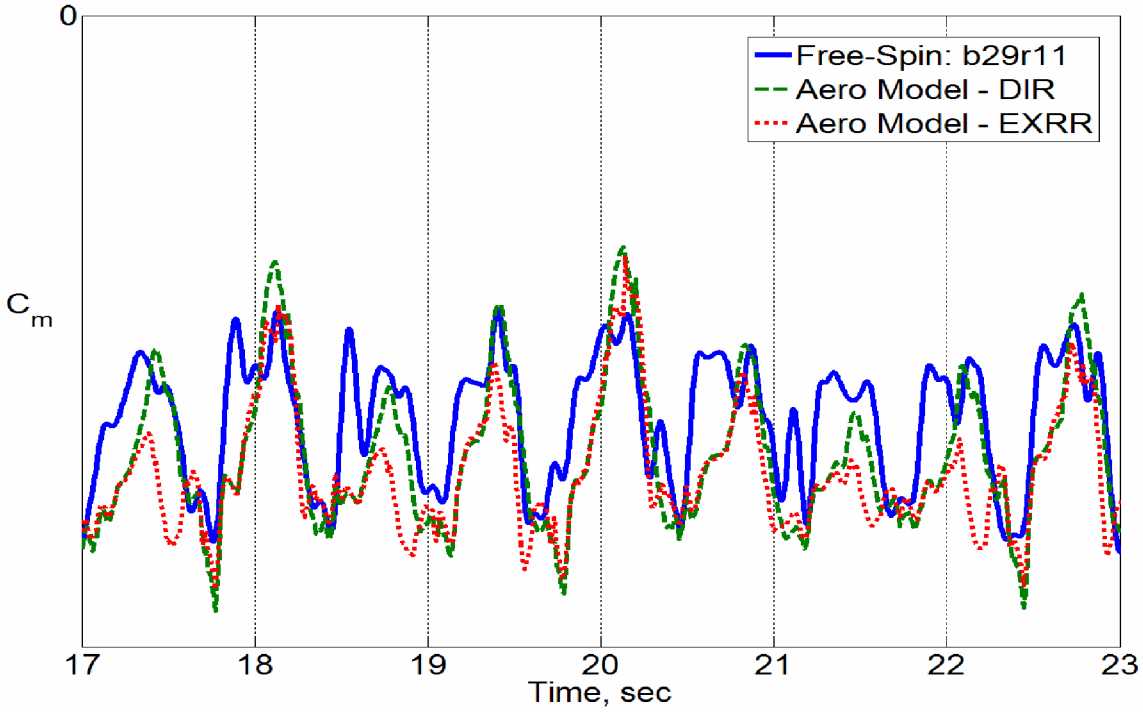

Figure 4.15: Comparison of pitching moment coefficient for free-spin data b29r11 and aerodynamic model using Direct Resolution and Excess Roll Rate blending.

Figure 4.14 and Figure 4.15 show that the Direct Resolution, Hybrid Kalviste, and Excess Roll Rate methods all have reasonable results. The Excess Roll Rate method often diverged from the group. The worst match of the blending methods was the 2D Kalviste method, shown in Figure 4.16:

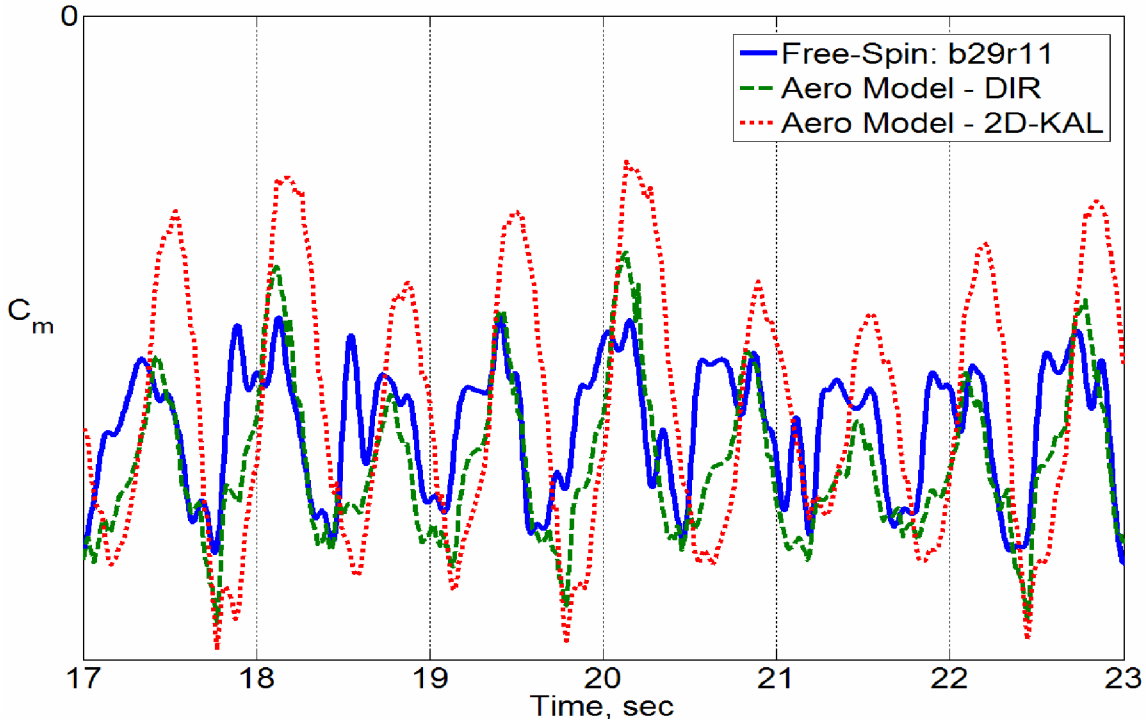

Figure 4.16: Comparison of pitching moment coefficient for free-spin data b29r11 and aerodynamic model using Direct Resolution and 2D Kalviste blending.

The poor match of the 2D Kalviste method is largely due to the fact that the pitch axis effects are being double counted with this method. Recall from Section 2.3.2.2, the oscillatory pitch rate is simply the body-axis pitch rate, i.e.:

$$q_{osc} = q_b \tag{4.4}$$

The pitch axis component of the steady state component is not removed from the body-axis pitch rate because this method ignores sideslip angle. However, there is a pitching

moment increment from the steady-state component (rotary balance data) and from the full body-axis pitch rate (forced oscillation data), i.e.:

$$\Delta C_{m,dynamic} = \Delta C_{m,\hat{q}_{osc}}\left(\alpha, \hat{q}_{osc}\right) + \Delta C_{m,\hat{\omega}_{ss}}\left(\alpha, \hat{\omega}_{ss}\right) \tag{4.5}$$

The oscillatory rate used with the forced oscillation term in Equation (4.5) has not been adjusted to reflect the inclusion of the rotary balance term, and as a result, the dynamic pitching moment increment is exaggerated. This result indicates the 2D Kalviste method is unsuitable for modeling motions that have substantial pitch rate.

Similar to the results shown in the last section for the rolling moment coefficient, using a blending method gave better results than using forced oscillation or rotary balance data alone, as evidenced by Figure 4.17:

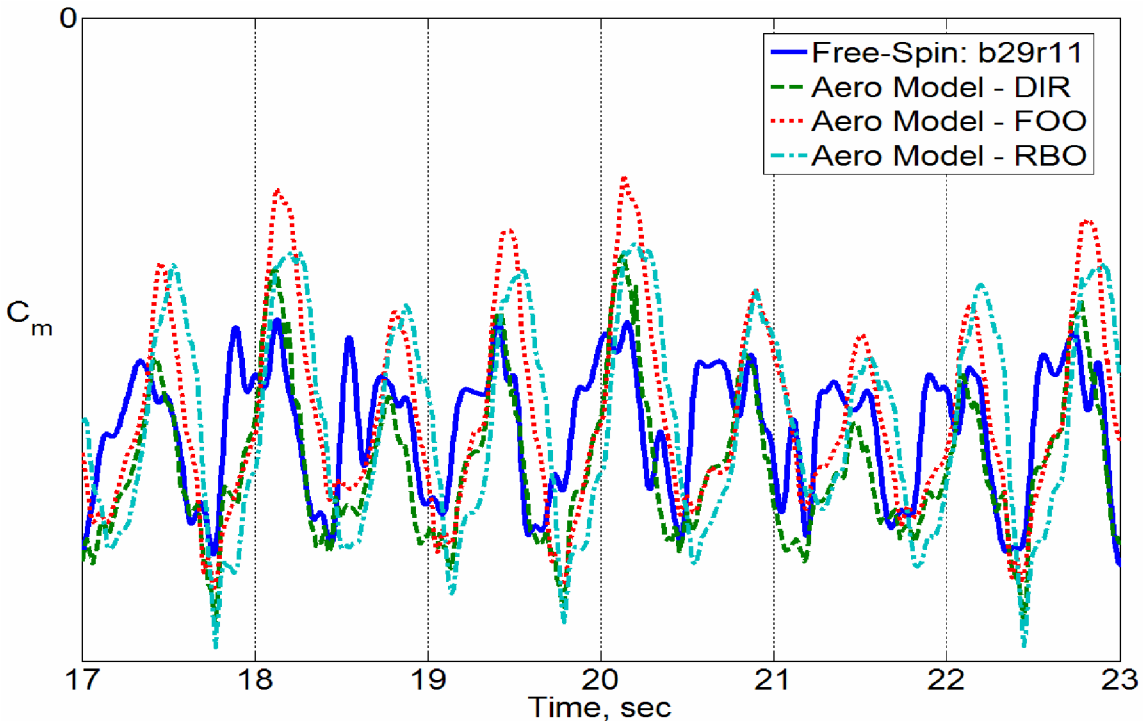

Figure 4.17: Comparison of pitching moment coefficient for free-spin data 29r11 and aerodynamic model using Direct Resolution blending and using forced oscillation data only and using rotary balance data only.

The results shown in Figure 4.14 through Figure 4.17 are similar to those obtained in other free-spin data runs. A sampling of these results is given in the following set of figures:

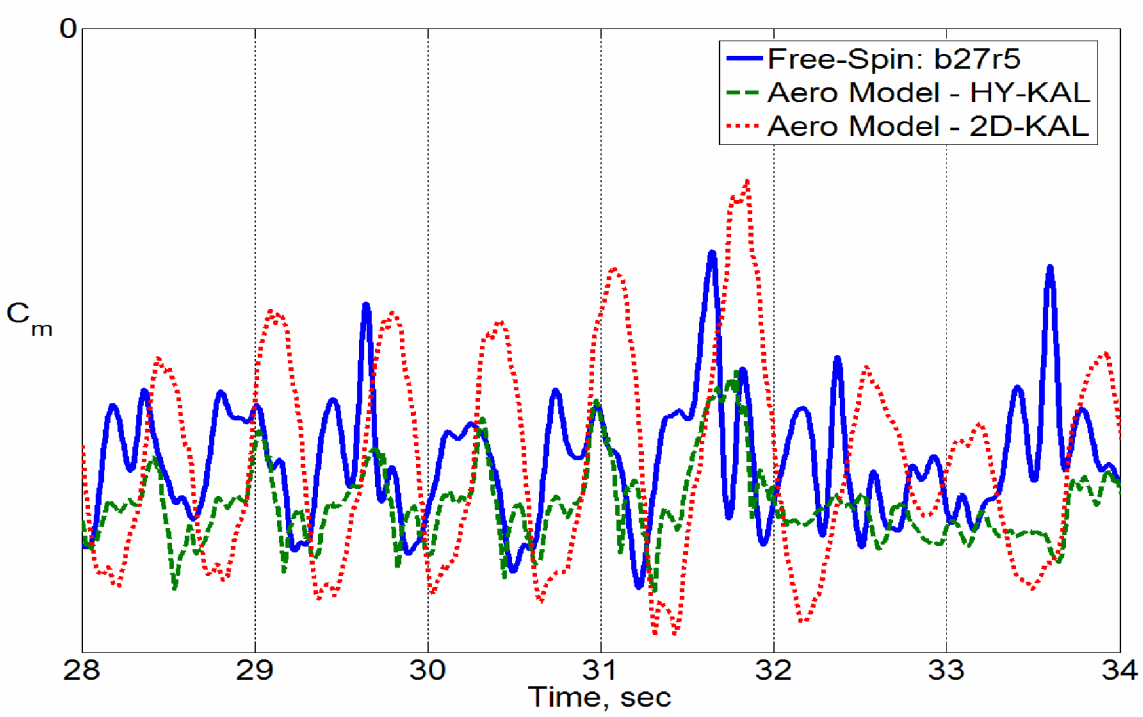

Figure 4.18: Comparison of pitching moment coefficient for free-spin data b27r5 and aerodynamic model using Hybrid Kalviste and 2D Kalviste blending.

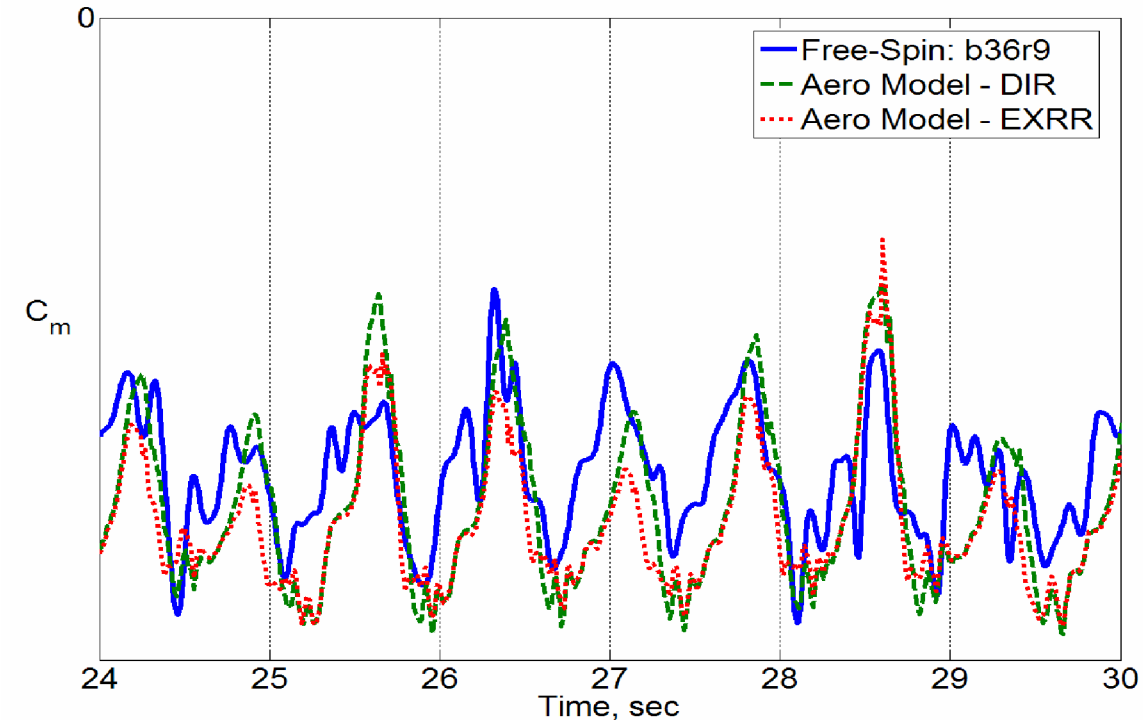

Figure 4.19: Comparison of pitching moment coefficient for free-spin data b36r9 and aerodynamic model using Direct Resolution and Excess Roll Rate blending.

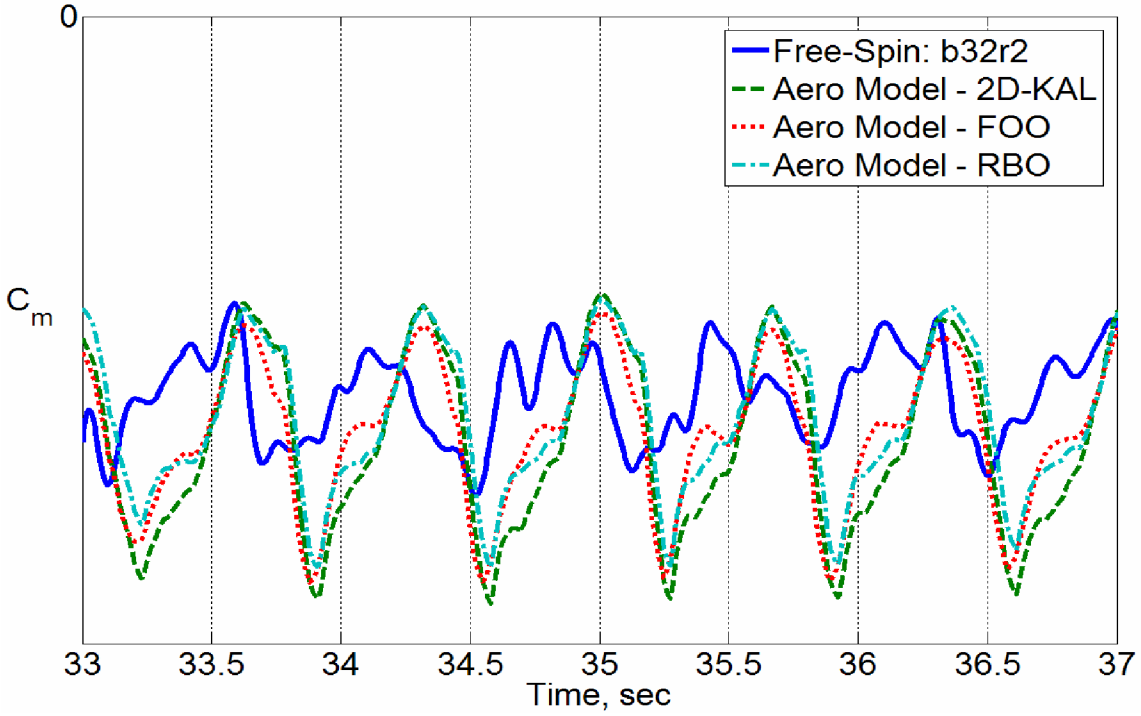

Figure 4.20: Comparison of pitching moment coefficient for free-spin data b32r2 and aerodynamic model using Hybrid Kalviste blending and using forced oscillation data only and using rotary balance data only.

The mismatch between the aerodynamic model and the free-spin data shown in Figure 4.14 through Figure 4.20 may stem from several sources. First, it must be recognized that the blending methods were mainly intended to model rolling and yawing motions. For instance, the 2D and Hybrid Kalviste methods do not consider the pitch axis when selecting which data set to use (ref Section 2.3.2.2) (Note: Kalviste's original formulation did include the pitch axis in the selection criteria, but numerous issues were encountered with this approach and it was abandoned in favor of the Hybrid and 2D formulations).

In addition, the oscillatory pitch rates computed by the Direct Resolution, Hybrid Kalviste, and Excess Roll Rate methods can exceed the limits of the pitch forced oscillation database making extrapolation necessary. This is due to the large angular rates and significant sideslip angles reached during the oscillatory spin motion. For example, recall from Section 2.3.2.1, the oscillatory pitch rate for Direct Resolution is computed by

$$q_{osc} = q_b - \omega_{ss} \sin\beta \tag{4.6}$$

During the oscillatory spin, the steady state angular rate (ω_{ss}) and the sideslip angle can be large relative to the body-axis pitch rate, which results in the second term of Equation (4.6) dominating the oscillatory pitch rate. While extrapolation outside of databases can be misleading, the pitch rate effects tend to be relatively linear with respect to angular rate, indicating adverse effects from extrapolation should be minimal.

Analysis of the free-spin data led to questions about the possible influence of the tether attached to the model. While care was taken to select data only where the tether appeared to be slack, the tether could still have exerted some force on the model. Since

the attachment point of the tether was approximately 5 inches above the center of gravity, any force exerted by the tether would produce a moment as well. Unfortunately, separating any possible effect of the tether from other sources of error (e.g., modeling error, unmodeled effects, noise, etc) is difficult. The residual between the free-spin pitching moment from run b29r11 and the aerodynamic model using Direct Resolution blending is shown in Figure 4.21.

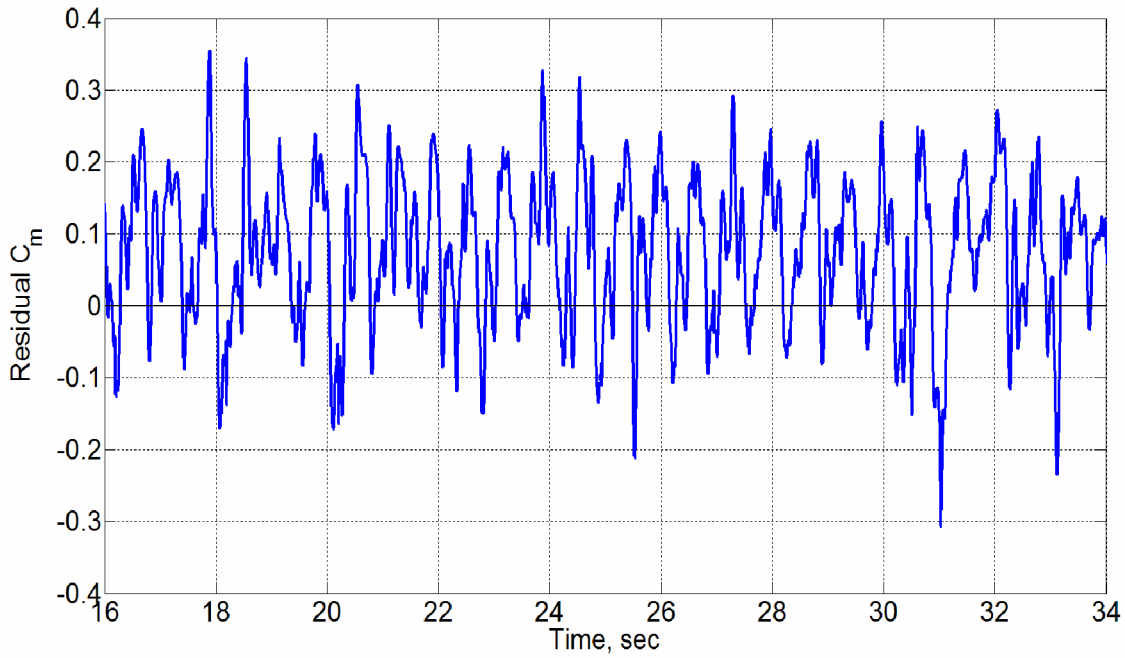

Figure 4.21: Residual pitching moment coefficient for free-spin data 29r11 and aerodynamic model using Direct Resolution

While the residual shown in Figure 4.21 is certainly not constant, it does have a small bias. Analysis of this data showed that the ~0.076 bias in the pitching moment residual could have been caused by a ~0.23 pound rearward force applied at the tether attachment point. Such an applied force would have resulted in a bias in the residual of C_X as well. However, the bias in the residual of C_X would have required a ~0.62 pound rearward

force. The applied forces necessary to account for biases in pitching moment and C_X residuals of several free-spin data runs were calculated and the results are summarized in Figure 4.22.

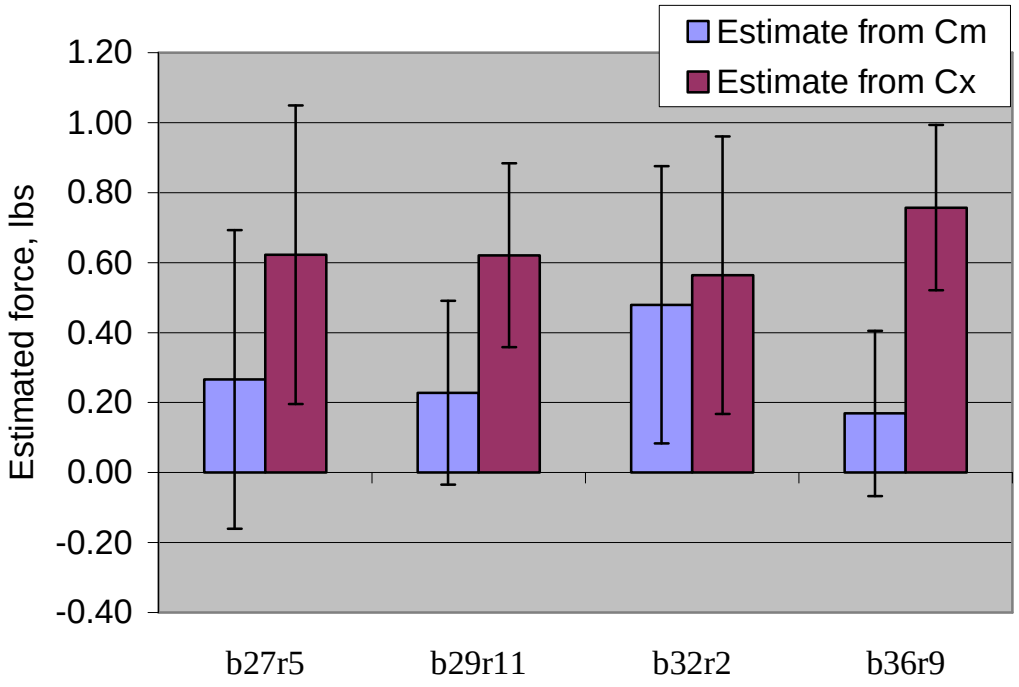

Figure 4.22: Estimated force required to account for biases in C_m and C_X residuals.

As can be seen in Figure 4.22, the required force to account for bias in C_X is generally much larger than the force required to account for the bias in the pitching moment, but there is a large standard deviation on these estimates indicated by the error bars in Figure 4.22. This indicates that the tether exerting a rearward force on the model during the free-spin test could explain the biases in the residual pitching moment and residual C_X, but the evidence is not conclusive. Recommendations regarding this issue will be discussed in Chapter 6.

In summary for this section, the aerodynamic model using the Direct Resolution and Hybrid Kalviste blending methods produced the best match to the free-spin pitching moment. Using the 2D Kalviste method resulted in a very poor match. The tether was identified as a possible source of error in the modeling results.

4.2.3 Yawing Moment Coefficient

The following section shows results for the yawing moment coefficient. The overall match was good, but with some similar issues seen in the rolling moment coefficient. The first set of figures is intended to compare the modeling methods to free-spin data and to each other. Free-spin data from run b29r11 is used.

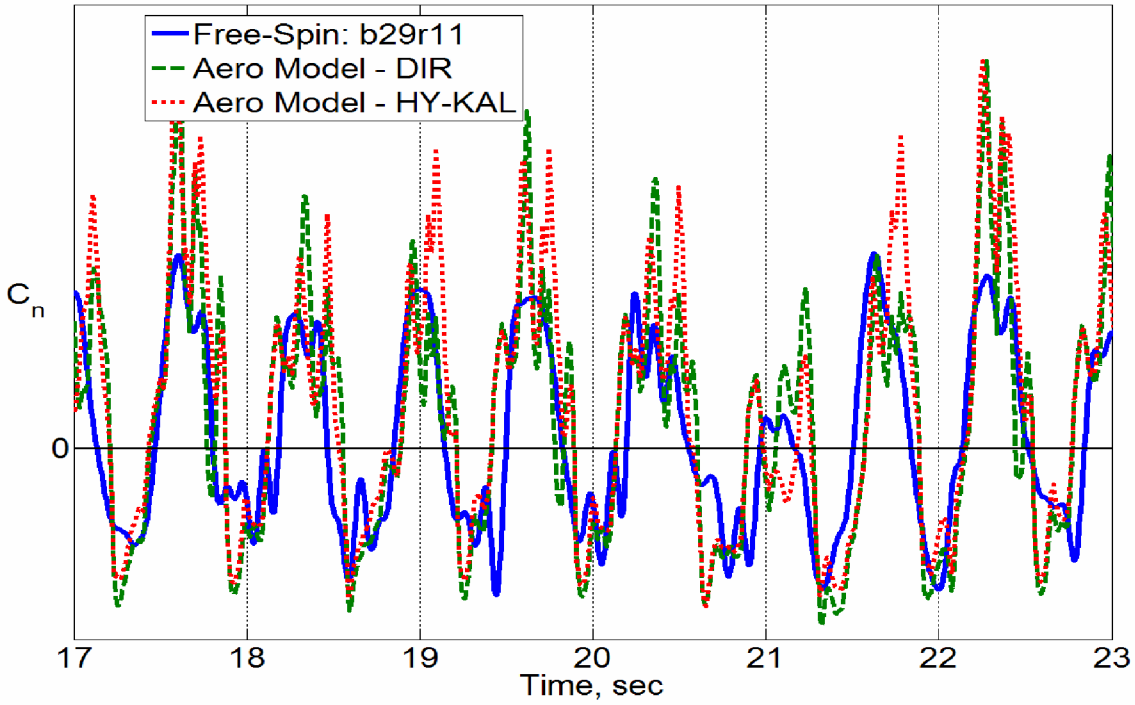

Figure 4.23: Comparison of yawing moment coefficient for free-spin data b29r11 and aerodynamic model using Direct Resolution and Hybrid Kalviste blending.

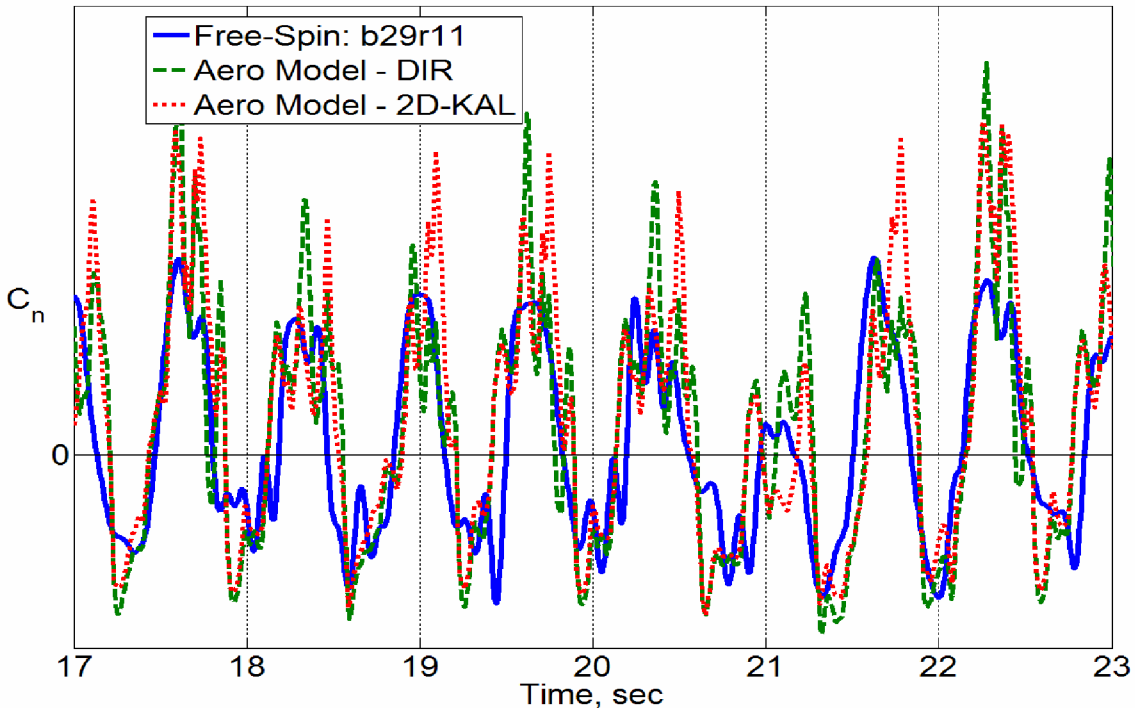

Figure 4.24: Comparison of yawing moment coefficient for free-spin data b29r11 and aerodynamic model using Direct Resolution and 2D Kalviste blending.

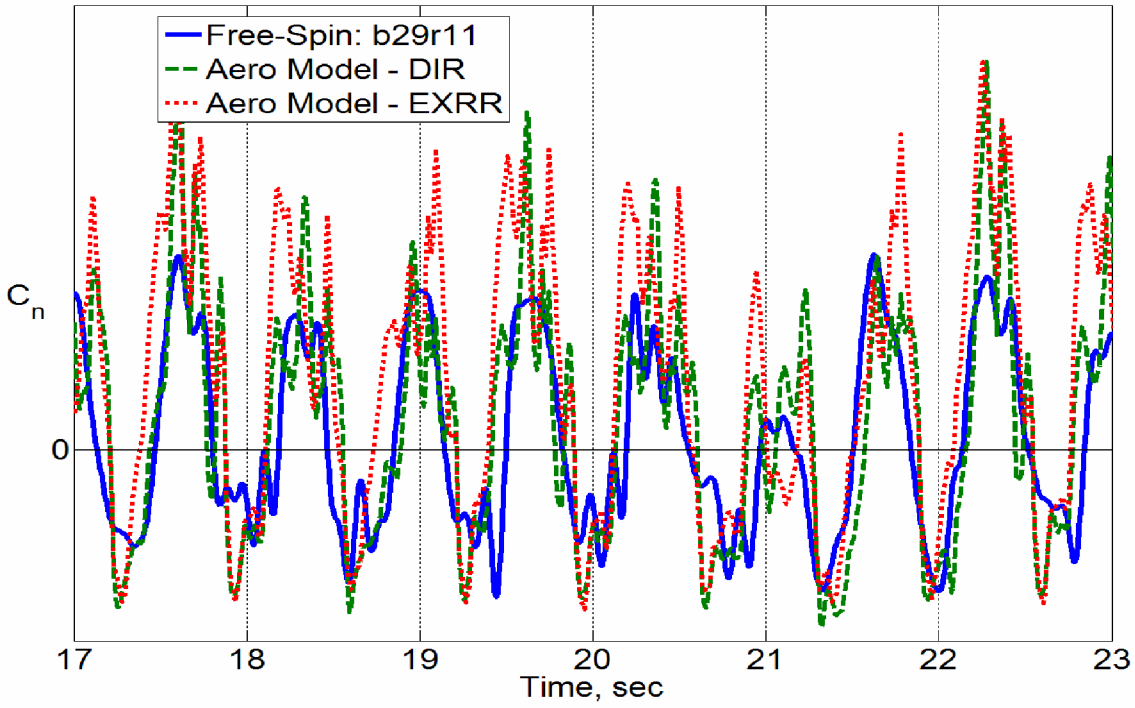

Figure 4.25: Comparison of yawing moment coefficient for free-spin data b29r11 and aerodynamic model using Direct Resolution and Excess Roll Rate blending.

As evidenced by Figure 4.23 through Figure 4.25, all of the blending methods gave similar satisfactory results, but with Direct Resolution and Hybrid Kalviste giving the best. Similar to preceding sections, using a blending method yielded better results than using forced oscillation or rotary balance data alone, as shown in Figure 4.26. However, once again, the angular roll and yaw rates reached during the spin were greater than the roll and yaw forced oscillation database limits, meaning extrapolation was required to predict the aerodynamic response.

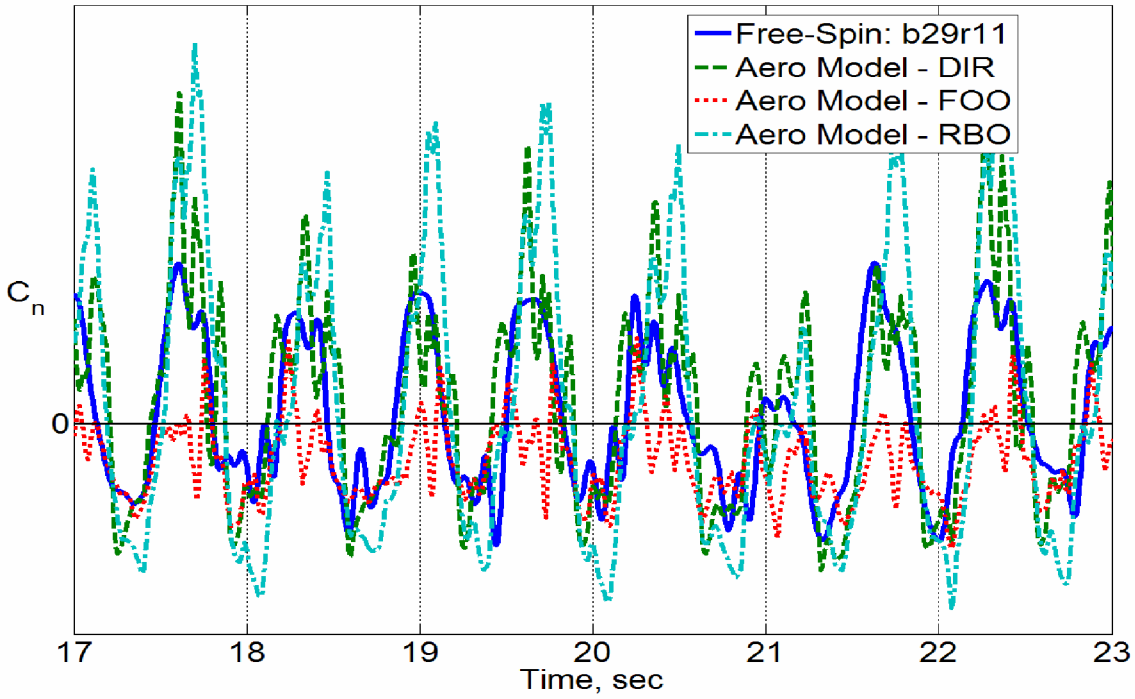

Figure 4.26: Comparison of yawing moment coefficient for free-spin data b29r11 and aerodynamic model using Direct Resolution blending and using forced oscillation data only and using rotary balance data only.

The results shown in Figure 4.23 through Figure 4.26 are similar to those obtained in other free-spin data runs. A sampling of these results is given in the following set of figures:

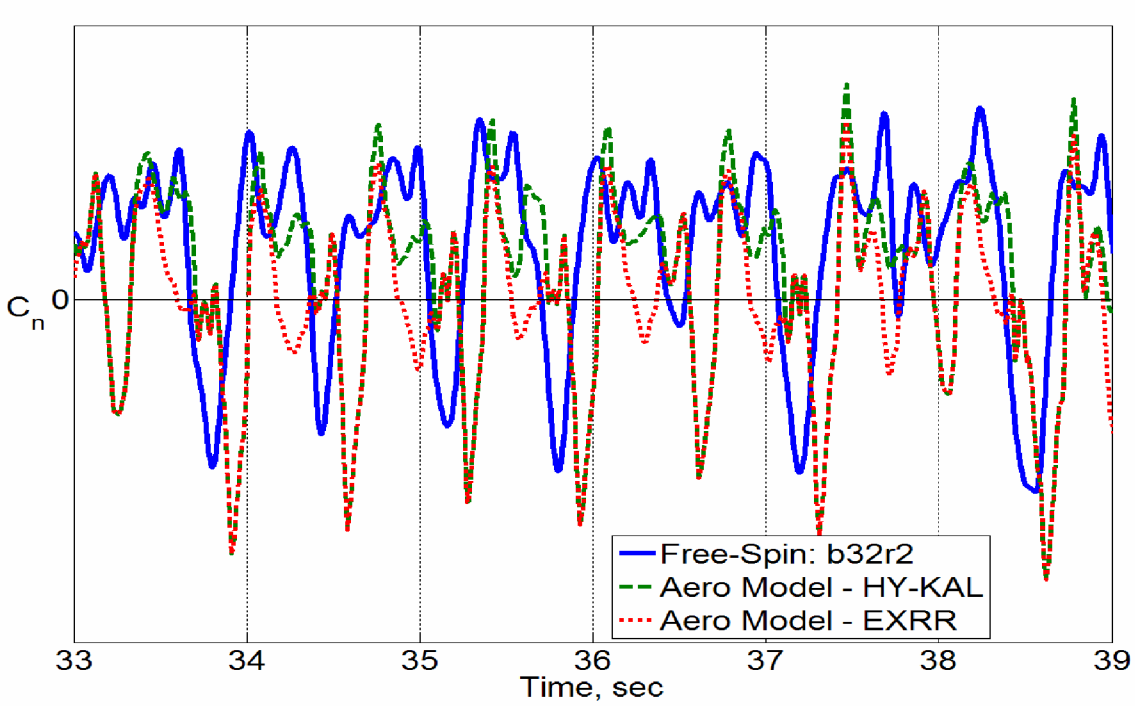

Figure 4.27: Comparison of yawing moment coefficient for free-spin data b32r2 and aerodynamic model using Hybrid Kalviste and Excess Roll Rate blending.

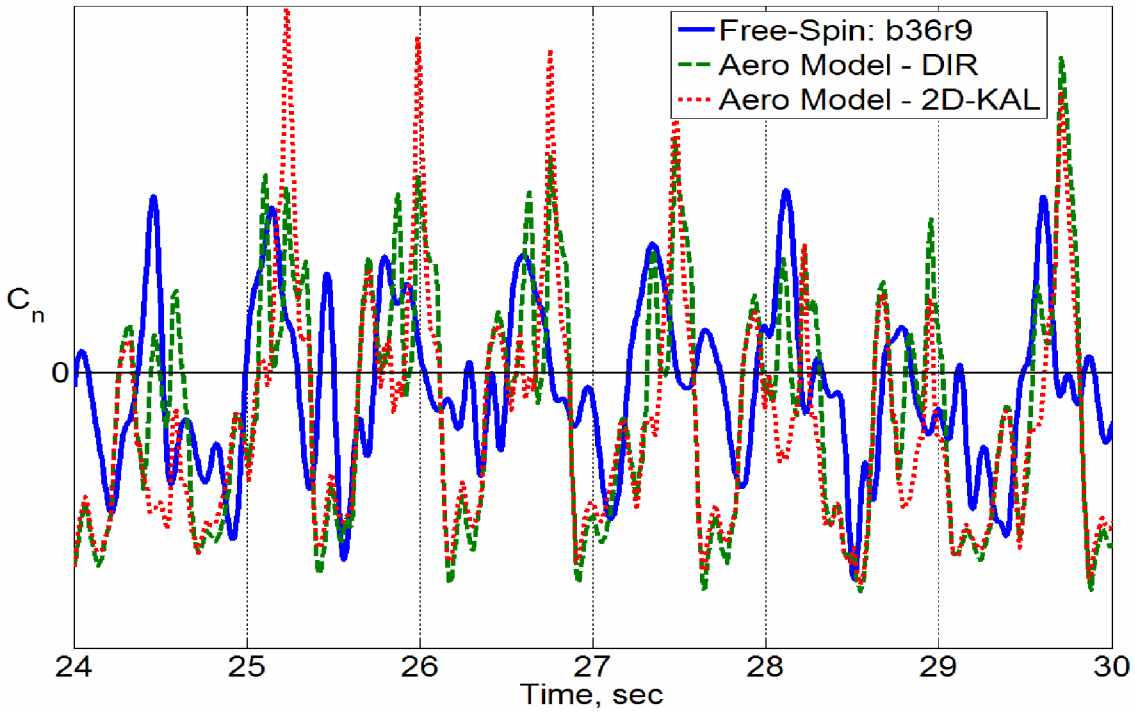

Figure 4.28: Comparison of yawing moment coefficient for free-spin data b36r9 and aerodynamic model using Direct Resolution and 2D Kalviste blending.

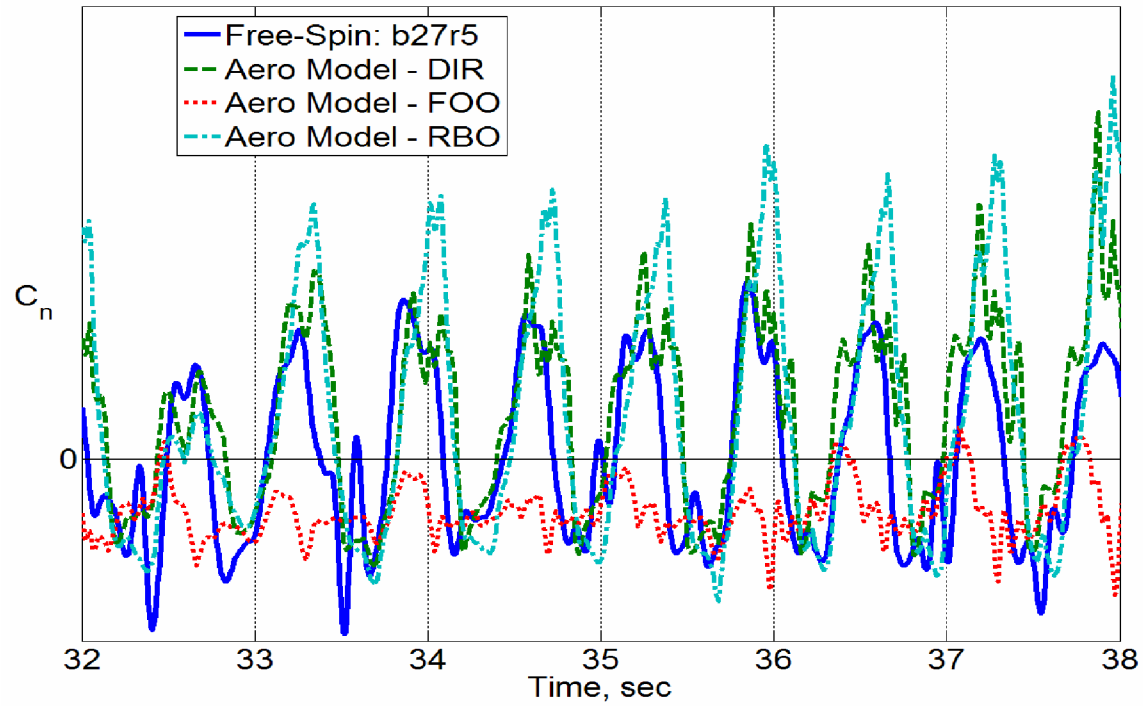

Figure 4.29: Comparison of yawing moment coefficient for free-spin data b27r5 and aerodynamic model using Direct Resolution blending and using forced oscillation data only and using rotary balance data only.

Figure 4.23 through Figure 4.29 show a high-frequency component in the aerodynamic model output not seen in the free-spin data, very similar to what was observed with the rolling moment coefficient. These high-frequency dynamics come from the same sources as identified in Section 4.2.1. Again, this high-frequency component is due in part to the nature of the blending methods and the forced oscillation database, and in part to aerodynamic asymmetries propagated through the reduction of the rotary balance wind tunnel data.

As described in Section 4.2.1, the fundamental issue is that the blending methods look up the oscillatory data at low angular rates not representative of the actual angular rates of the aircraft. This becomes a problem when the forced oscillation data is nonlinear and/or asymmetric with respect to angular rate, as is the case for the roll and

yaw forced oscillation data. Figure 4.30 shows the increments to yawing moment coefficient due to oscillatory roll and yaw rates at $\alpha = 40^{-}$.

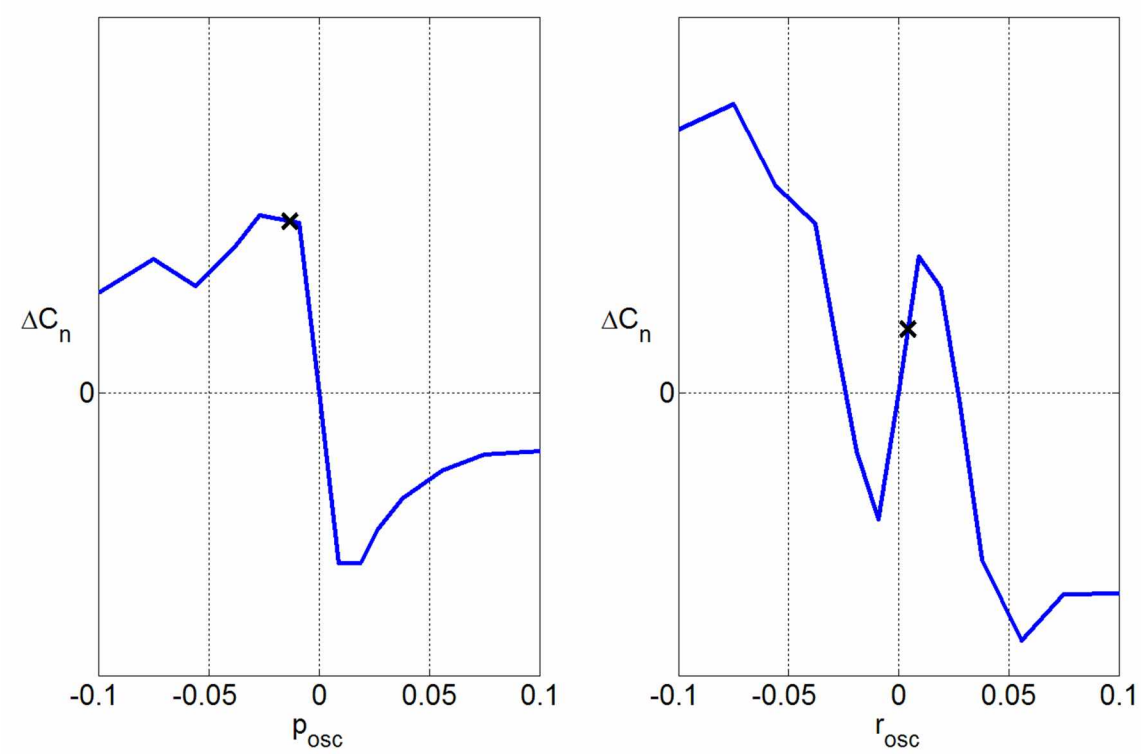

Figure 4.30: Increments to yawing moment coefficient due to oscillatory roll and yaw rates at $\alpha = 40^{-}$.

Similar to the rolling moment, the high-frequency dynamics seen in Figure 4.23 through Figure 4.29 are caused in part by the blending methods using data in the nonlinear regions in the roll and yaw databases. The blending methods often simultaneously use data in the nonlinear regions of the roll and yaw oscillatory data (denoted by "X"s in Figure 4.30), further exacerbating the nonlinearity. This results in large, abrupt variations in the yawing moment seen in Figure 4.23 through Figure 4.29.

Asymmetries in the rotary balance data again play a role in the high-frequency dynamics seen in Figure 4.23 through Figure 4.29, particularly in Figure 4.27 (run

b32r2). The large downward spike in the aerodynamic model occurs just as the aircraft crosses $\beta = 0^-$, where the asymmetries in the rotary data are large. Figure 4.31 shows the static asymmetries present in the yawing moment coefficient for the rotary balance data.

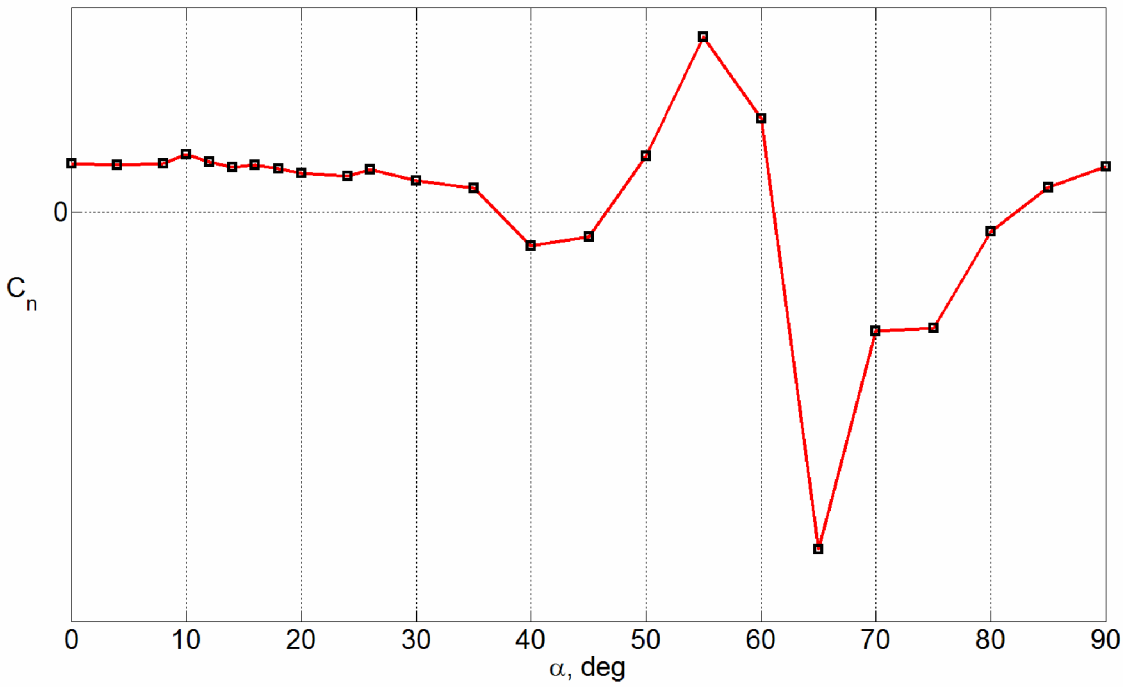

Figure 4.31: Yawing moment coefficient for rotary balance data, $\beta = 0^-$, $\hat{\omega}_{ss} = 0^-$

The asymmetries shown in Figure 4.31 are propagated to the remainder of the dynamic data via the data reduction process, potentially creating nonlinearities that did not exist before.

In addition to the asymmetry issue, the rotary balance data reduction process assumes any difference between the static and dynamic data is entirely due to the angular rate. This also assumes that any nonlinearity in the static data is also present in the dynamic data; i.e., angular rate has no effect on static nonlinearities. This may or may

not be a good assumption, since the flow mechanisms that cause static nonlinearities (e.g. vortical flows) may not be present or have the same effect when the aircraft is rotating. These issues encountered with the rotary balance data reduction highlighted a need to better understand the nonlinear flow characteristics around the aircraft during rotary motion so that an appropriate data reduction method can be implemented.

In summary for this section, the blending methods produced an acceptable match to the free-spin data. Again, using a blending method produced better results than using forced oscillation or rotary balance data alone. Similar to the rolling moment coefficient, high-frequency dynamics are present in the aerodynamic model output, caused by a combination of the blending methods and forced oscillation data and the rotary balance data reduction process.

4.2.4 Side Force Coefficient

The following section shows results for the side force coefficient. There is little dynamic effect on the side force and as a result, all of the blending methods yielded very good results. The first set of figures is intended to compare the modeling methods to free-spin data and to each other. Free-spin data from run b29r11 is used.

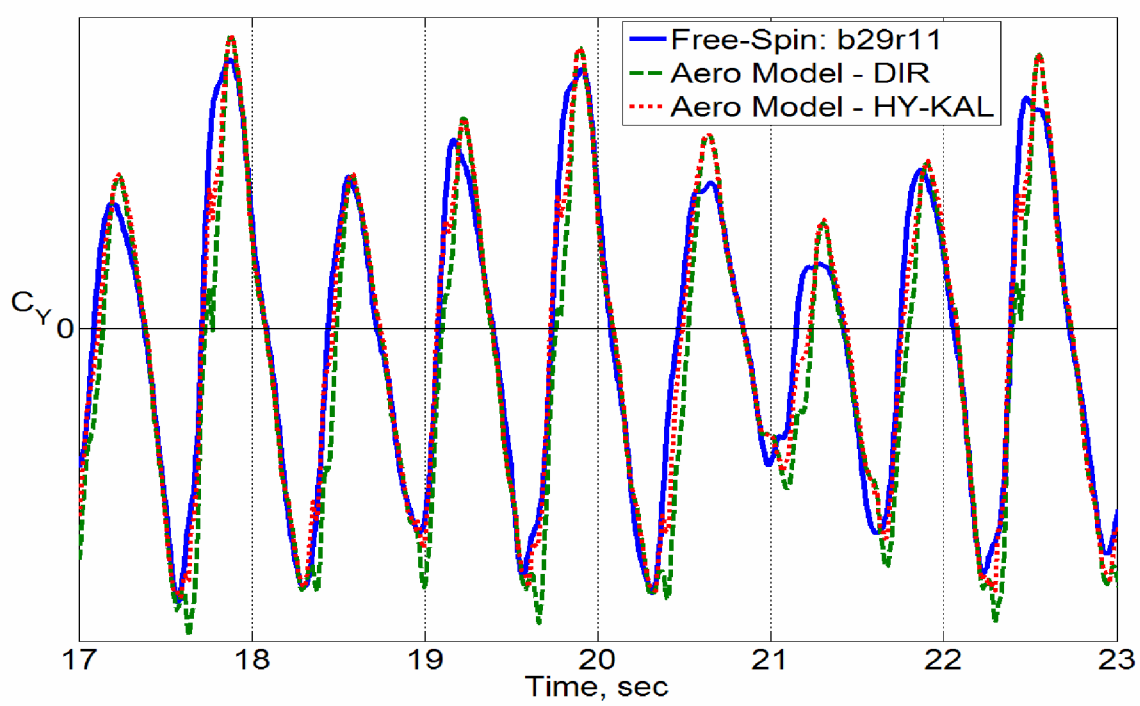

Figure 4.32: Comparison of side force coefficient for free-spin data b29r11 and aerodynamic model using Direct Resolution and Hybrid Kalviste blending.

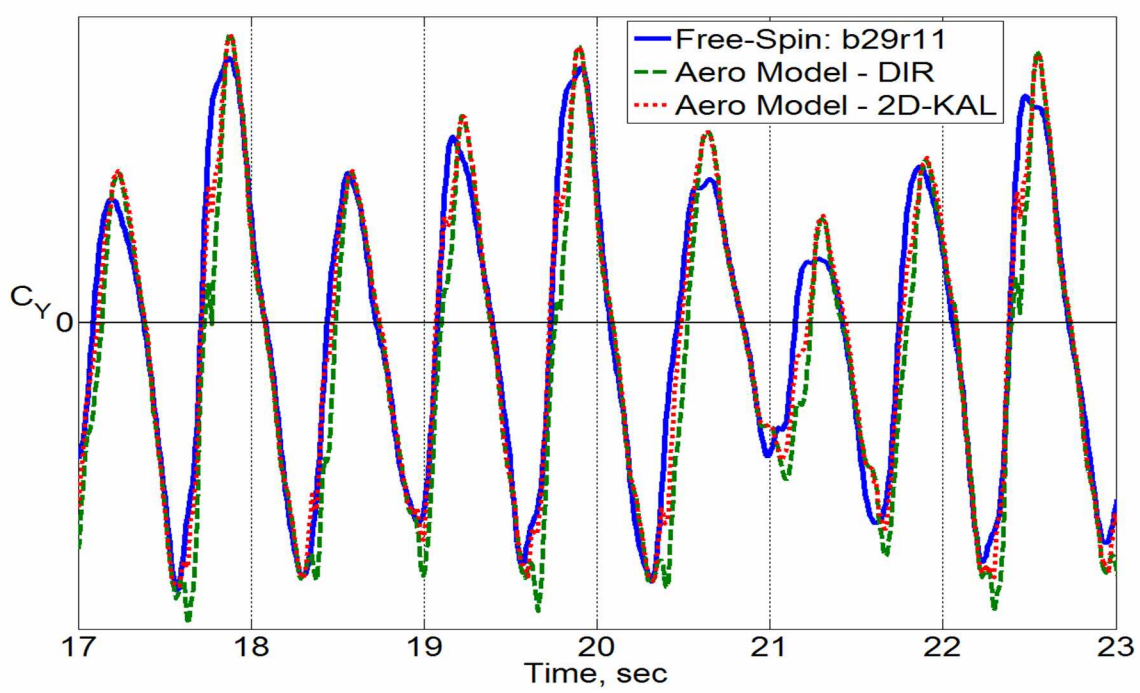

Figure 4.33: Comparison of side force coefficient for free-spin data b29r11 and aerodynamic model using Direct Resolution and 2D Kalviste blending.

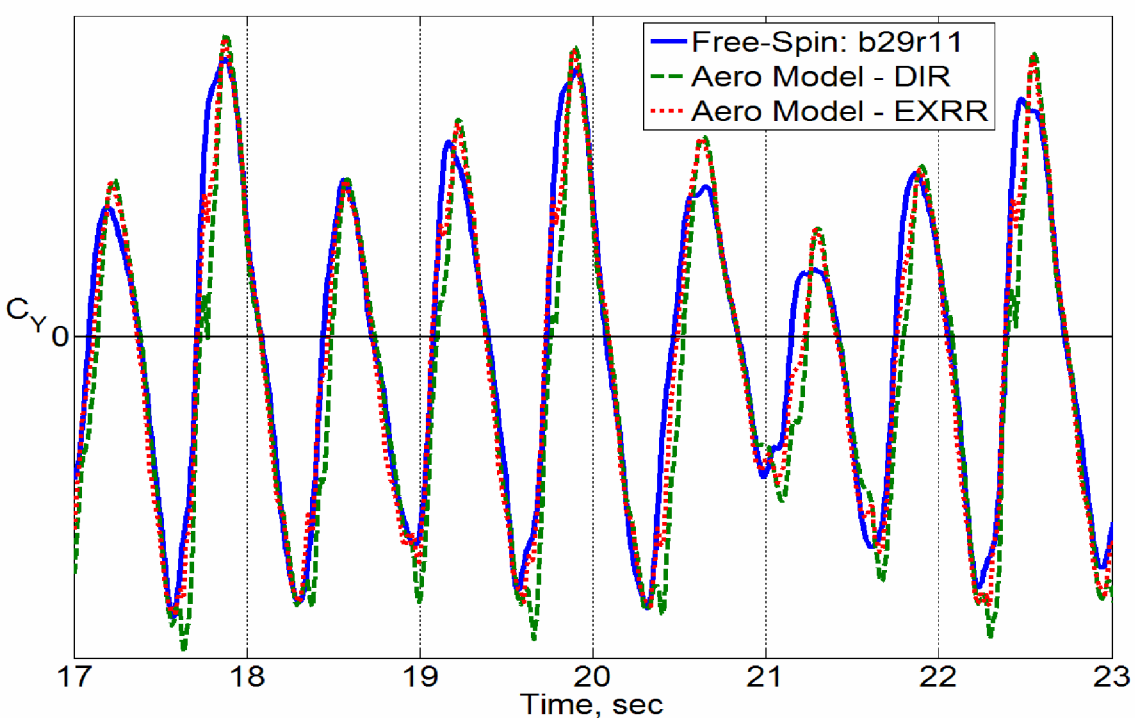

Figure 4.34: Comparison of side force coefficient for free-spin data b29r11 and aerodynamic model using Direct Resolution and Excess Roll Rate blending.

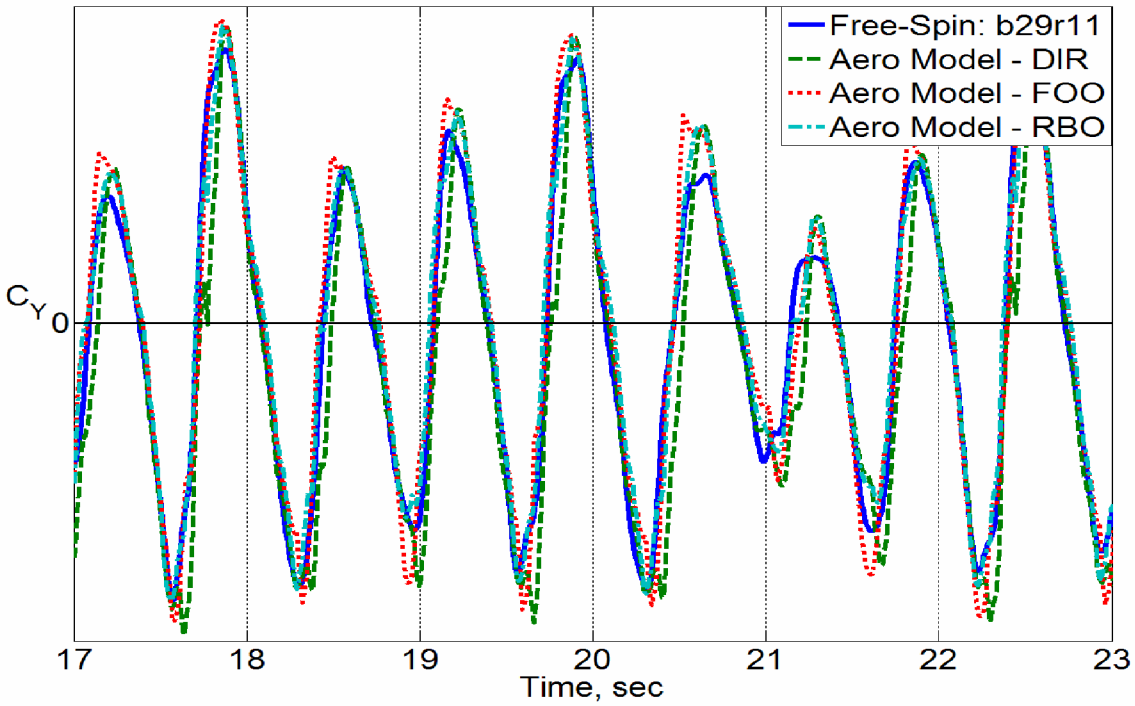

Figure 4.35: Comparison of side force coefficient for free-spin data b29r11 and aerodynamic model using Direct Resolution blending and using forced oscillation data only and using rotary balance data only.

The results shown in Figure 4.32 through Figure 4.35 are similar to those obtained in other free-spin data runs. A sampling of these results is given in the following set of figures:

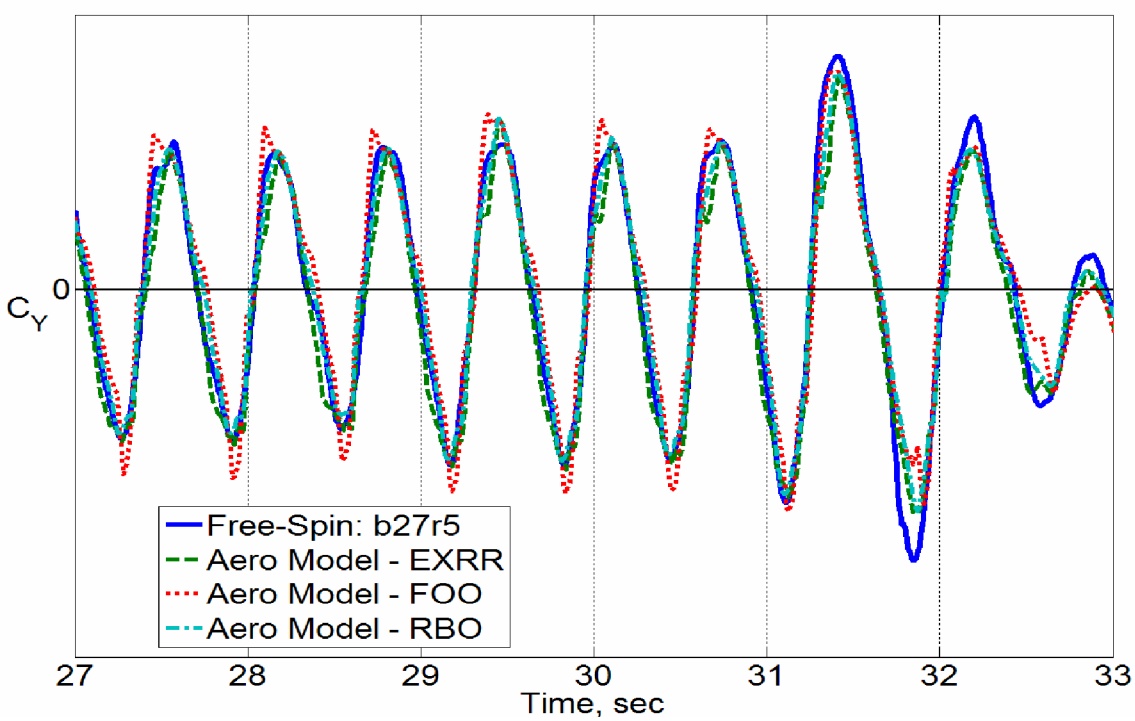

Figure 4.36: Comparison of side force coefficient for free-spin data b27r5 and aerodynamic model using Excess Roll Rate blending and using forced oscillation data only and using rotary balance data only.

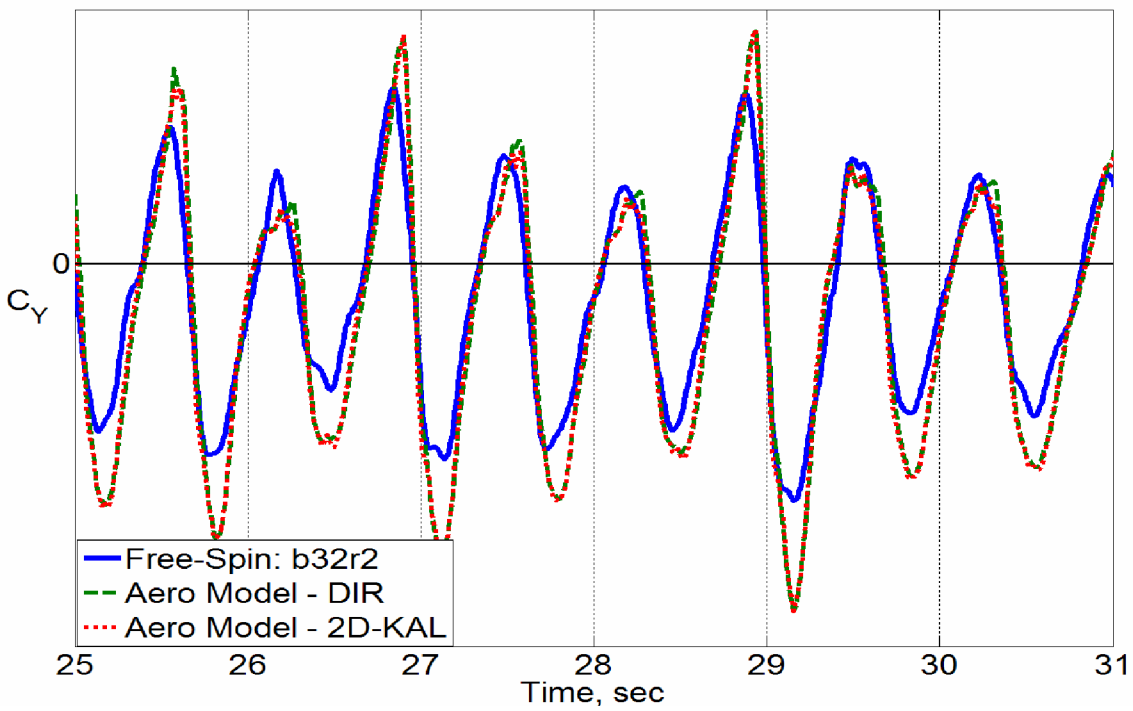

Figure 4.37: Comparison of side force coefficient for free-spin data b32r2 and aerodynamic model using Direct Resolution and 2D Kalviste blending.

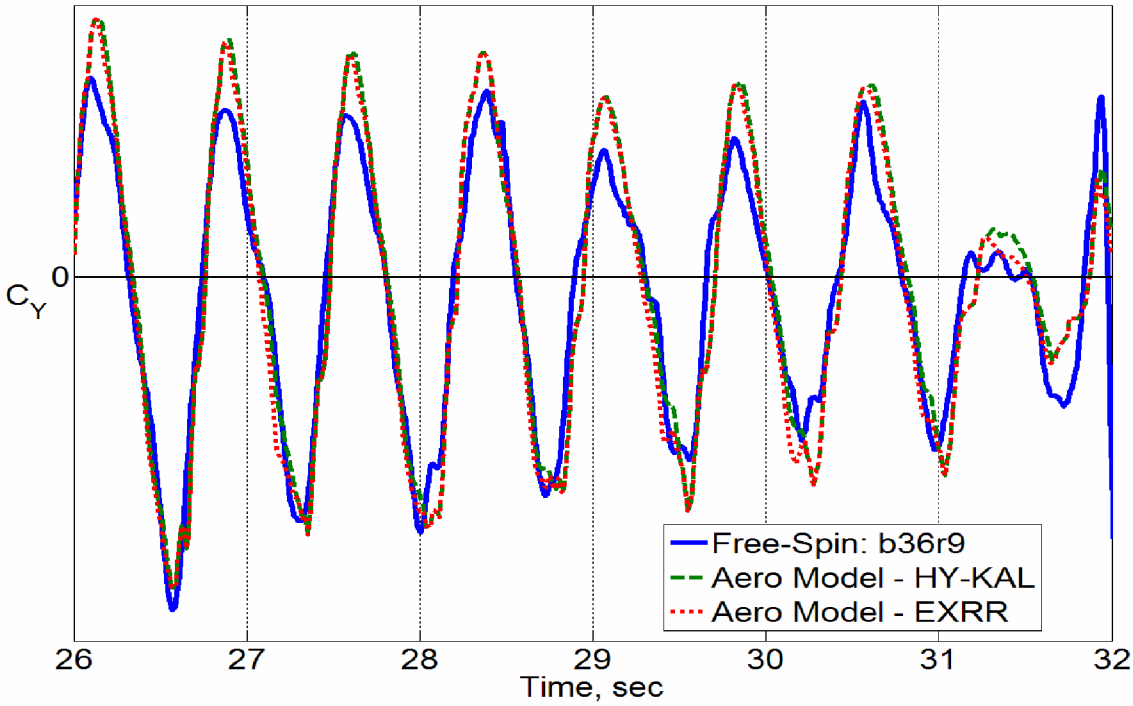

Figure 4.38: Comparison of side force coefficient for free-spin data b36r9 and aerodynamic model using Hybrid Kalviste and Excess Roll Rate blending.

As seen in Figure 4.32 through Figure 4.38, little difference can be discerned between the blending methods and even between the blending methods and using forced oscillation or rotary balance data alone. The primary reason is that there is little effect of angular rate on side force, so differences between blending methods are negligible. The good match shown in Figure 4.32 through Figure 4.38 suggests the aerodynamic model can accurately predict side forces during a spin.

An important conclusion of the results shown in Figure 4.32 through Figure 4.38 is that this indicates that there are few Reynold's number effects present for flow over the fuselage. As discussed in Section 3.5.1.3, the Reynold's number difference between the wind tunnel data the aerodynamic model is based on versus the free-spin wind tunnel test is relatively small. The excellent match shown in the preceding figures indicate there are few effects due to Reynold's number differences between wind tunnel tests for flow over the fuselage. Reynold's number effects for flow over the wings cannot be assessed using the side force coefficient.

In summary for this section, there is very little dynamic effect on the side force coefficient, and as a result, all of the blending methods gave similar results. The overall match between the aerodynamic model and the free-spin data was very good, indicating the aerodynamic model can accurately model side force during a spin.

4.2.5 Lift Force Coefficient

The following section shows results for the lift force coefficient. The overall match was relatively good, given that the lift coefficient is often not predicted well in dynamic situations. The Direct Resolution and Hybrid Kalviste methods yielded the best match, while 2D Kalviste and Excess Roll Rate both had poor results. Again, using a

blending method yielded better results than using forced oscillation or rotary balance data alone. The first set of figures is intended to compare the modeling methods to free-spin data and to each other. Free-spin data from run b29r11 is used.

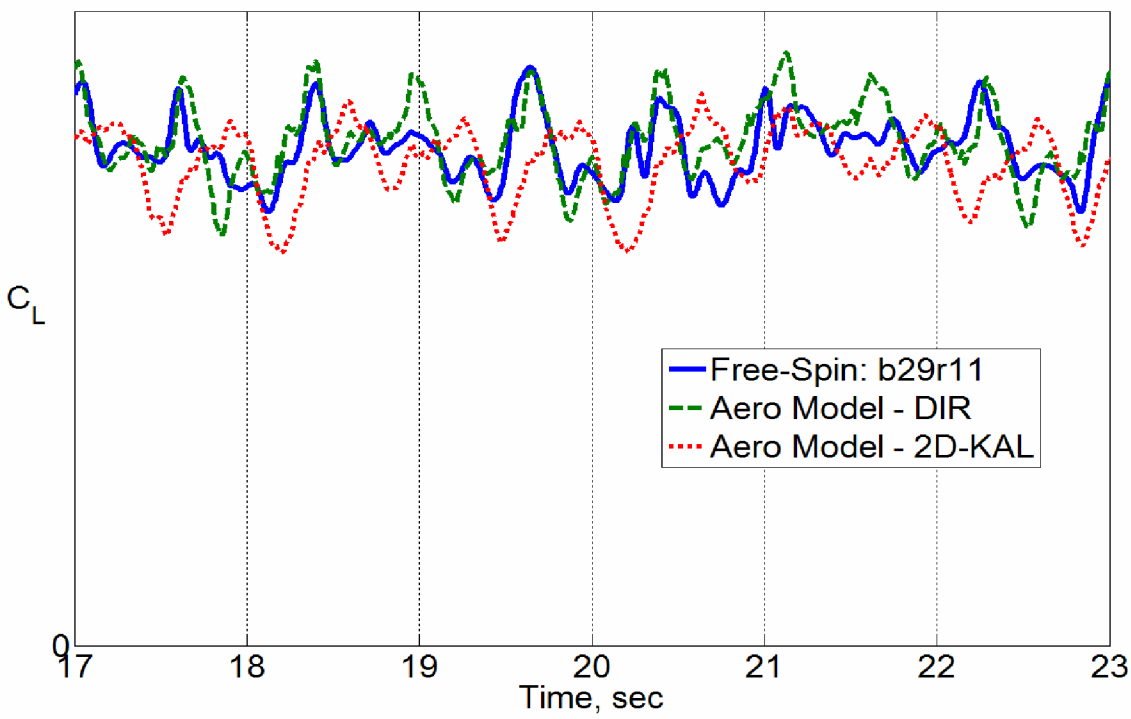

Figure 4.39: Comparison of lift force coefficient for free-spin data b29r11 and aerodynamic model using Direct Resolution and 2D Kalviste blending.

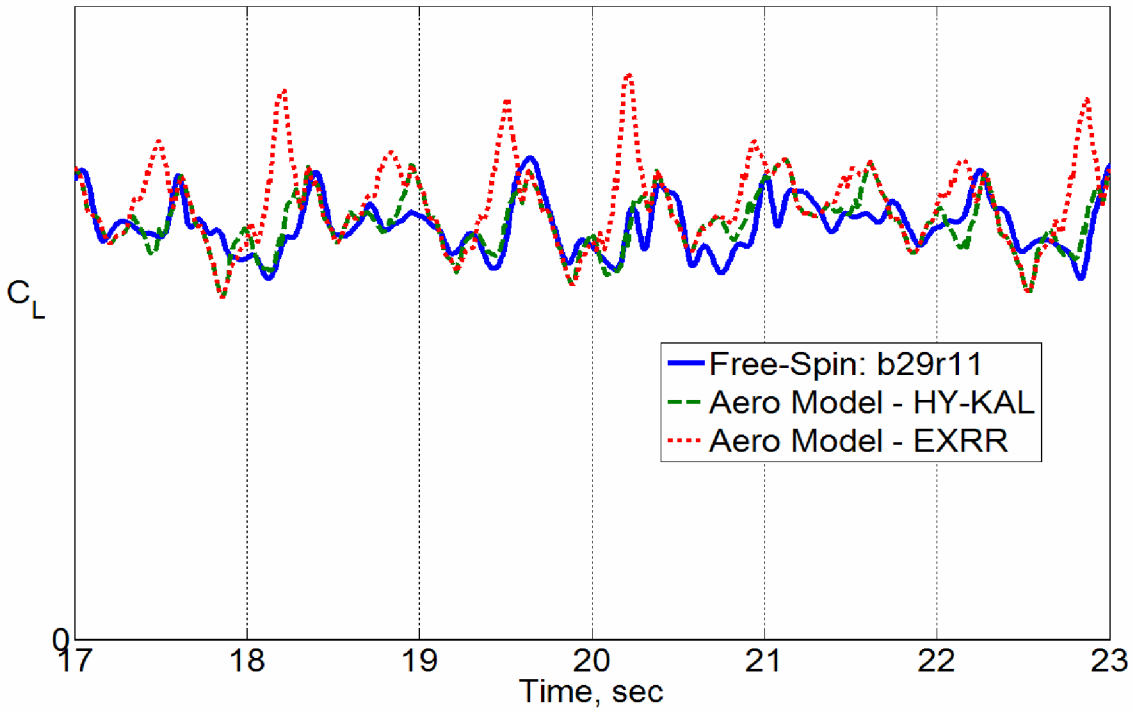

Figure 4.40: Comparison of lift force coefficient for free-spin data b29r11 and aerodynamic model using Hybrid Kalviste and Excess Roll Rate blending.

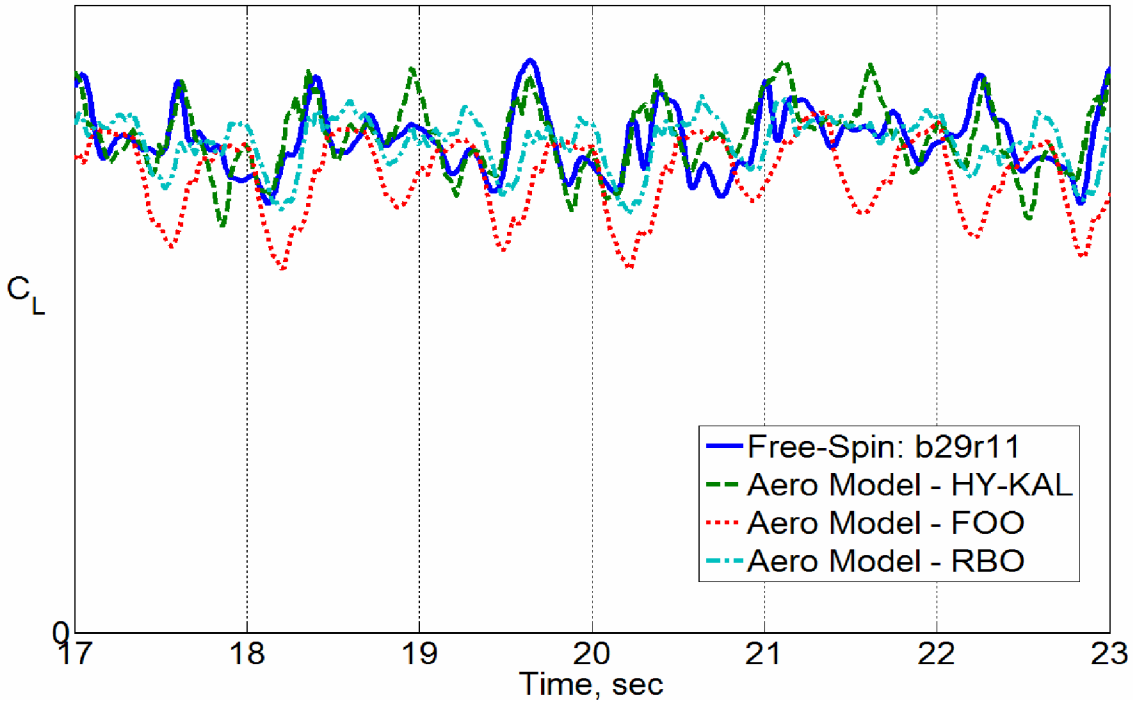

Figure 4.41: Comparison of lift force coefficient for free-spin data b29r11 and aerodynamic model using Hybrid Kalviste blending and using forced oscillation data only and using rotary balance data only.

As can be seen in Figure 4.39 through Figure 4.41, the Direct Resolution and Hybrid Kalviste methods provide a better match than 2D Kalviste, Excess Roll Rate, and using forced oscillation or rotary balance data alone. The latter methods have a poor match of both the amplitude and frequency of oscillation. These results were similar to those obtained in other free-spin data runs, a sample of which is shown in the following figures.

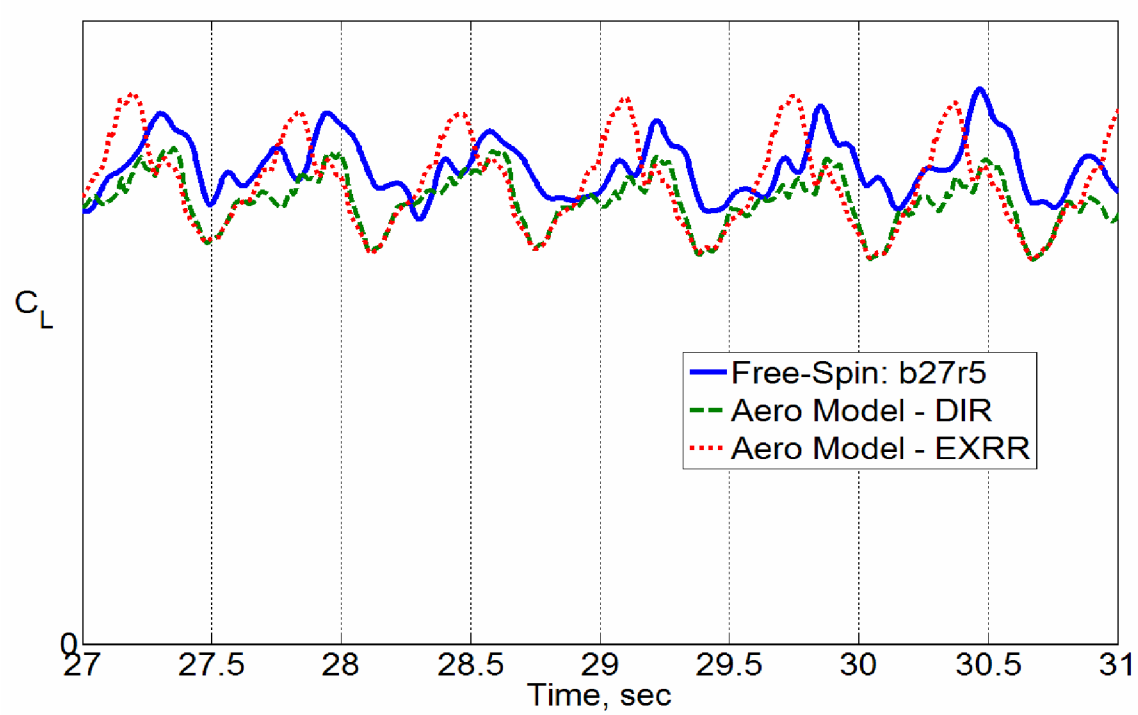

Figure 4.42: Comparison of lift force coefficient for free-spin data b27r5 and aerodynamic model using Direct Resolution and Excess Roll Rate blending.

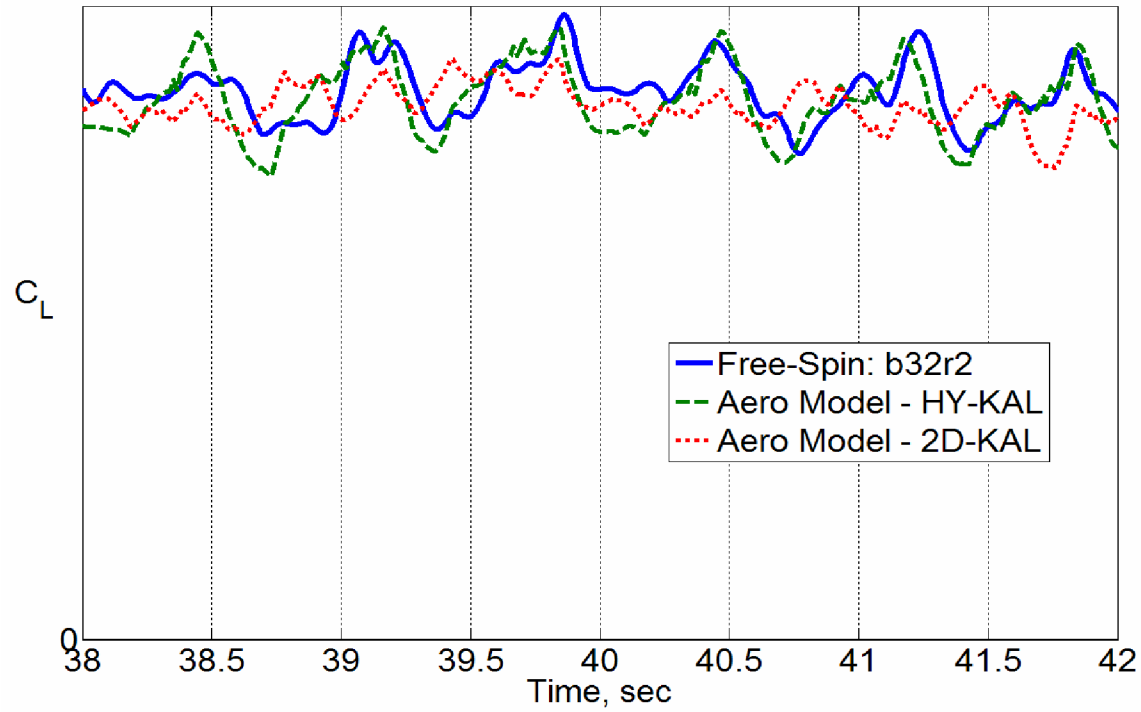

Figure 4.43: Comparison of lift force coefficient for free-spin data b32r2 and aerodynamic model using Hybrid Kalviste and 2D Kalviste blending.

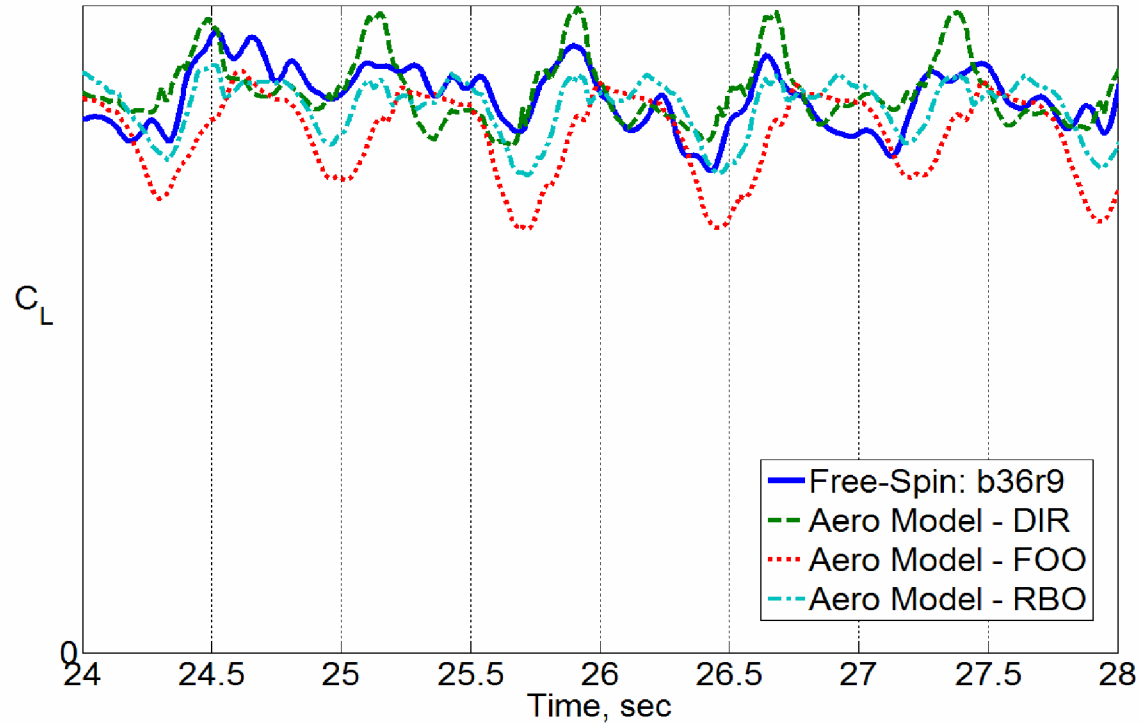

Figure 4.44: Comparison of lift force coefficient for free-spin data b36r9 and aerodynamic model using Direct Resolution blending and using forced oscillation data only and using rotary balance data only.

The mismatch in Figure 4.39 through Figure 4.44 is best examined by first splitting the lift coefficient into its component parts. The lift coefficient can be calculated by the following equation

$$C_L = C_X \sin\alpha - C_Z \cos\alpha \tag{4.7}$$

Figure 4.45 and Figure 4.46 show a comparison of C_X and C_Z between free-spin data and the aerodynamic model using Direct Resolution blending. The scales on the figures are the same to facilitate comparison.

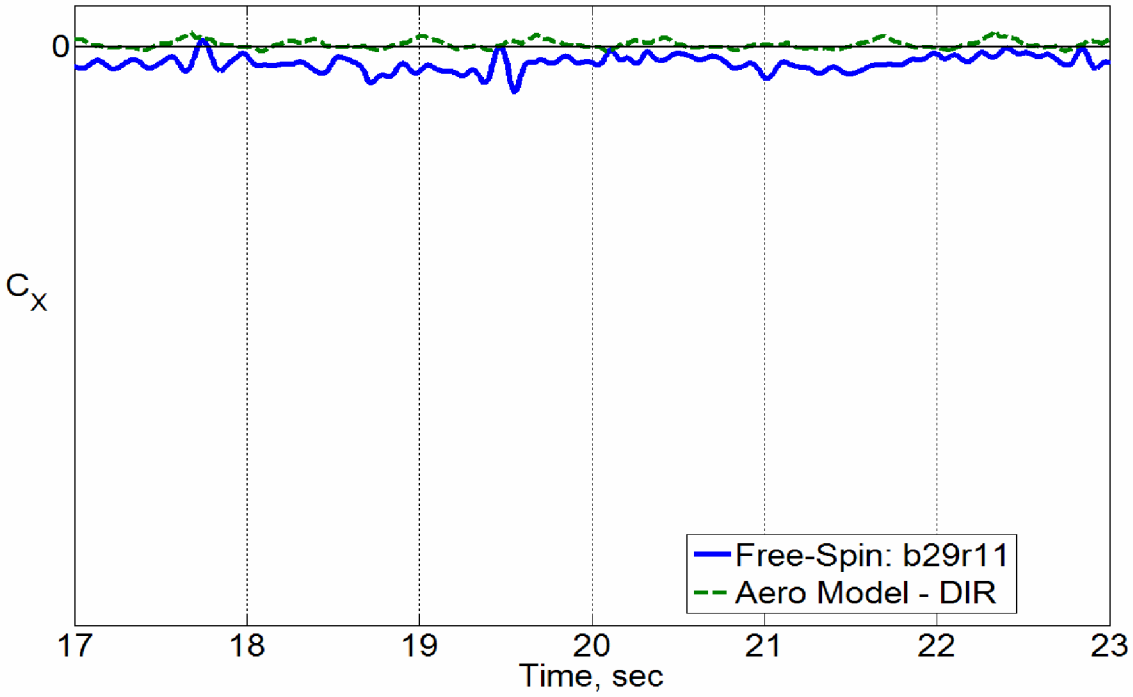

Figure 4.45: Comparison of C_X for free-spin data b29r11 and aerodynamic model using Direct Resolution blending.

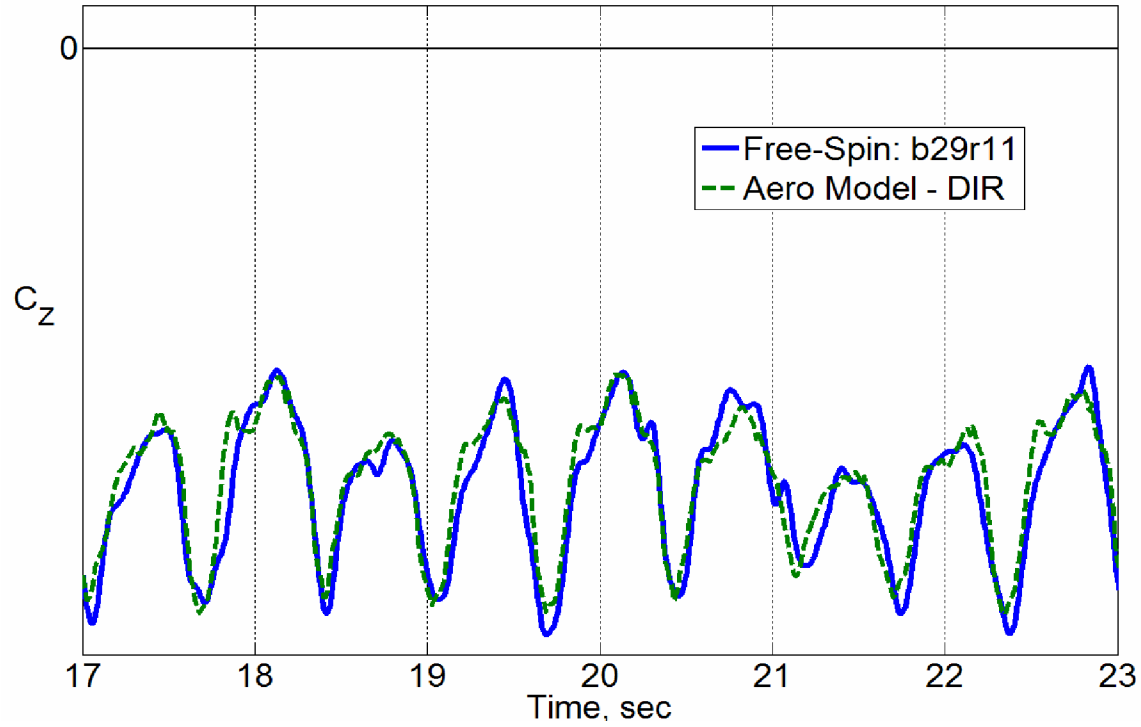

Figure 4.46: Comparison of C_Z for free-spin data b29r11 and aerodynamic model using Direct Resolution blending.

Note in Figure 4.45 there appears to be a fairly constant mismatch between the free-spin data and the aerodynamic model. This error, combined with the relatively small errors seen in Figure 4.46, create the mismatch seen in the lift coefficient. The error in C_X could possibly be explained by the tether pulling on the model during the free-spin test. This possibility was discussed in Section 4.2.2, and as shown in Figure 4.22, the needed tether force to account for the pitching moment bias and the C_X bias are not the same. However, this does not rule out the possibility of the tether exerting force on the model, since it is impossible to separate the error caused by the tether and error from other sources.

In addition, as discussed with the pitching moment, the blending methods are not aimed at pitch-axis motions, and the only dynamic effects on C_X and C_Z are from pitch

rate and rotary motion. As seen with the pitching moment, the 2D Kalviste method produces poor results, again in part due to the pitch axis effects being double counted, as discussed in Section 4.2.2.

Finally, the mismatch in the lift coefficient between the free-spin data and the aerodynamic model could be partly due to Reynold's number differences between wind tunnel tests. While Reynold's number effects were expected to be minimal due to the similar Reynold's numbers between wind tunnel tests, these effects are very difficult to quantify and were beyond the scope of this research.

In summary for this section, the Direct Resolution and Hybrid Kalviste methods produced the best match of the free-spin data. The 2D Kalviste and Excess Roll Rate methods, along with using forced oscillation or rotary balance data alone produced the poorest results. Errors in the aerodynamic model were traced primarily to C_X, which could be the result of the tether exerting force on the model during the free-spin test.

4.2.6 Drag Force Coefficient

The following section shows results for the drag force coefficient. There is little dynamic effect on the drag force, and consequently all of the blending methods gave similar results. Overall the match was very good, even when no blending method was used. The first set of figures is intended to compare the modeling methods to free-spin data and to each other. Free-spin data from run b29r11 is used.

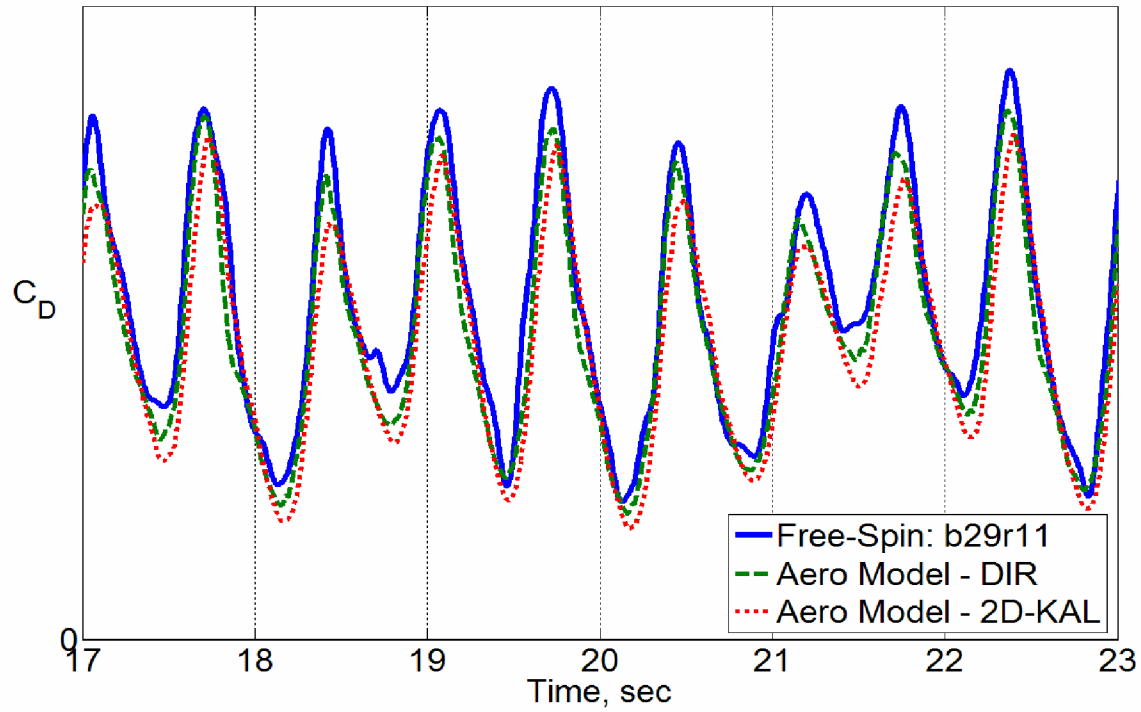

Figure 4.47: Comparison of drag force coefficient for free-spin data b29r11 and aerodynamic model using Direct Resolution and 2D Kalviste blending.

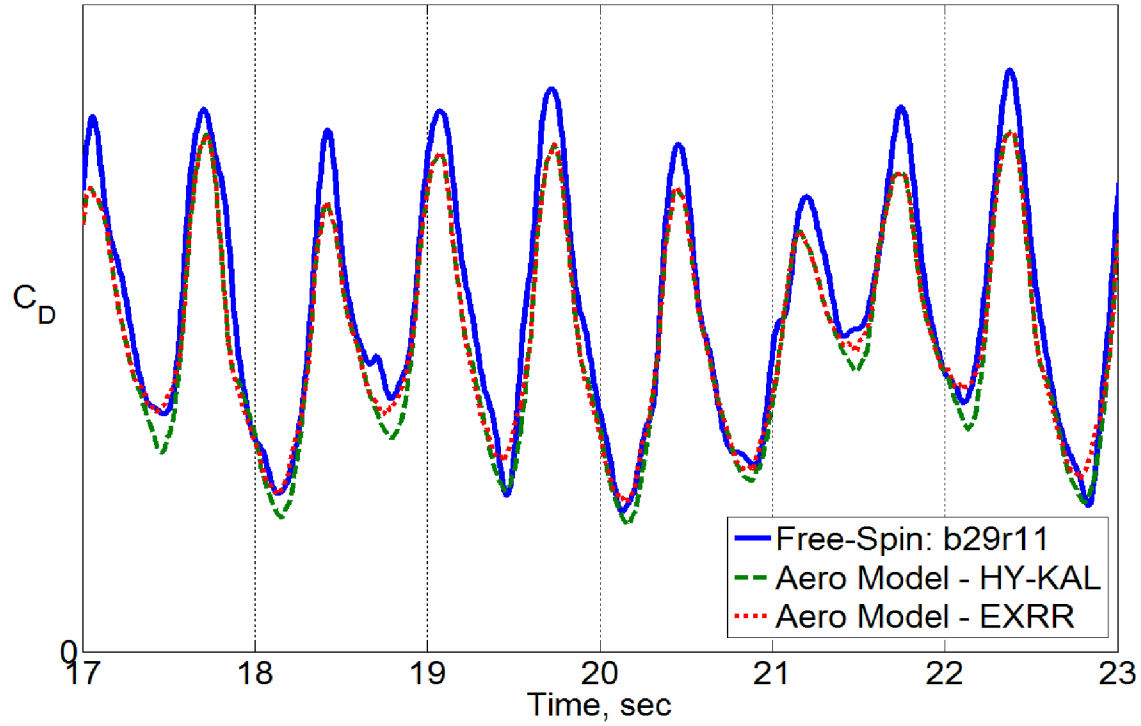

Figure 4.48: Comparison of drag force coefficient for free-spin data b29r11 and aerodynamic model using Hybrid Kalviste and Excess Roll Rate blending.

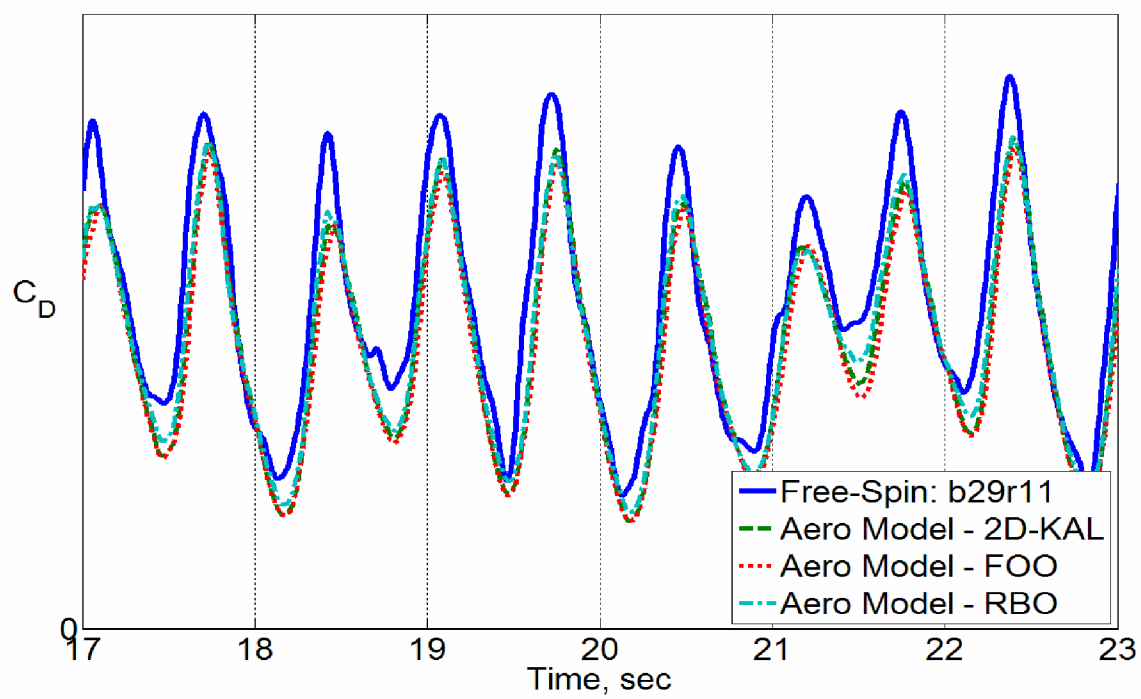

Figure 4.49: Comparison of drag force coefficient for free-spin data b29r11 and aerodynamic model using 2D Kalviste blending and using forced oscillation data only and using rotary balance data only.

As can be seen in Figure 4.47 through Figure 4.49, the overall match is very good, and few differences can be seen between any of the modeling methods used. The aerodynamic model matches the frequency of the motion almost exactly, but has a slightly different amplitude than the free-spin data. This mismatch can be traced primarily to the error in C_Z, but also in the error in C_X, shown in Figure 4.45 and Figure 4.46. Similar to the lift coefficient, the drag coefficient is a combination of the x and z-axis coefficients.

$$C_D = -C_X \cos\alpha - C_Z \sin\alpha \tag{4.8}$$

Note that the above equation is the drag coefficient in the stability axis, often used during wind tunnel testing. By examining Figures Figure 4.46 and Figure 4.47, the worst mismatches in C_D can be correlated with the worst mismatches in C_Z. However, as

noted above, the bulk of C_Z and thusly C_D is made up by the static aerodynamics, so the modeling methods studied had little effect on the overall drag.

In addition, the mismatch in the drag coefficient between the free-spin data and the aerodynamic model could be partly due to Reynold's number differences between wind tunnel tests. While Reynold's number effects were expected to be minimal due to the similar Reynold's numbers between wind tunnel tests, these effects are very difficult to quantify and were beyond the scope of this research.

In summary for this section, the aerodynamic model yielded a good match to the free-spin data no matter what blending method, if any, was used. The frequency of the oscillation was matched almost exactly, and with only a slight mismatch in the amplitude.

4.2.7 Summary of Aerodynamic Coefficient Matching

As a method to quantify the match of the aerodynamic model to the free-spin data, the RMS errors (relative to the free-spin data) of each aerodynamic coefficient were computed for each free-spin run listed in Table 4.1. These data were then averaged to yield the mean RMS error, which was used as a measure of the overall performance of the aerodynamic model. The results are shown below in Figure 4.50.

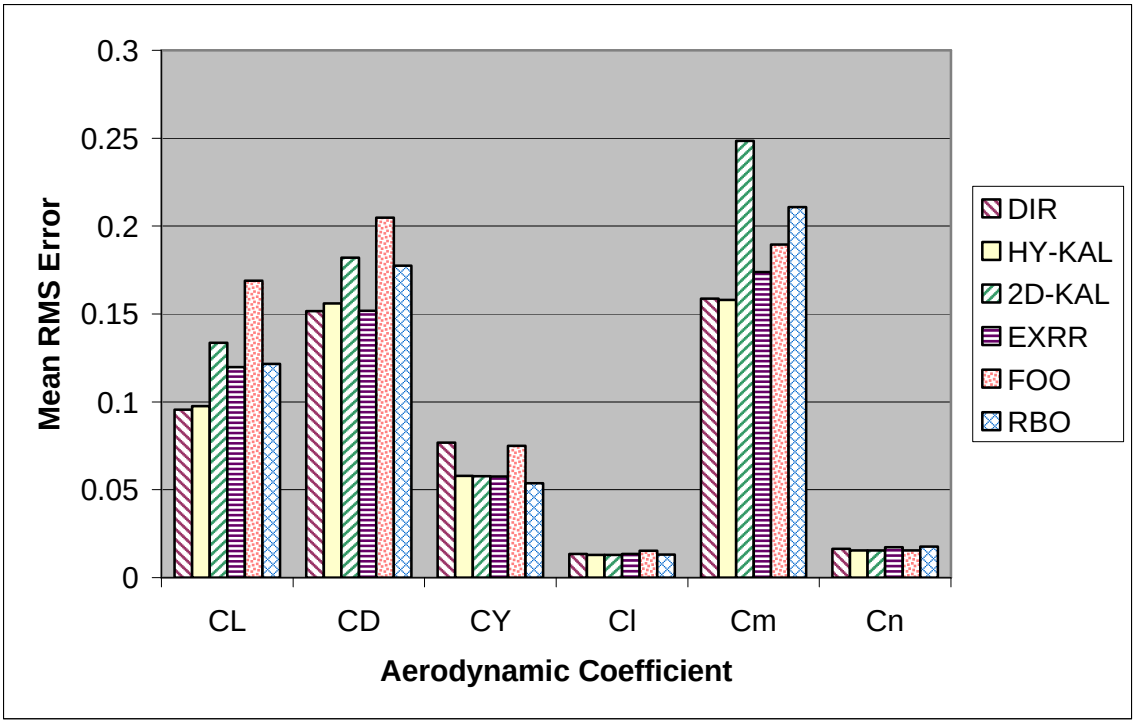

Figure 4.50: Mean RMS error of each axis of the aerodynamic model.

Figure 4.50 shows that using the Direct Resolution and Hybrid Kalviste methods generally result in the lowest mean RMS error. Use of a blending method generally produced better results than using forced oscillation or rotary balance data alone, with the notable exception of the 2D Kalviste method.

High-frequency dynamics noted in the aerodynamic model output in the rolling and yawing moment coefficients had two primary sources: First, the blending methods look up oscillatory data at angular rates not representative of the actual aircraft motion. This becomes a significant issue when there are nonlinearities in the dynamic wind tunnel data, as is the case for the roll and yaw forced oscillation data at angles of attack above ~35°. Second, the rotary balance data reduction process propagates any asymmetries in the static data through the dynamic data. Significant asymmetries were present in the

rolling moment and yawing moment static rotary balance data at angles of attack above ~40°, which contributed to high-frequency dynamics in the aerodynamic model output.

Mismatch between the pitching moment and C_X was theorized to be partially due to the tether attached to the free-spin model exerting a force during the free-spin test. Analysis of the data indicated that this was a possibility, but was not conclusive.

The forced oscillation database did not contain data at large enough nondimensional rates for modeling spins. The angular rates achieved in a spin were often greater than the database limits. This was a significant issue for using forced oscillation data only, as the majority of the spin requires extrapolation. This was not an issue for the roll and yaw databases when a blending method was used, but was still an issue for the pitch database.

4.3 Simulation Results

The previous section provided a detailed and direct validation of the aerodynamic model using free-spin data. However, since the primary use of the aerodynamic model is for simulation, it is important to compare a simulation using the aerodynamic model to the validation data. Section 4.3.1 shows time history comparisons between the simulation and free-spin data. As mentioned in Section 3.4, precise time history comparisons for long duration, highly nonlinear flight motions such as spins are unrealistic since very small differences in the forcing functions (i.e. the aerodynamic model) can lead to large differences in the integrated response. The focus of the comparison was verifying that the simulation captured the general characteristics of the spin. This is more completely explored in Section 4.3.2, which shows comparisons of the spin mode characteristics obtained from the simulation and from free-spin data.

Comparisons of simulation results using the Direct Resolution, Kalviste, and Excess Roll Rate methods are shown. Only limited simulation results using forced oscillation data only are shown, as this method often drove the simulation unstable, likely due to the limits of the forced oscillation database being exceeded. Simulation results using rotary balance data only are not shown as this method is not suitable for simulation of general aircraft motion and almost always drives the simulation unstable.

4.3.1 Time History Comparison

A commonly used method to determine if a simulation captures the character of the aircraft motion is to compare simulator time histories to flight test data time histories. As discussed previously, precisely matching time histories is not realistic for nonlinear maneuvers such as spins. Nonlinear maneuvers often have large differences in integrated response for small changes in inputs, making comparisons of time histories from the ideal simulation environment to real-world wind tunnel data difficult.

This section compares time histories of key aircraft motion states obtained from simulated fully developed spins and from free-spin data. Only test run b27r5 will be compared in this section; a more complete comparison of spin mode characteristics is given in the next section. The next three figures show time histories of Euler angles from the free-spin test and simulation results for test run b27r5.

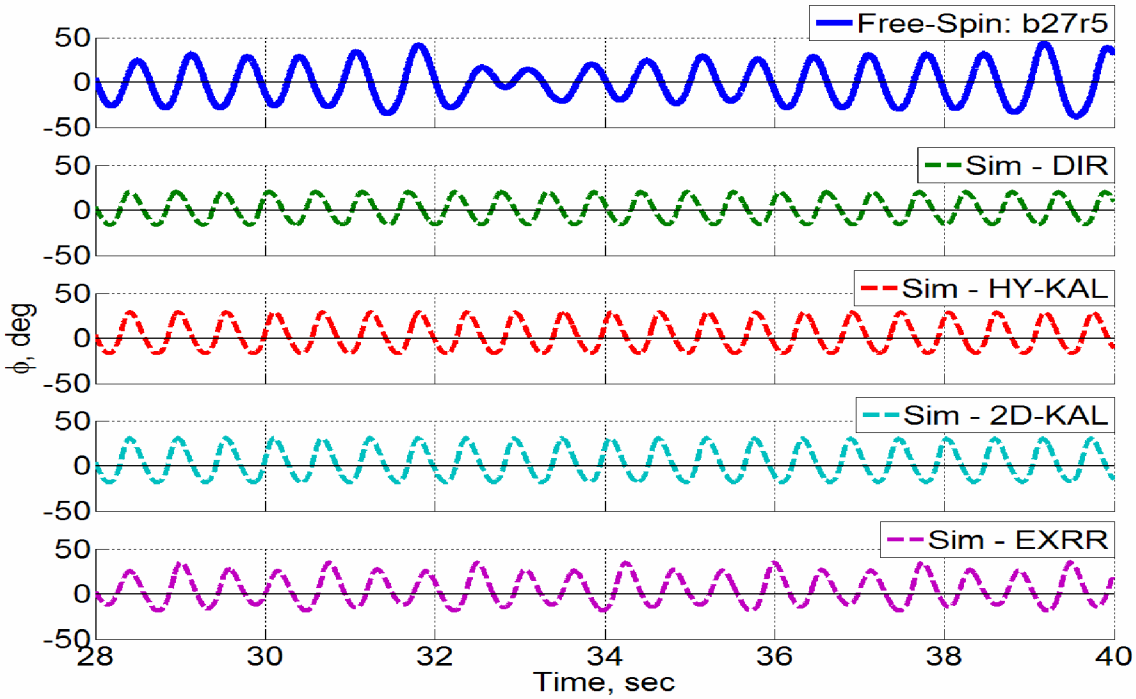

Figure 4.51: Roll angle time history from free-spin run b27r5 and simulation results.

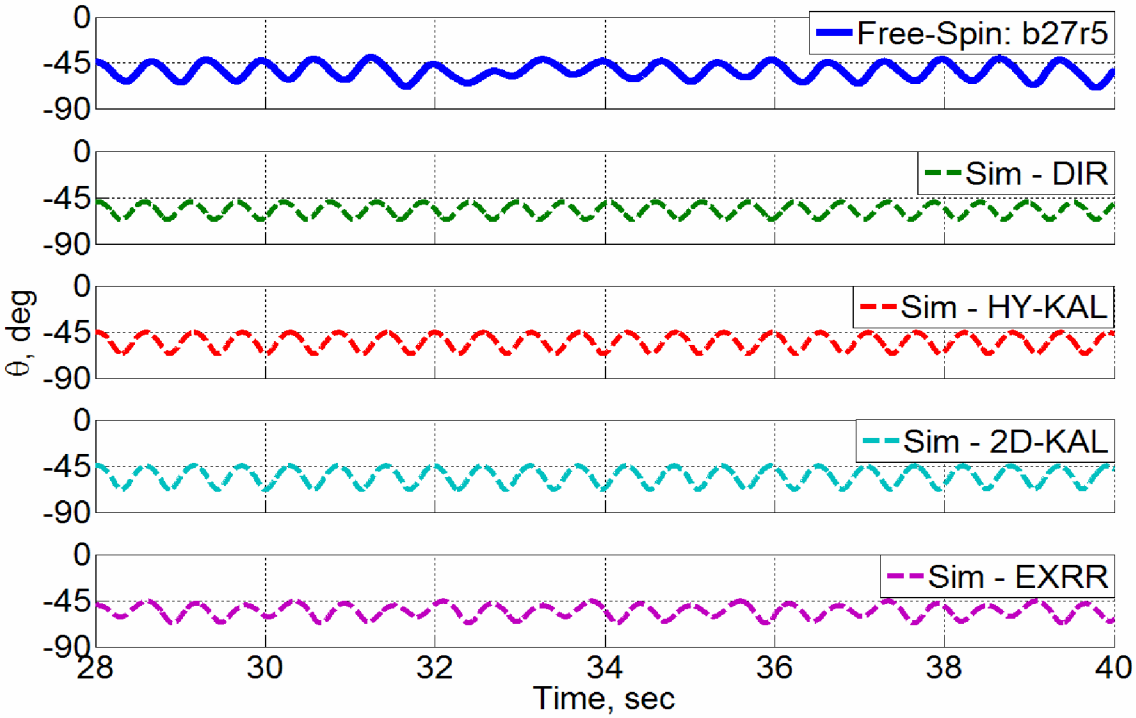

Figure 4.52: Pitch angle time history from free-spin run b27r5 and simulation results.

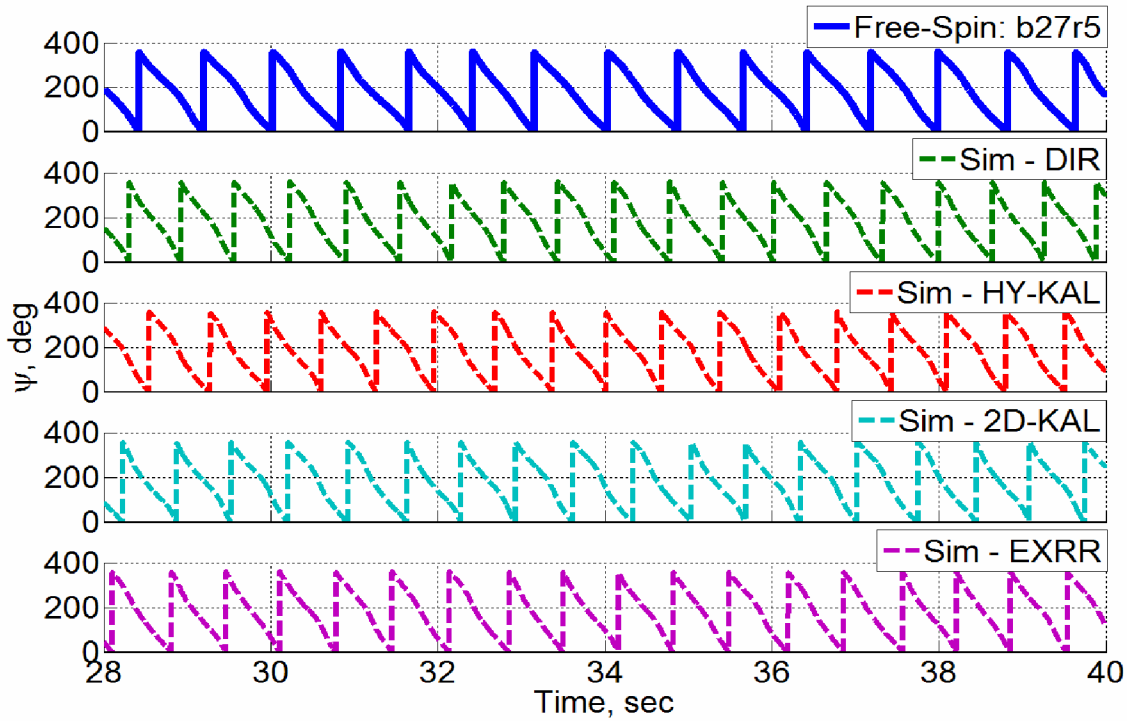

Figure 4.53: Yaw angle time history from free-spin run b27r5 and simulation results.

It is clear in Figure 4.51 through Figure 4.53 that the simulation using any of the blending methods captures the general oscillatory character of the free-spin data. However simulation results using the Direct Resolution method were typically the least oscillatory and also had a faster spin rate than observed in the free-spin data.

Figure 4.54 through Figure 4.56 compare the body-axis angular rates. Again, note that the simulation results typically capture the general oscillatory character of the free-spin data. The simulation results showed a faster roll rate with less oscillation than the free-spin data. In addition, the magnitude of the simulated pitch rate oscillations was less than what was exhibited in the free-spin data. The simulated yaw rate matched the free-spin data quite well.

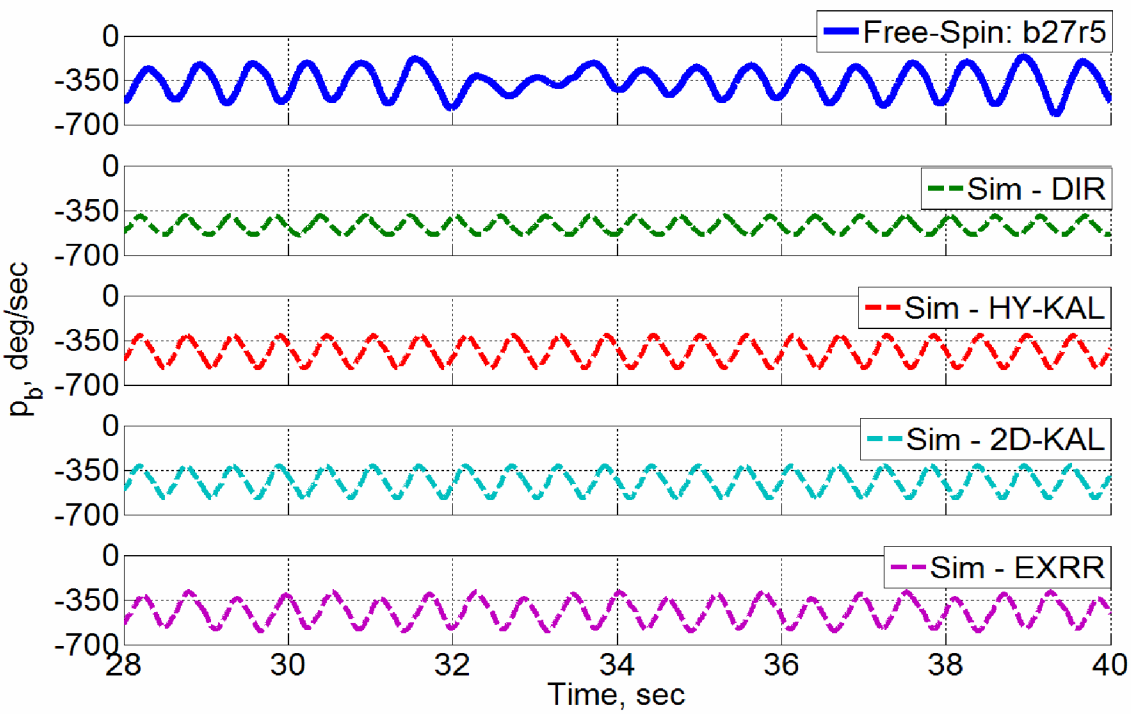

Figure 4.54: Body-axis roll rate time history from free-spin run b27r5 and simulation results.

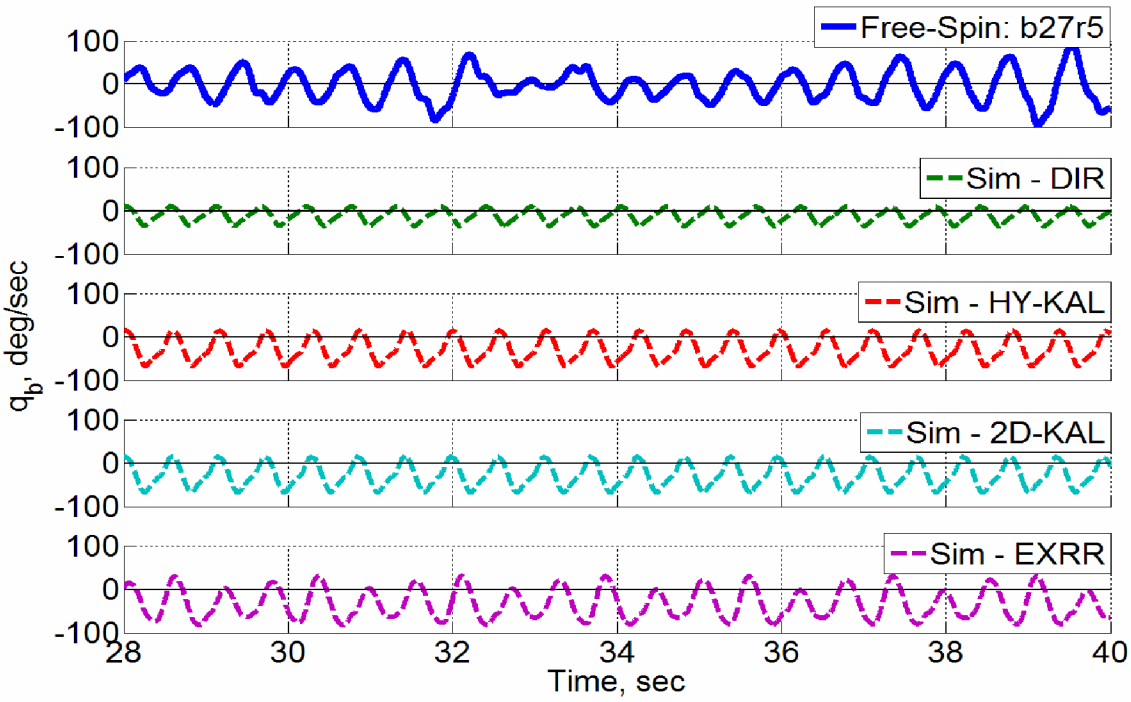

Figure 4.55: Body-axis pitch rate time history from free-spin run b27r5 and simulation results.

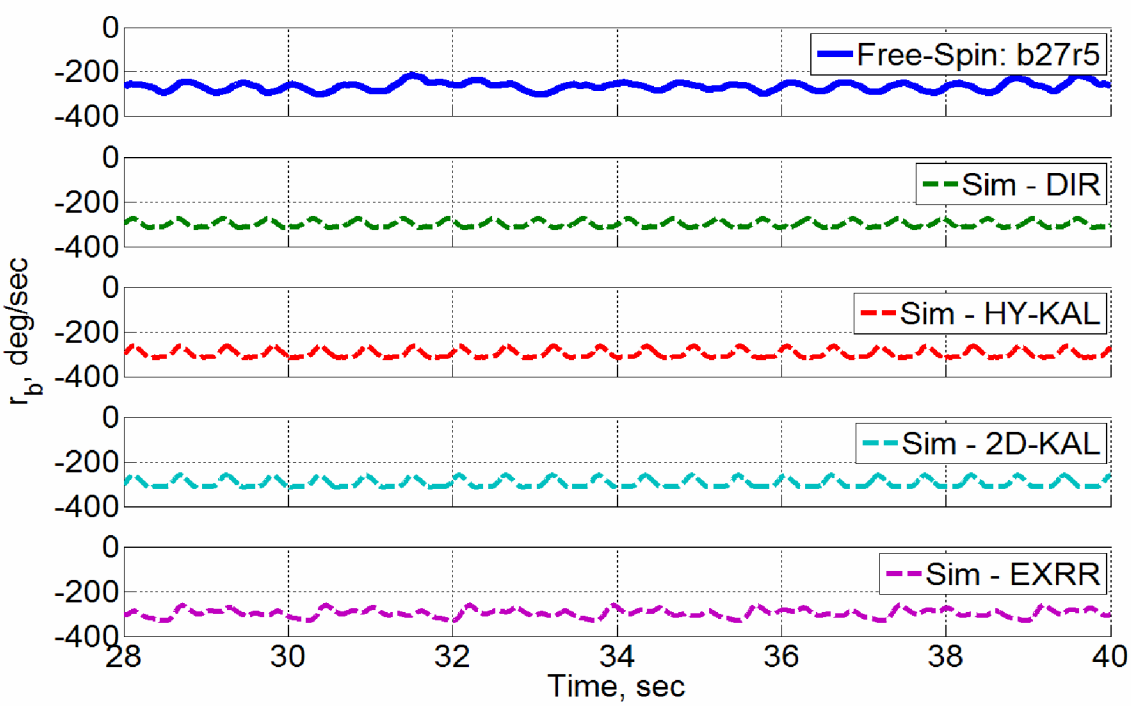

Figure 4.56: Body-axis yaw rate time history from free-spin run b27r5 and simulation results.

Figure 4.57 through Figure 4.59 show time histories for the angle of attack and sideslip angle, as well as the angle of attack – sideslip angle trace. Similar to the Euler angles and body-axis rates, the simulation captures the main features of the free-spin data, but is not as oscillatory. In particular, note that the Direct Resolution method has the smallest magnitude oscillations in general and all of the methods under-predict the amplitude of the sideslip angle oscillations. This fact is most evident in Figure 4.59, which shows the angle of attack – sideslip angle trace; note how the simulation results have a much tighter oscillation pattern than the free-spin data.

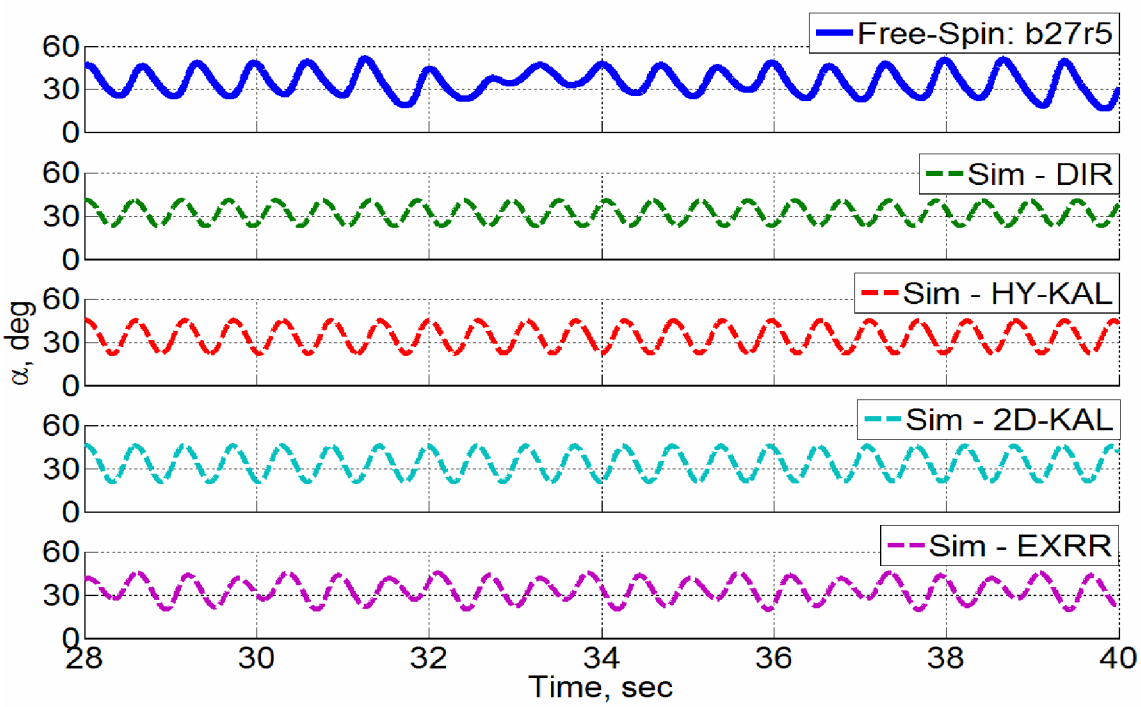

Figure 4.57: Angle of attack time history from free-spin run b27r5 and simulation results.

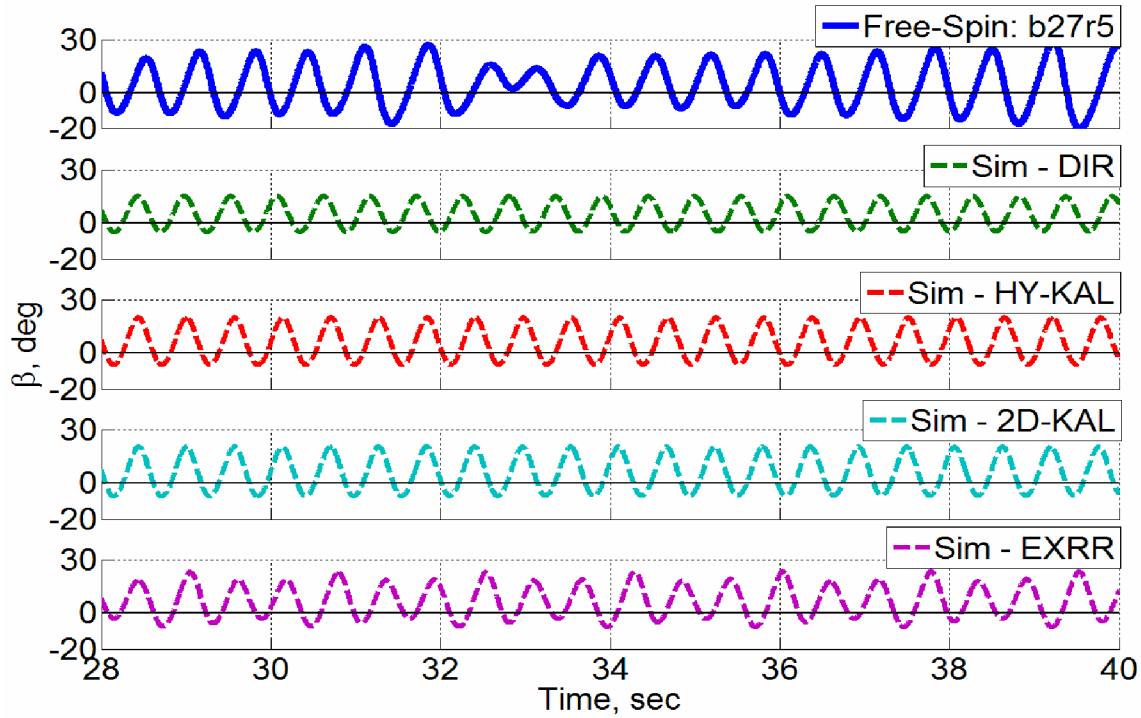

Figure 4.58: Sideslip angle time history from free-spin run b27r5 and simulation results.

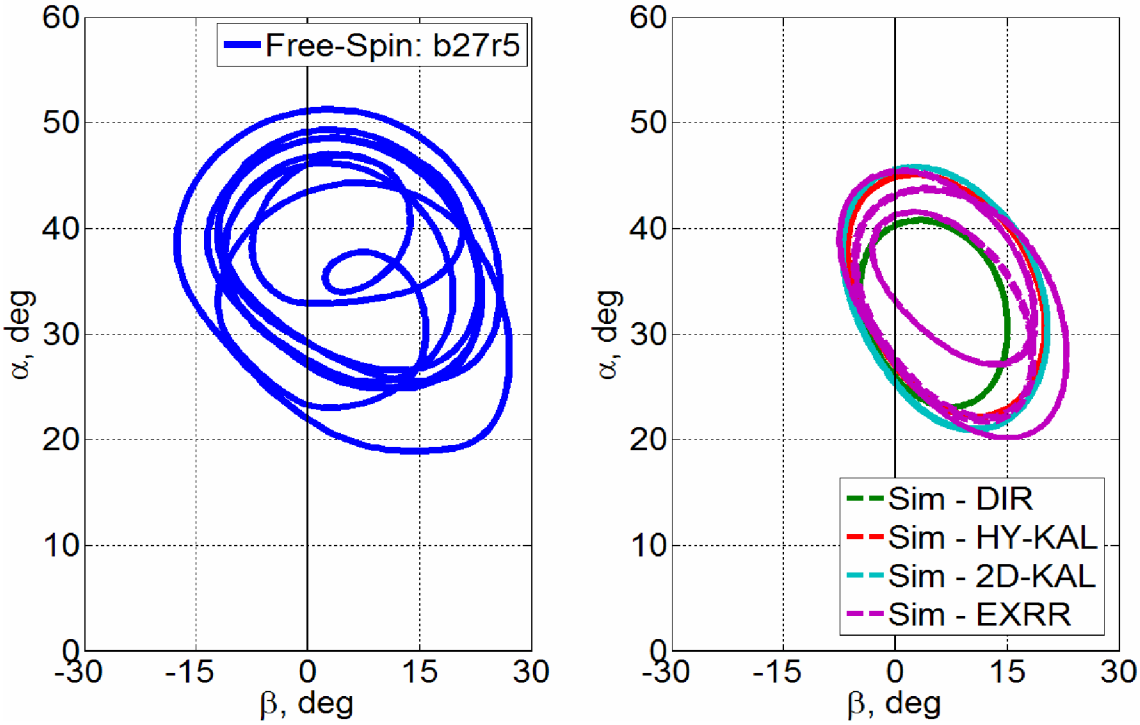

Figure 4.59: Angle of attack – sideslip angle trace from free-spin run b27r5 and simulation results.

It is apparent in Figure 4.59 that the simulation results (using Direct Resolution in particular) are not as oscillatory as the free-spin data. This is not unexpected since the free-spin test conditions are rarely ideal, unlike the simulation. This difference is exacerbated by the fact that the oscillatory spin mode is not a steady-state stable equilibrium but rather an unsteady limit-cycle oscillation. However, the simulation captures the overall character of the spin motion. The next section presents more quantitative comparisons of the simulation results to the free-spin data by examining the spin mode characteristics.

4.3.2 Spin Mode Comparison

The typical flight-test description of a spin includes the orientation (upright or inverted), attitude (steep or flat), degree of oscillation, and rate. In this research, the

character of the spin mode was quantitatively described using the average angle of attack, sideslip angle, nondimensional spin rate, seconds per turn, and velocity. In addition, the RMS deviation about the mean of each parameter was calculated to measure the degree of oscillation of the spin.

Based on simulation studies and rotary balance data analysis, two primary spin modes were expected for the aircraft configuration tested; a steep oscillatory spin mode and a very steep nonoscillatory spin mode. As was shown in Table 4.1, only the oscillatory spin mode was obtained in the free-spin test. This represents the one major difference between the free-spin results and the simulation predictions. When the ailerons are fully deflected with the direction of the spin (runs b32r2, b33r4, b42r7, and b42r9), the simulation predicts a very steep, nonoscillatory spin mode, but the free-spin test results exhibited a steep, oscillatory spin mode. However, as mentioned in Section 3.5.4, difficulty in obtaining extremely steep spin modes is a known limitation of the free-spin test technique. Consequently, the comparisons in this section will be limited to the oscillatory spin mode results.

Figure 4.60 through Figure 4.64 show comparisons of spin mode characteristics for the oscillatory spins obtained in the free-spin test and simulation results using the blending methods described in Section 2.3.2, with the exception of using rotary balance data only. This method is not suitable for simulation of general aircraft motion and will often drive the simulation unstable. It should be noted that simulation results using forced oscillation data only did not predict a spin for runs b27r5 and b27r9 and are omitted.

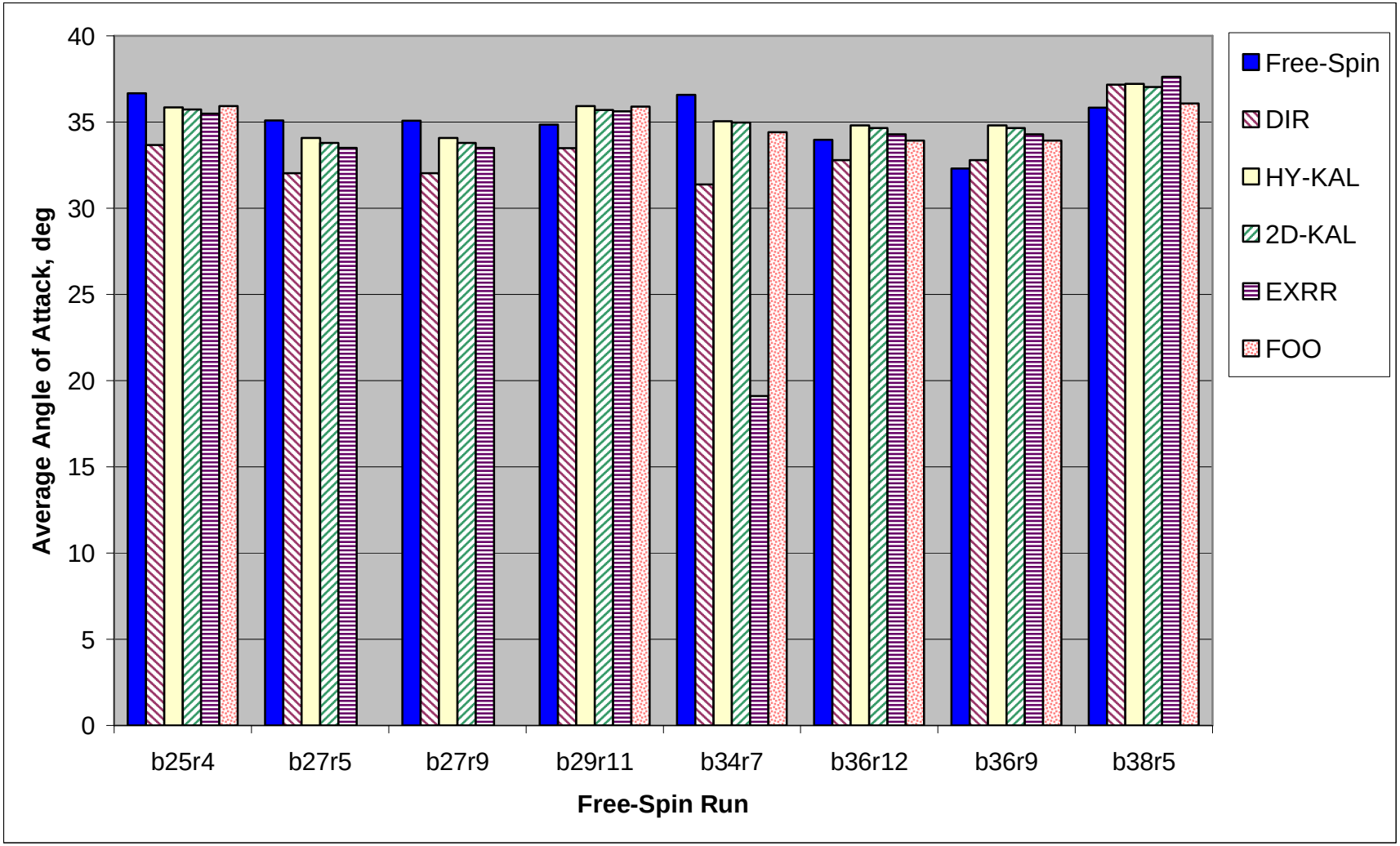

Figure 4.60: Comparison of average angle of attack for oscillatory spin modes between free-spin data and simulation results.

As can be seen in Figure 4.60, the average angle of attack from the simulation results agrees fairly consistently with the free-spin data, generally within about 2°. One exception is run b34r7, where the Excess Roll Rate method, and to a lesser extent, the Direct Resolution method have significantly lower average angles of attack. For this run the simulation using the Excess Roll Rate method reached the very steep nonoscillatory spin mode, hence the low average angle of attack.

The next two figures show the average sideslip angle (Figure 4.61) and nondimensional spin rate (Figure 4.62). In general for the sideslip angle, the simulation results agree with the free-spin data within about 2°. The Kalviste methods appear to have the closest match to the free-spin data. Again, for run b34r7, a different spin mode was reached with the simulation using the Excess Roll Rate method, and as a result the average sideslip angle is much different than the other results.

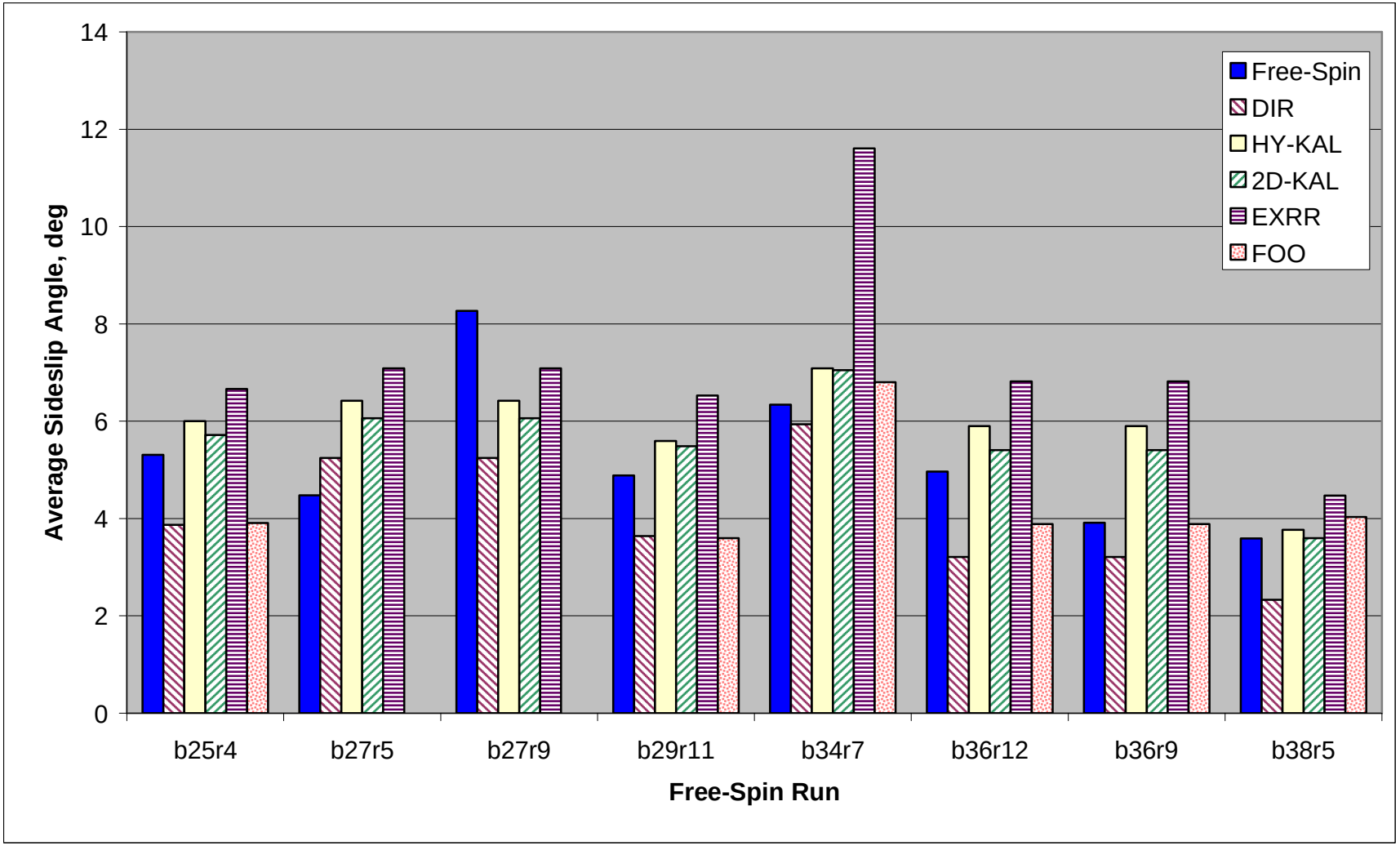

Figure 4.61: Comparison of average sideslip angle for oscillatory spin modes between free-spin data and simulation results.

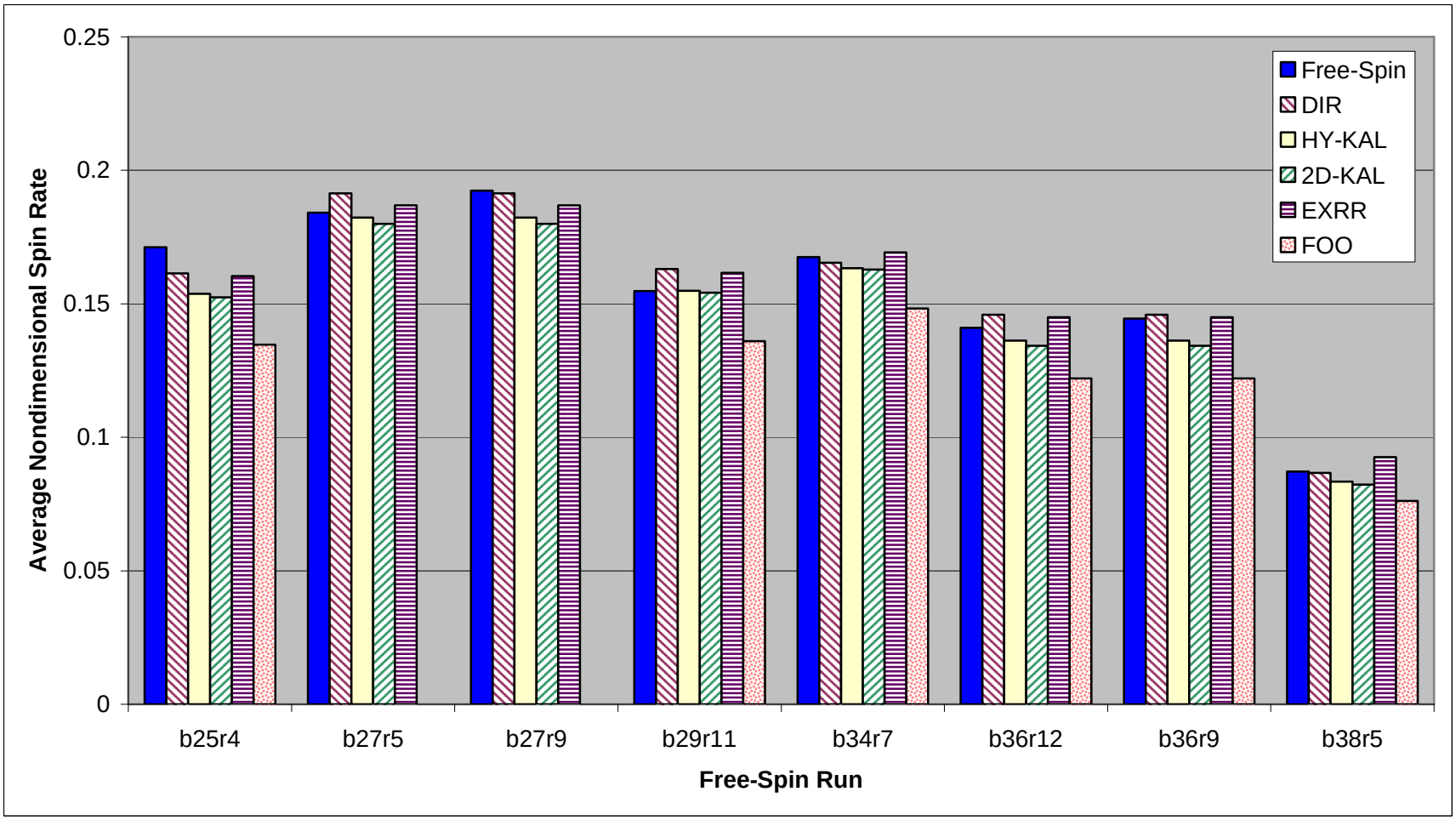

Figure 4.62: Comparison of average nondimensional spin rate for oscillatory spin modes between free-spin data and simulation results.

All of the simulation results for nondimensional spin rate shown in the previous figure match the free-spin data quite well, typically within ~5%. Results using forced oscillation data only typically had the poorest match, while results using the Direct Resolution method had the closest match.

Figure 4.63 shows the average seconds per turn. Again, the simulation results in general show a good match to the free-spin data, but for this parameter, the Kalviste methods provide the closest overall match, with an average within ~7% of the free-spin results.

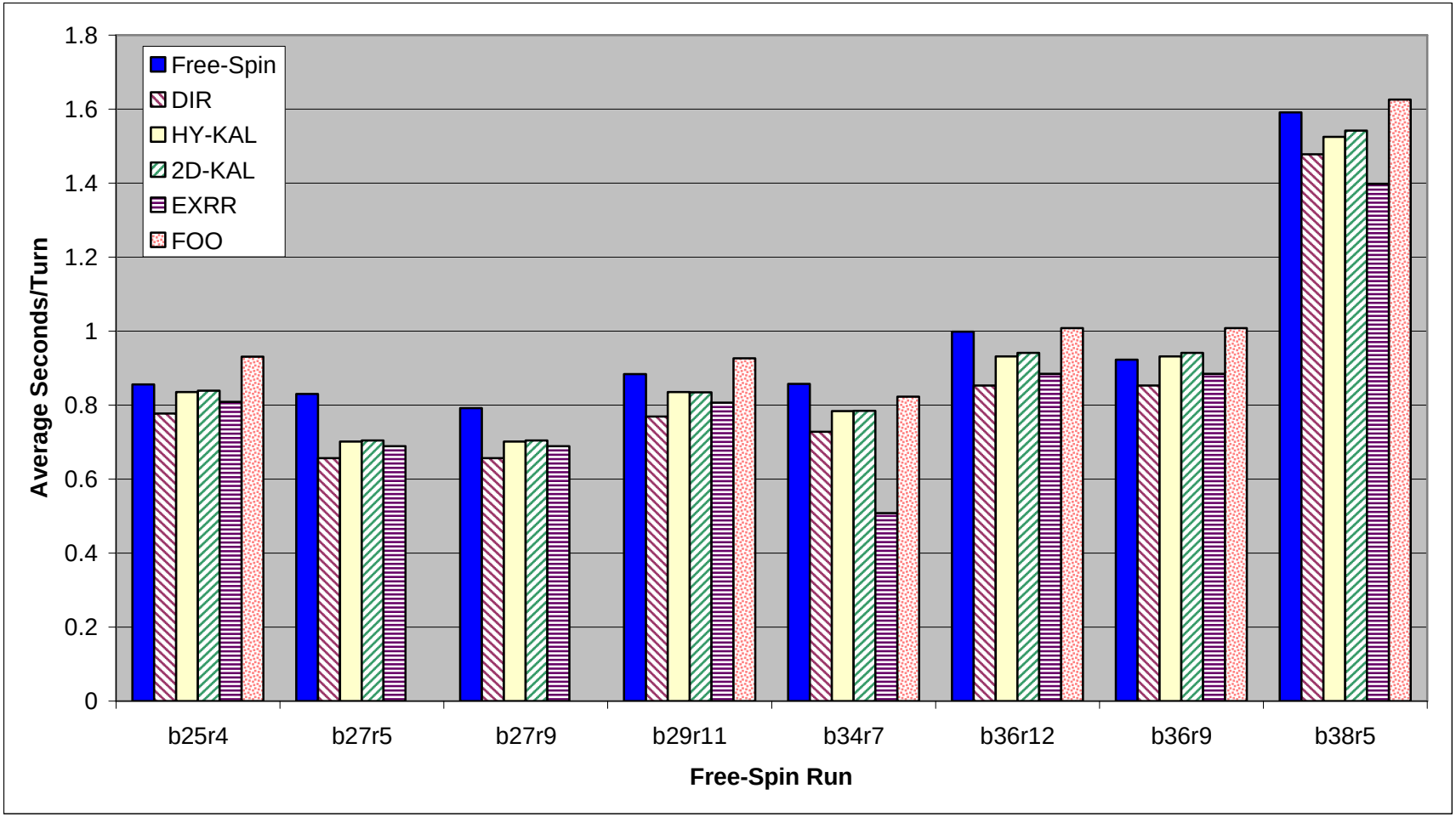

Figure 4.63: Comparison of average seconds per turn for oscillatory spin modes between free-spin data and simulation results.

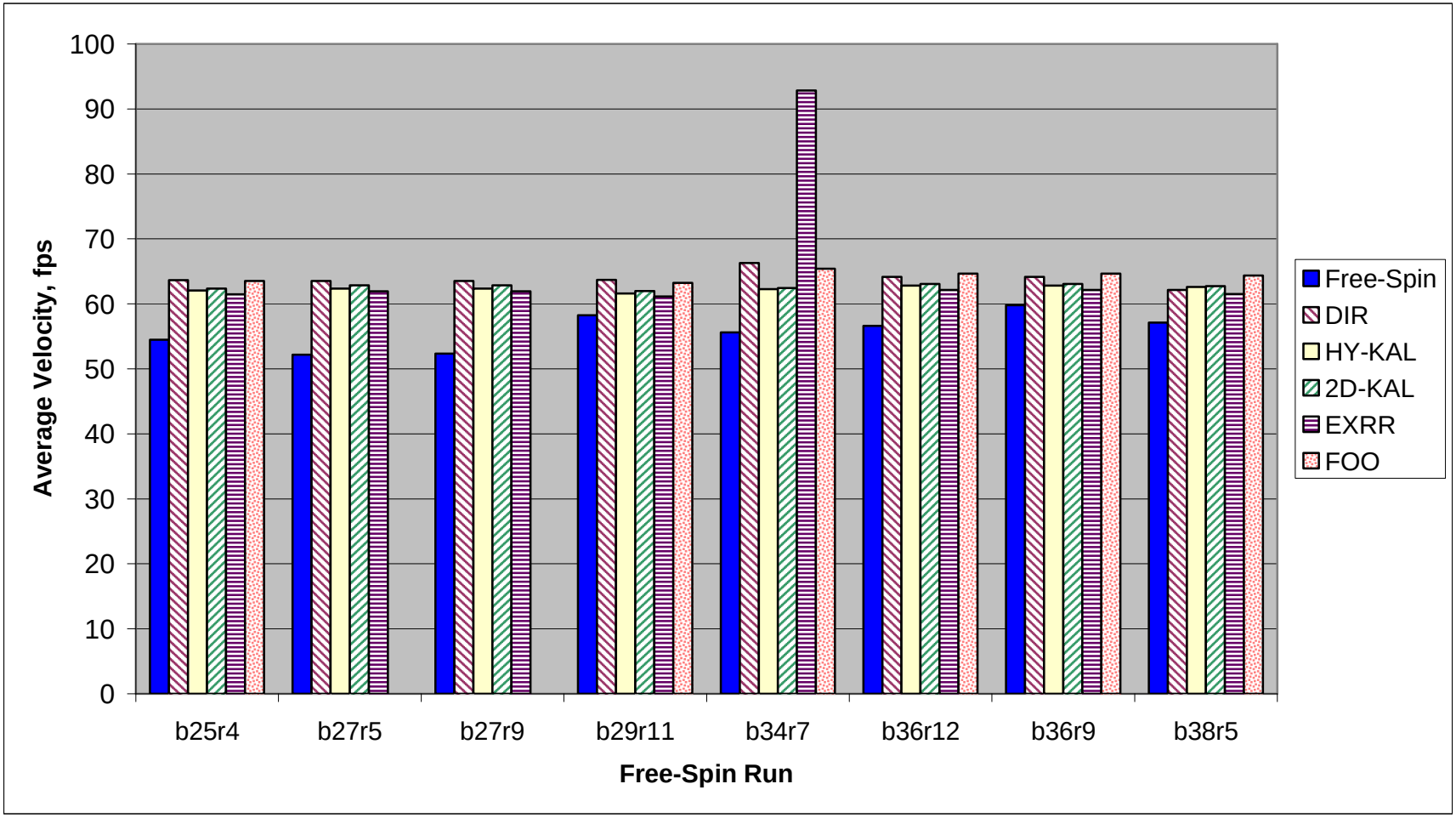

Figure 4.64: Comparison of average velocity for oscillatory spin modes between free-spin data and simulation results.

The final figure in this series shown above (Figure 4.64) depicts the average velocity. In general the simulation results show a higher average velocity and are fairly consistent between blending methods. The one exception is for simulation results using the Excess Roll Rate method for run b34r7 where the simulation obtained a much steeper spin mode and thus has a higher corresponding velocity. The higher average velocity seen in the simulation results agrees with the aerodynamic drag coefficient matching results from Section 4.2.6. The results in that section showed that the aerodynamic model predicted slightly less drag than seen in the free-spin data; a lower drag coefficient corresponds to a higher equilibrium velocity in the spin.

While the average values of the spin mode characteristic are an important metric, since the spins are oscillatory, the degree of oscillation must also be considered. However, a standardized method for quantifying the oscillatory characteristics of a spin does not exist. For this research, the RMS deviation about the mean of each parameter was used to quantify the oscillatory character of the spin.

The following set of figures (Figure 4.65 - Figure 4.69) compares the RMS deviations computed from free-spin data and from simulation results. The simulation results were varied and did not match the free-spin data as well as the average values shown previously. Note that simulation results using forced oscillation data only were typically the worst match and the Kalviste methods generally provided the best results.

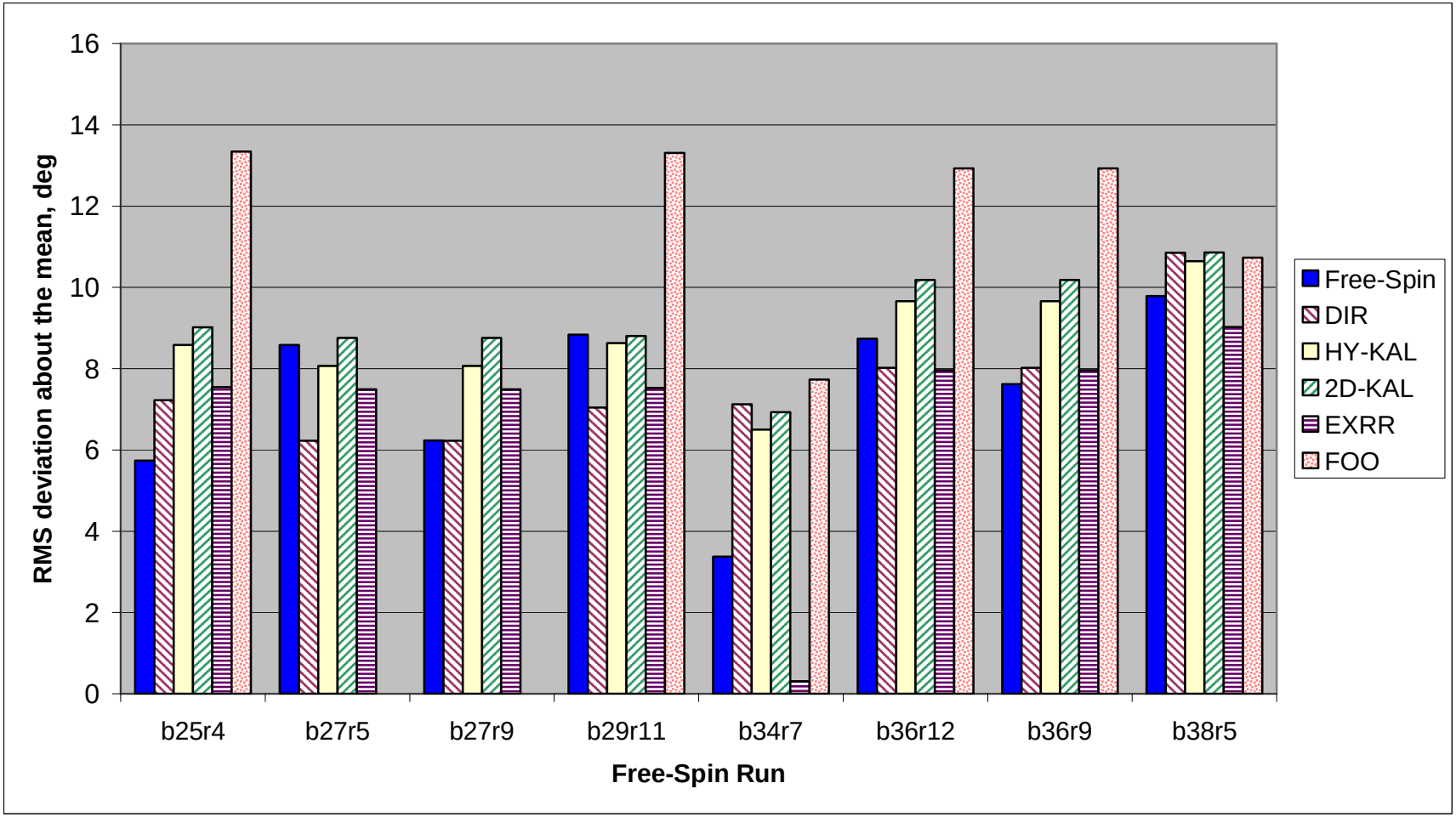

Figure 4.65: Comparison of RMS deviation about the mean of angle of attack for oscillatory spin modes between free-spin data and simulation results.

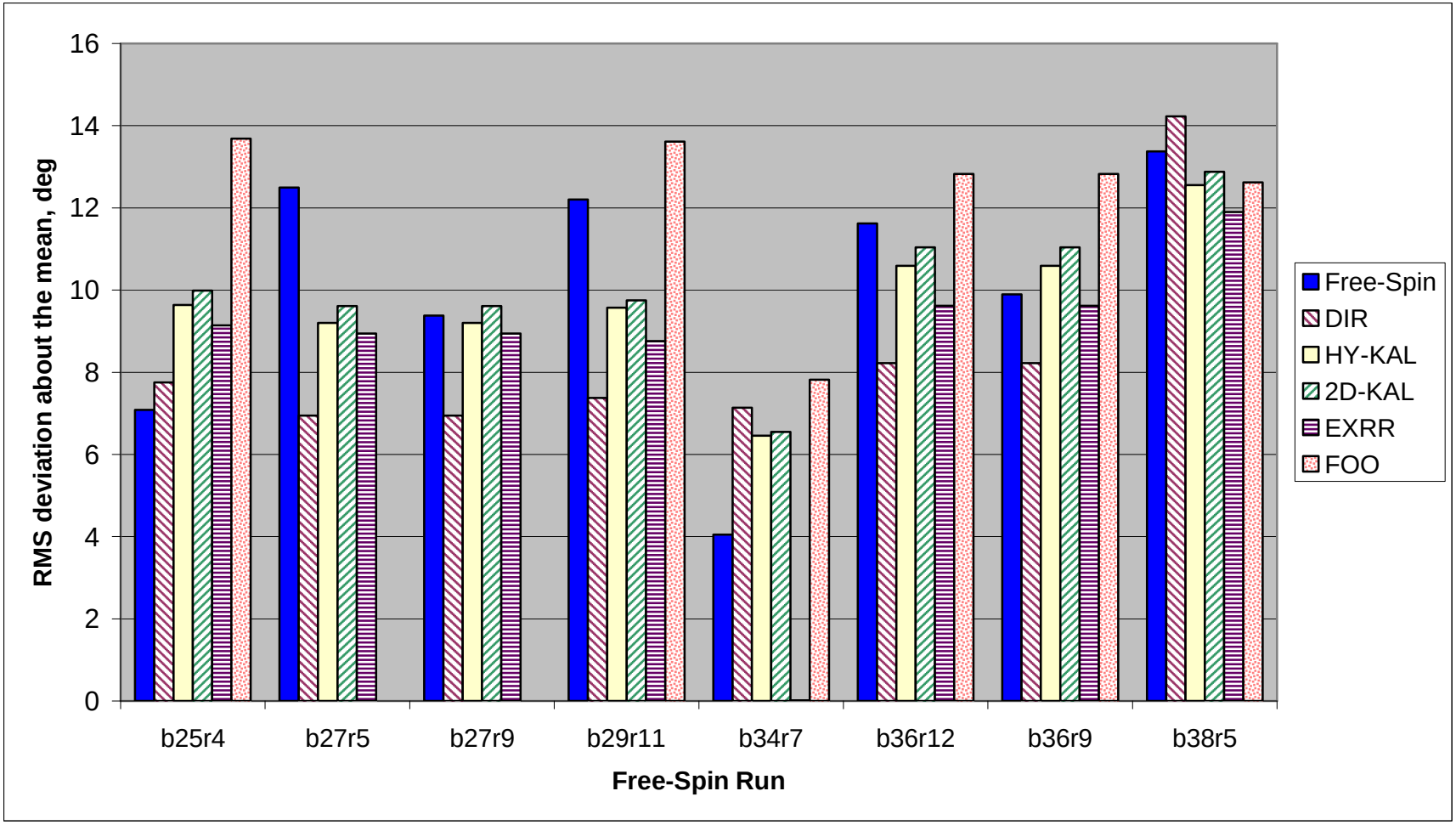

Figure 4.66: Comparison of RMS deviation about the mean of sideslip angle for oscillatory spin modes between free-spin data and simulation results

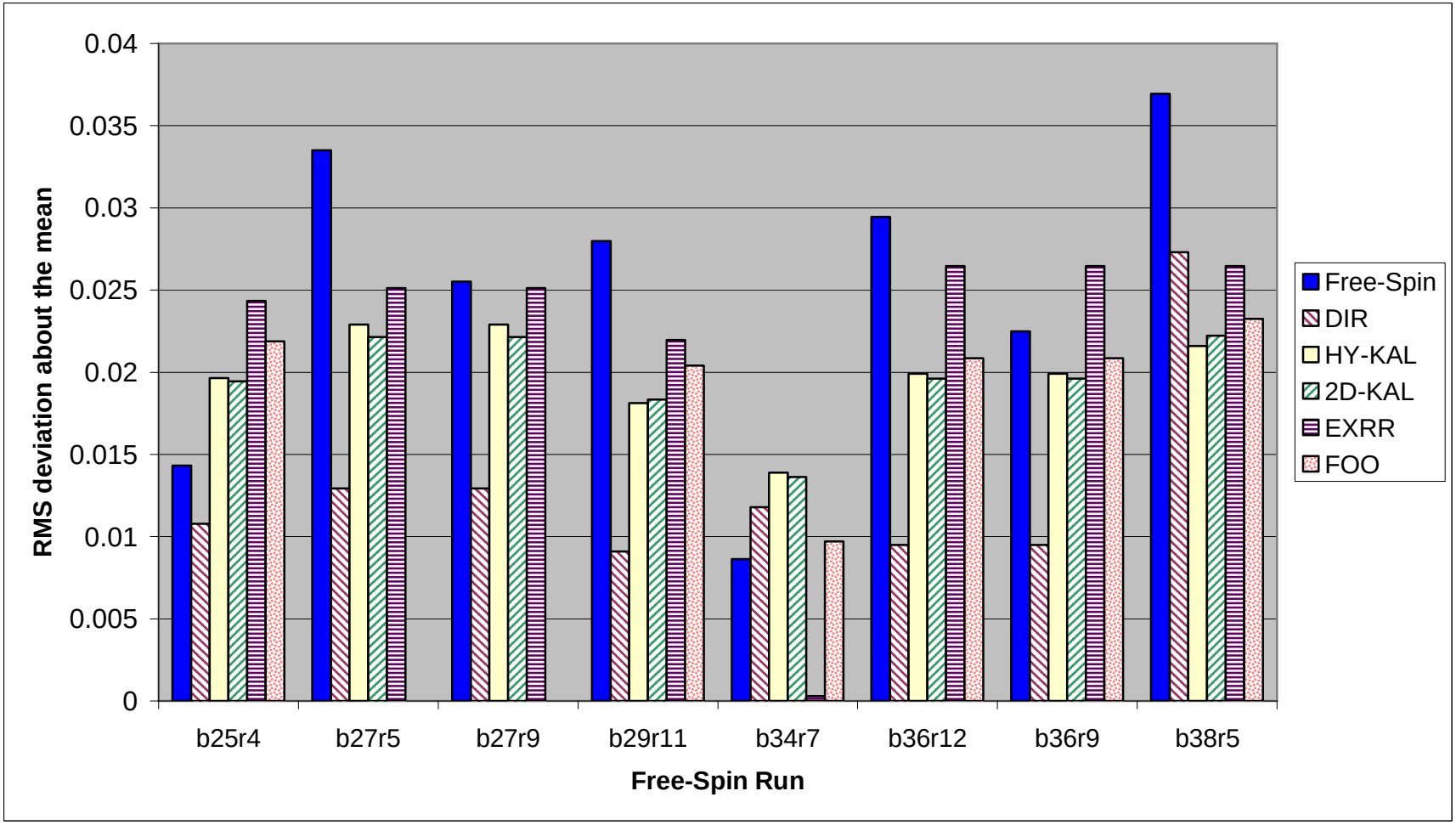

Figure 4.67: Comparison of RMS deviation about the mean of nondimensional spin rate for oscillatory spin modes between free-spin data and simulation results.

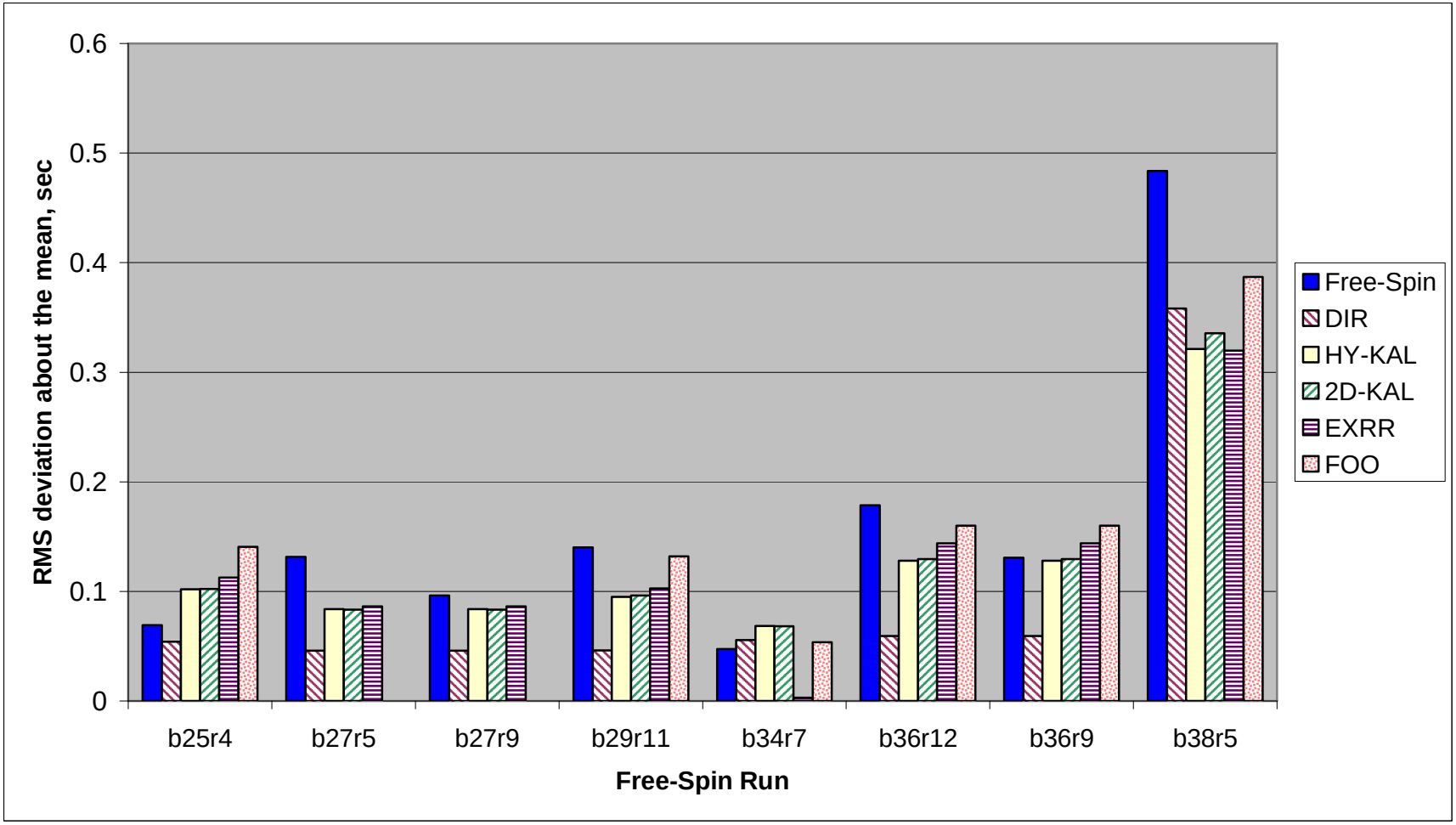

Figure 4.68: Comparison of RMS deviation about the mean of seconds per turn for oscillatory spin modes between free-spin data and simulation results.

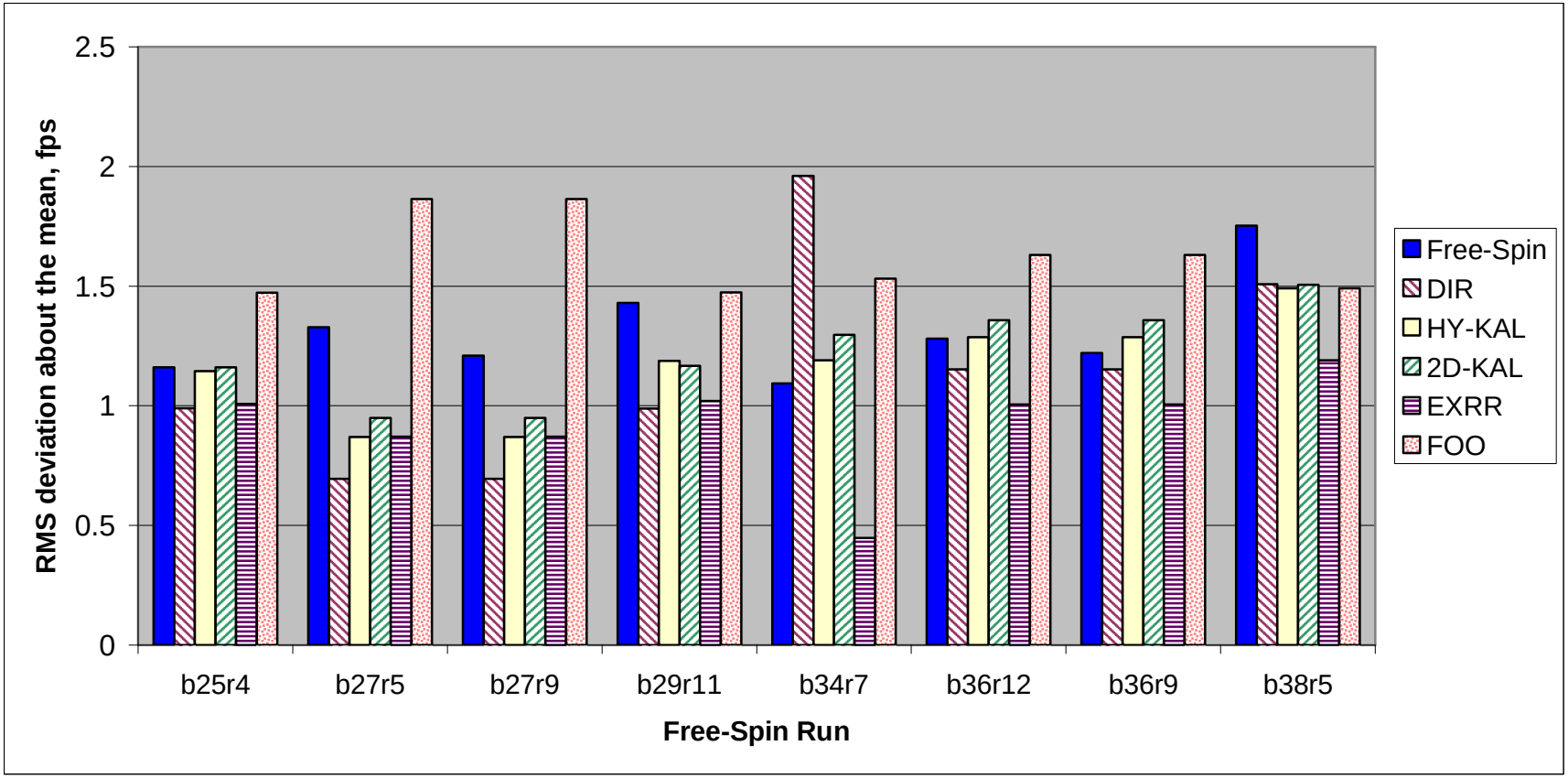

Figure 4.69: Comparison of RMS deviation about the mean of velocity for oscillatory spin modes between free-spin data and simulation results.

Additional insight on the match of the simulation results to the free-spin data can be gained by examining the mean percent error of the simulation results relative to the free-spin data. First, the percent error (relative to the free-spin data) of the simulation results for each of the free-spin runs shown in Figure 4.60 through Figure 4.64 was computed. The mean percent error was then calculated by averaging these values. Figure 4.70 shows the mean percent error for each averaged spin mode characteristic shown in Figure 4.60 through Figure 4.64. It should be noted that mean percent error of the sideslip angle is inflated due to the low magnitude of the average sideslip angles. As mentioned previously, the simulation results for both the average angle of attack and average sideslip angle were within ~2° of the average values for the free-spin data.

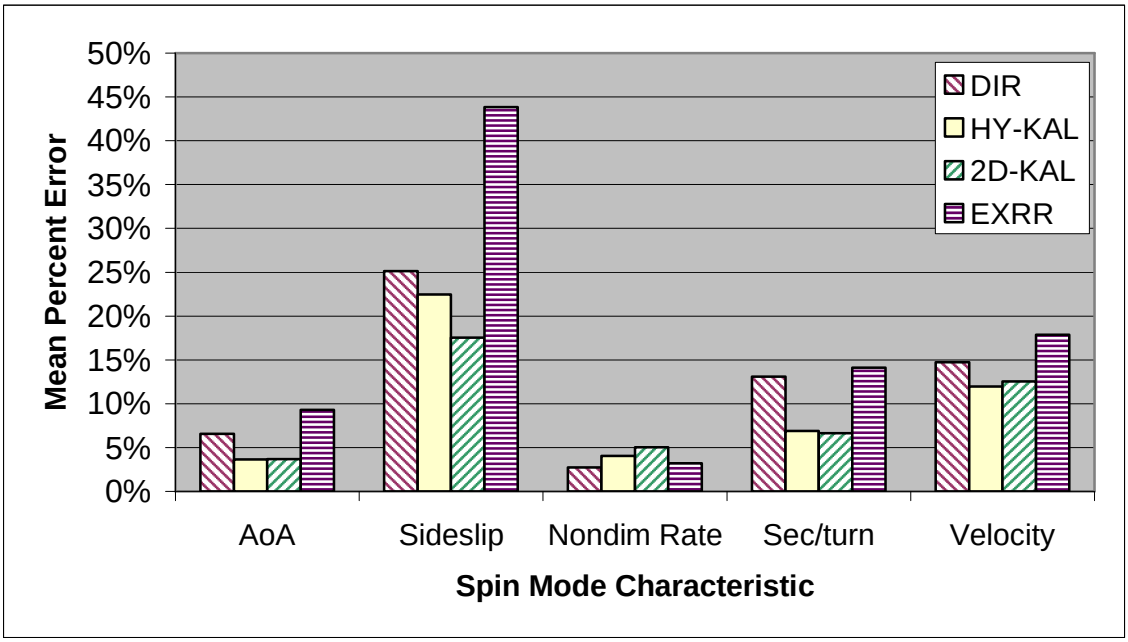

Figure 4.70: Mean percent error of simulation results for averaged spin mode characteristics.

The results in Figure 4.70 show the Kalviste methods generally have lowest mean percent error, with the exception of the nondimensional spin rate. The average spin characteristics matched best were the nondimensional spin rate (all within 5%) and the angle of attack (all within 10%), arguably the most important features that describe a spin.

Figure 4.71 shows the mean percent error of the simulation results relative to the free-spin data for the RMS deviations of each spin mode characteristic shown in Figure 4.65 through Figure 4.69. The mean percent errors were calculated via the same method described previously.

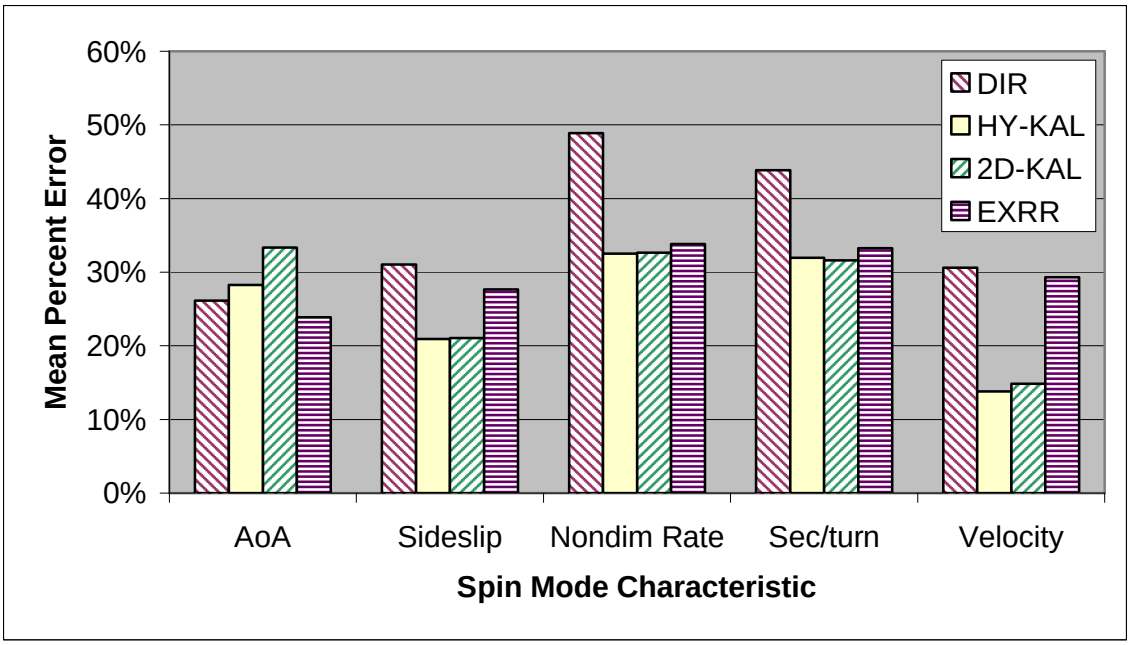

Figure 4.71: Mean percent error of simulation results for the RMS deviation about the mean of spin mode characteristics.

As noted previously, the RMS deviations of the simulation results does not match the free-spin data as well as the averaged values, meaning the simulation results are

generally not as oscillatory as the free-spin data. However, it should be noted that the percent errors for the RMS deviations are larger partially due to the lower magnitude of these values. Again, results using the Kalviste methods generally had the lowest mean percent error, with the exception of the angle of attack, where the Excess Roll Rate method had the lowest mean percent error.

In summary for this section, simulation results using any of the blending methods yielded spin mode characteristics that were similar to the free-spin test results. Average values and RMS deviations about the mean of spin mode characteristics from simulation results using the Kalviste methods had the overall closet match to the free-spin data.

An important exception is the configuration where the simulation predicted a very steep nonoscillatory spin mode (ailerons with the spin) but an oscillatory spin mode was obtained in the free-spin test. As previously discussed, this mismatch is essentially due to limitations of the free-spin test technique and should not be considered a failing of the aerodynamic modeling methods. Nevertheless, a developed spin mode was obtained in the free-spin test that could not be repeated in the simulation. There are a number of possible causes, including potential unmodeled effects of rate on aileron control power, Reynold's number effects on control power, and inaccuracies and/or movement of the ailerons on the free-spin model. A brief sensitivity study was conducted using the simulation and found that a reduction of the aileron deflection from 20° (full deflection, with the spin) to 12° (with the spin) caused the aircraft to transition from the very steep nonoscillatory spin mode to the oscillatory spin mode. This study indicated that degradation in the aileron control power and/or lesser aileron deflection could explain why the free-spin test achieved the oscillatory spin mode.

CHAPTER 5

CONCLUSIONS

This research was successful in modeling the aerodynamics of a large transport aircraft during fully developed spins. This is a significant step towards accurate modeling and prediction of flight dynamics of large transport airplanes in loss-of-control situations. A number of significant conclusions were made based on the research results.

1. Spin dynamics of large transport airplanes can be successfully modeled using a blend of forced oscillation and rotary balance wind tunnel data. The results presented in Chapter 4 showed that the aerodynamic modeling methods captured the aerodynamic characteristics of a large transport aircraft during a spin with sufficient accuracy to enable simulation of spins that are consistent with free-spin wind tunnel test data. The results in Chapter 4 also demonstrated that combining the forced oscillation and rotary balance data yields superior results compared to using only one type of dynamic wind tunnel data.
2. The aerodynamic coefficient matching presented in Section 4.2 showed that the Direct Resolution and Hybrid Kalviste methods had a close match to the free-spin data. The simulation results presented in Section 4.3 demonstrated that using the Hybrid Kalviste and 2D Kalviste methods in simulation resulted in a close match to the free-spin data. These results

indicated that using the Hybrid Kalviste method will result in a good overall match to the free-spin data.

3. High-frequency dynamics observed in the output of the aerodynamic model were determined to be a result of the blending methods, nonlinearities in the forced oscillation data, and propagation of asymmetries in the rotary balance data through the data reduction process.

   The fundamental issue concerning the blending methods is that the oscillatory rate database is referenced using angular rates not representative of the actual body-axis angular rates the aircraft is experiencing. This fact, coupled with significant nonlinearities in the roll and yaw forced oscillation databases, results in high-frequency dynamics in the rolling and yawing moment coefficients. A new lookup method that mitigates this issue is proposed in Chapter 6.

   In addition, asymmetries in the static rotary balance rolling and yawing moment coefficients were propagated to the rotary balance database via the data reduction process. As a result, the rolling and yawing moment coefficient increments due to rate contain large nonlinearities near $\beta = 0^-$ that may not be representative of the true aerodynamics. Further research on how to deal with aerodynamic asymmetries is needed, as discussed in Chapter 6.

4. The forced oscillation database did not contain sufficiently high enough values of nondimensional rate for modeling spins. The nondimensional roll and yaw rates reached during the free-spin test were significantly larger than

the limits of the corresponding forced oscillation databases. As a result, extrapolation was required when using only forced oscillation data in the aerodynamic model. Linearly extrapolating outside of the database can produce misleading results since the roll and yaw forced oscillation data contains significant nonlinearities.

In addition, the oscillatory pitch rate calculated by the blending methods at times slightly exceeded the corresponding forced oscillation database. While extrapolation outside of the forced oscillation databases can produce misleading results, the pitch forced oscillation data is relatively linear with respect to rate, indicating the extrapolation in the pitch forced oscillation database likely had little negative impact.

Finally, additional data is needed to validate the aerodynamic modeling methods for post-stall gyrations, incipient spin, and spin recovery phases. Only the developed spin phase can be validated using free-spin wind tunnel data. Subscale flight testing using dynamically-scaled powered models has been proposed as a method for obtaining flight-test data from high-risk flight regimes and is under development[25,26].

CHAPTER 6

RECOMMENDATIONS

Several issues requiring further research were identified during the course of this research. This chapter will discuss these needs and recommendations on meeting them.

6.1 New Lookup Method for Blending Methods

As discussed in Section 4.2 and Chapter 5, one cause of the high-frequency dynamics present in the aerodynamic model output was the blending methods. The fundamental issue is the blending methods lookup the forced oscillation data at angular rates not representative of the actual aircraft motion. This approach is acceptable if the forced oscillation data is linear with respect to angular rate (e.g. when using linear derivatives). However, since the forced oscillation data used in this research is highly nonlinear with respect to rate at high angles of attack, high-frequency dynamics are introduced to the aerodynamic model output that were not observed in the free-spin wind tunnel data.

In an effort to more accurately represent the actual aircraft motion, a new method for looking up the forced oscillation data was developed and tested that uses forced oscillation data at an angular rate more representative of the actual aircraft motion. The new method was inspired by Kramer's proposed method[13], which looks up the forced oscillation and rotary balance data at the total angular rate ($\bar{\Omega}$) and then multiplies the resulting coefficient increment by a scale factor proportional to the oscillatory or steady-state rate component.

All of the blending methods compute a steady-state angular rate that represents the portion of the total angular rate that is assigned to the rotary balance data and oscillatory rate components that represent the portion of the total angular rate that is assigned to the forced oscillation data (ref Section 2.3.2). The oscillatory components are computed by subtracting an appropriate portion of the steady-state angular rate from the total body-axis angular rates. For example, the Direct Resolution equations are repeated below.

$$\omega_{ss} = p_b \cos\alpha \cos\beta + q_b \sin\beta + r_b \sin\alpha \cos\beta \tag{6.1}$$

$$p_{osc} = p_b - \omega_{ss} \cos\alpha \cos\beta \tag{6.2}$$

$$q_{osc} = q_b - \omega_{ss} \sin\beta \tag{6.3}$$

$$r_{osc} = r_b - \omega_{ss} \sin\alpha \cos\beta \tag{6.4}$$

This method of computing the oscillatory angular rate components often results in small oscillatory rate values that are not representative of the actual aircraft motion. When these small values are used to lookup forced oscillation data, significant nonlinearities can be introduced to the aerodynamic model output.

The new method of looking up forced oscillation data first finds the coefficient increment using the body-axis angular rate, then finds the coefficient increment due to the steady-state rate component, and finally subtracts this value from the body-axis increment. This is perhaps easier understood in equation form. Using the roll oscillatory component and rolling moment as an example, recall that the Direct Resolution method looks up the rolling moment coefficient increment due to oscillatory roll rate using the following:

$$\Delta C_{l,\hat{p}_{osc}} = C_{l,\hat{p}_{osc}}\left(\alpha, \hat{p}_{osc}\right) \tag{6.5}$$

Where $C_{l,\hat{p}_{osc}}$ represents the forced oscillation database and p_{osc} is computed using Equation (6.2). In contrast, the new method computes the coefficient increment by the following:

$$\Delta C_{l,\hat{p}_{osc}} = C_{l,\hat{p}_{osc}}(\alpha, \hat{p}_b) - C_{l,\hat{p}_{osc}}(\alpha, \hat{\omega}_{ss}\cos\alpha\cos\beta) \tag{6.6}$$

The new method uses the same oscillatory angular rate value, but essentially just shifts where this value is used in the forced oscillation database. Figure 6.1 depicts this process graphically:

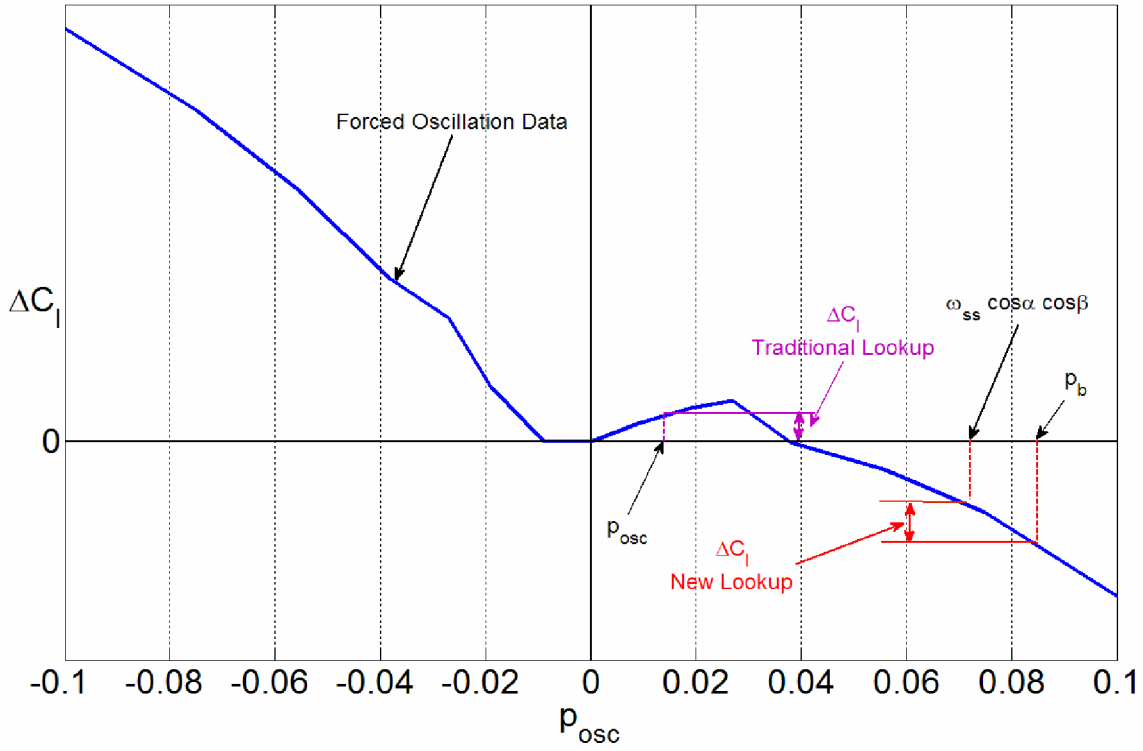

Figure 6.1: Roll forced oscillation rolling moment increment, $\alpha = 35^{\circ}$, showing graphical depiction of traditional (purple) and new (red) lookup methods

In the hypothetical example shown in Figure 6.1, $\hat{p}_b \approx 0.083$, $\hat{\omega}_{ss}\cos\alpha\cos\beta \approx 0.070$, and thus $\hat{p}_{osc} \approx 0.013$. Using the new lookup method (shown in red in Figure 6.1) the

rolling moment increment would be negative, but using the traditional method (shown in purple) the increment would be positive due to the nonlinearity in the forced oscillation data.

When used in conjunction with symmetric rotary balance data (discussed in Section 6.3), using the new lookup method eliminated the majority of high-frequency dynamics previously seen in the aerodynamic model output. The rolling moment coefficient matching results for free-spin data b29r11 and the aerodynamic model using the Direct Resolution method with traditional and new lookups is shown below in Figure 6.2 and Figure 6.3.

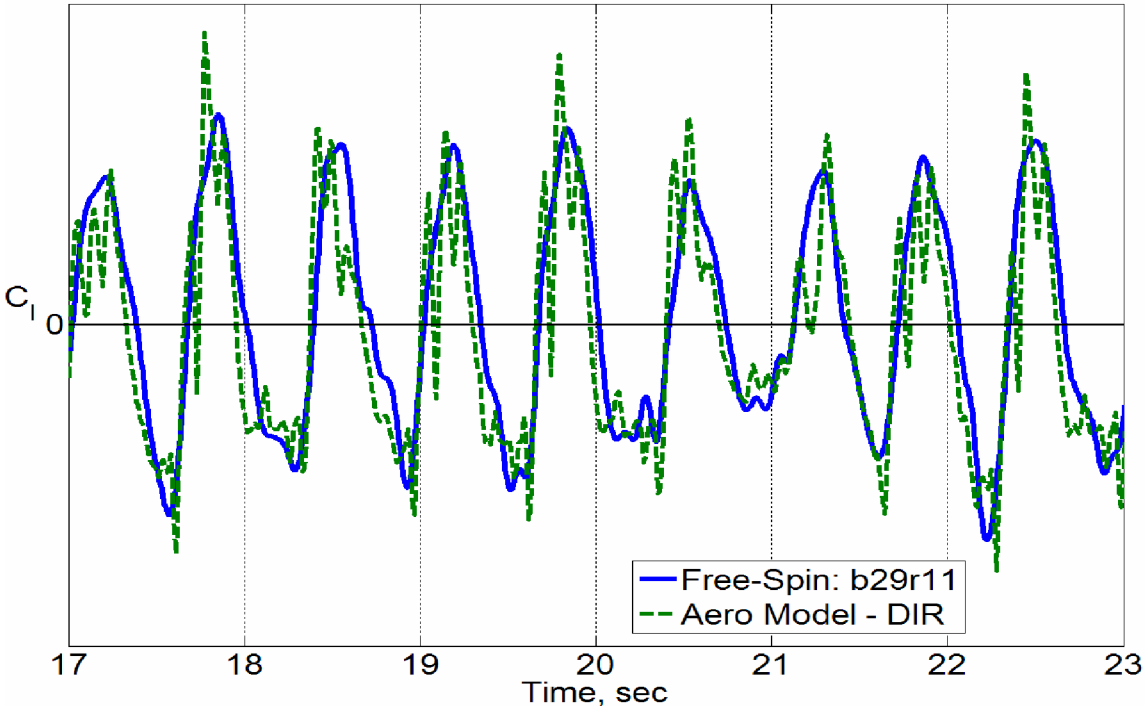

Figure 6.2: Comparison of Rolling Moment Coefficient for free-spin data b29r11 and aerodynamic model using Direct Resolution blending with traditional lookup.

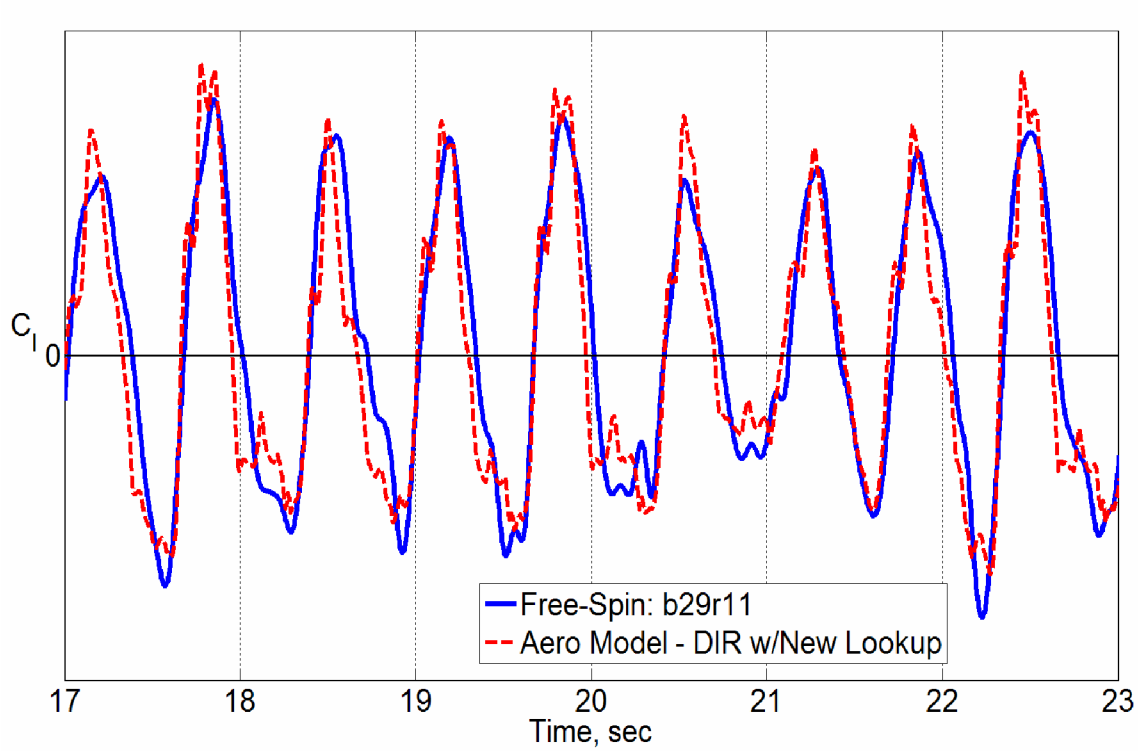

Figure 6.3: Comparison of Rolling Moment Coefficient for free-spin data b29r11 and aerodynamic model using Direct Resolution blending with new lookup and symmetric rotary balance data.

As can be seen in Figure 6.2 and Figure 6.3, the new lookup method used with symmetric rotary balance data significantly reduces or eliminates the high-frequency dynamics in the aerodynamic model output while still producing a good match to the free-spin data.

One disadvantage to the new lookup method is that the forced oscillation data must be looked up at the full body-axis angular rates. As mentioned previously, the nondimensional body-axis rates experienced during a spin often exceeded the forced oscillation database, making extrapolation necessary when using the new lookup method.

The results using the new lookup method show promise and further development of this method with appropriately sized forced oscillation databases should provide significant improvement in the aerodynamic model output.

6.2 Investigate Aerodynamic Asymmetries in Wind Tunnel Data

As has been discussed, the high-frequency dynamics shown in Chapter 4 are due in part to nonlinearities and asymmetries in the aerodynamic databases. An additional concern not specifically mentioned in Chapter 4 is that the forced oscillation databases are not symmetric with respect to angular rate, as is normally expected for a symmetric aircraft.

Aerodynamic asymmetries are present in the forced oscillation and rotary balance databases because the data was processed "as is", i.e., all of the features in the experimental data were assumed to be "real" aerodynamic effects. This brings up the fundamental question that every researcher must confront when analyzing experimental wind tunnel data: What features in the data do you believe to be "real" aerodynamic effects and what features do you consider noise or artificial contamination? Traditionally, this question was answered by assuming the only real aerodynamic effects were those that made sense according to relatively simple aerodynamic models (e.g., $C_l = 0$ when $\beta = 0^-$). Experience has shown that many of the features seen in experimental wind tunnel data are indeed real aerodynamic effects that are not captured by traditional aerodynamic models. However, it has also been recognized that peculiarities in wind tunnel data can be caused by many other factors, including instrumentation errors and noise, model imperfections, sting interactions, structural dynamics, and wind tunnel flow irregularities, to name a few.

Traditional wind tunnel testing is not normally aimed at identifying and modeling aerodynamic asymmetries. A wind tunnel test specifically designed to model aerodynamic asymmetries is one approach to resolving this issue, but it is not clear how

such a test should be designed or if the test would require changes in instrumentation and/or data collection practices. Additional investigation of this matter is recommended.

Research is also recommended to determine if accurate modeling of aerodynamic asymmetries has an appreciable effect on accurate prediction of post-stall and spin motions. An additional concern requiring further research is how to deal with asymmetries when creating aerodynamic models from dynamic wind tunnel data.

6.3 Creation of a Symmetric Rotary Balance Database

In Section 4.2.1, asymmetries in the rotary balance data were identified as an additional source of high-frequency dynamics seen in the aerodynamic model output. Due to the data reduction process, described in Section 4.2.1, asymmetries in the static rotary balance data were propagated to the dynamic data.

One approach to this issue is to make the rotary balance data symmetric before performing the data reduction process. While this approach does not address the larger issue of how to model aerodynamic asymmetries, it does provide a simple solution that prevents static asymmetries from being propagated into the dynamic data.

A symmetric rotary balance database was created by flipping one part of the data across the point of expected symmetry, averaging the data, and flipping the result back. This method was developed during previous NASA/Boeing aerodynamic modeling research[2]. The points of expected symmetry are based on physically similar flow situations. Symmetry is expected about $\beta = 0^-$:

$$\begin{aligned} C_l\left(-\hat{\omega}_{ss}\right) &= -C_l\left(+\hat{\omega}_{ss}\right) \quad & C_X\left(-\hat{\omega}_{ss}\right) &= C_X\left(+\hat{\omega}_{ss}\right) \\ C_m\left(-\hat{\omega}_{ss}\right) &= C_m\left(+\hat{\omega}_{ss}\right) \quad & C_Y\left(-\hat{\omega}_{ss}\right) &= -C_Y\left(+\hat{\omega}_{ss}\right) \\ C_n\left(-\hat{\omega}_{ss}\right) &= -C_n\left(+\hat{\omega}_{ss}\right) \quad & C_Z\left(-\hat{\omega}_{ss}\right) &= C_Z\left(+\hat{\omega}_{ss}\right) \end{aligned} \tag{6.7}$$

Symmetry is also expected for the following cases of non-zero sideslip:

$$\begin{aligned} C_l(-\hat{\omega}_{ss},-\beta) &= -C_l(+\hat{\omega}_{ss},+\beta) & C_X(-\hat{\omega}_{ss},-\beta) &= C_X(+\hat{\omega}_{ss},+\beta) \\ C_m(-\hat{\omega}_{ss},-\beta) &= C_m(+\hat{\omega}_{ss},+\beta) & C_Y(-\hat{\omega}_{ss},-\beta) &= -C_Y(+\hat{\omega}_{ss},+\beta) \\ C_n(-\hat{\omega}_{ss},-\beta) &= -C_n(+\hat{\omega}_{ss},+\beta) & C_Z(-\hat{\omega}_{ss},-\beta) &= C_Z(+\hat{\omega}_{ss},+\beta) \end{aligned} \tag{6.8}$$

The process to make the data symmetric is depicted graphically in Figure 6.4 and Figure 6.5.

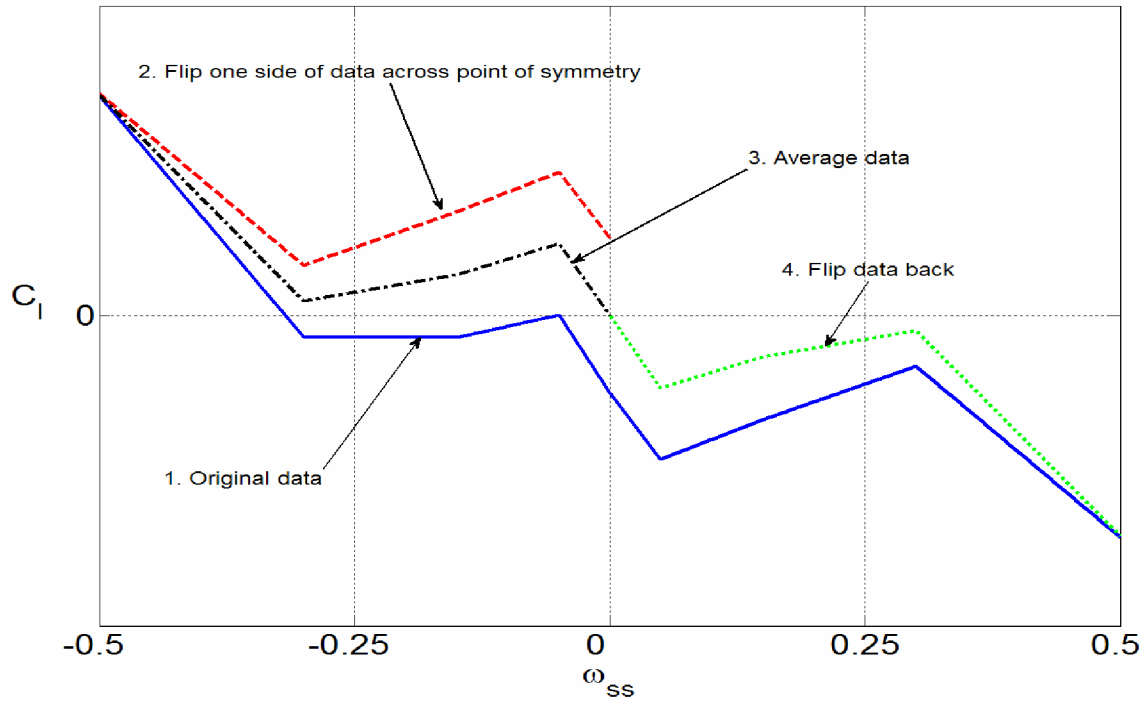

Figure 6.4: Graphical depiction of method used to make rotary balance rolling moment coefficient data symmetric, $\alpha = 30^{\circ}$ and $\beta = 0^{\circ}$.

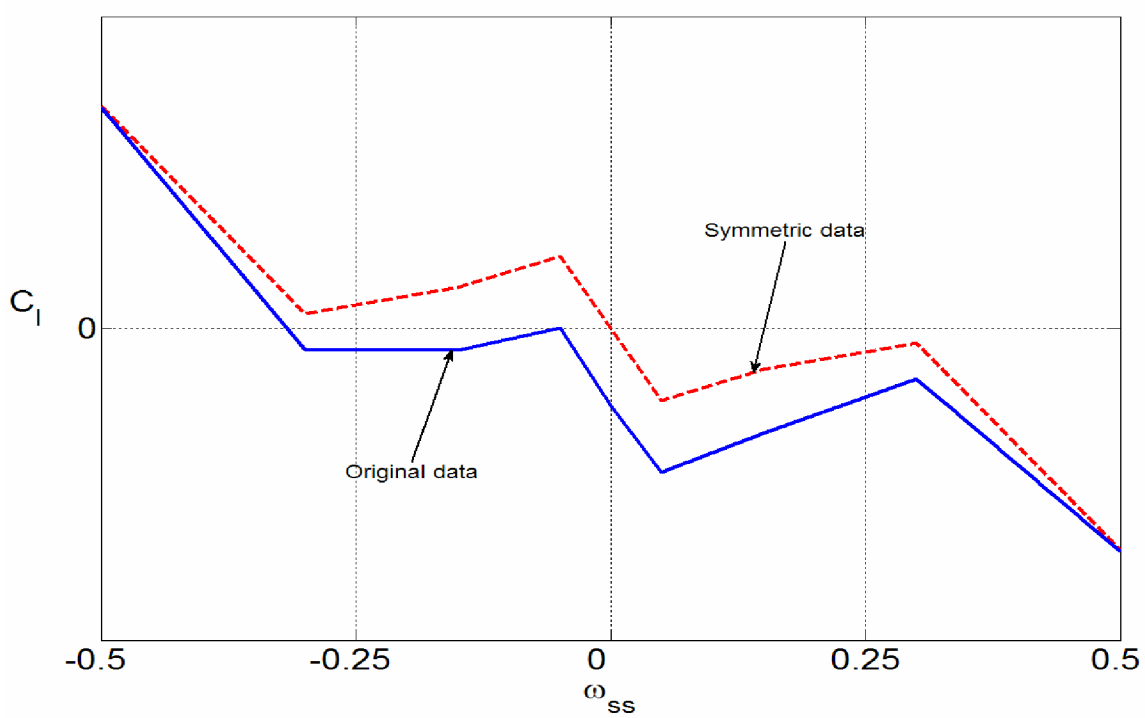

Figure 6.5: Original and symmetric rotary balance rolling moment coefficient data, $\alpha = 30^{-}$ and $\beta = 0^{-}$.

As can be seen in Figure 6.4 and Figure 6.5, this method of making data symmetric provides the desired result of eliminating the static asymmetry in the data. However, in the process the remainder of the data is significantly altered and it is not clear if this is appropriate. Further research on how to model aerodynamic asymmetries is needed, in particular investigation of whether asymmetries present in static data are present in dynamic data as well.

6.4 High-Rate Forced Oscillation Data

As mentioned in Chapters 4 & 5, the forced oscillation database did not contain sufficiently high enough values of nondimensional rate for modeling spins. This presented a problem for using forced oscillation data only, as the nondimensional roll and yaw rates observed in the free-spin wind tunnel test often significantly exceeded the

limits of the forced oscillation databases. In addition, the pitch oscillatory component computed by the blending methods occasionally extended beyond the database limits. Finally, the new lookup method proposed in Section 6.1 requires forced oscillation data at and above the body-axis nondimensional rates observed in the free-spin test.

Ideally, the forced oscillation database would have sufficient nondimensional rate coverage to include the maximum rates observed during the free-spin test or the maximum oscillatory rate components computed using the new lookup method, whichever is greater. This would allow the new lookup method described in Section 6.1 to be fully tested. The required database limits computed using this criterion are shown in Table 6.1.

Table 6.1: Suggested nondimensional rates for forced oscillation testing

Axis	Existing Limits	Desired Limits	Desired Resolution	Additional Test Points
Roll	±0.107	±0.22	0.05	3
Pitch	±0.0075	±0.012	0.0015	3
Yaw	±0.112	±0.13	0.02	1

At a minimum, at least one value of the nondimensional rates beyond the existing limits for each axis listed in Table 6.1 should be tested to evaluate the validity of linearly extrapolating beyond the limits of the existing database.

6.5 Investigate Tether Effects on Free-Spin Data

The use of tether during the free-spin test was theorized to be a possible source of error in the matching of the pitching moment and axial force coefficients, as discussed in Chapter 4. A thorough investigation of the effect (if any) of the tether on the free-spin

data would help identify deficiencies in the aerodynamic model and improve accuracy of future free-spin tests.

Perhaps the simplest way to investigate the tether effects is to conduct free-spin tests with and without the tether using the same model. Ideally, the same model used in this research would be used, but any aircraft model that has a similar steep oscillatory spin mode would suffice.

The oscillatory spin mode observed in this research was difficult to obtain during free-spin testing. Launching the model without the tether would almost certainly damage or destroy the model. To obtain developed spin data without the tether, a simple mechanism could be used to remotely release the tether from the model once the oscillatory spin mode has been established.

6.6 Investigate Nonoscillatory Spin Mode

The simulation results showed a nonoscillatory spin mode that was not observed during the free-spin test. As discussed in Section 4.3, this difference was likely due to limitation of the free-spin test technique. Further investigation of potential unmodeled effects of rate or Reynold's number on control power could help determine why the nonoscillatory spin mode was not obtained during free-spin testing. In addition, additional free-spin tests could be conducted aimed at attempting to obtain the nonoscillatory spin mode. Flight testing using dynamically scaled subscale models also presents another option for exploring this spin mode.

APPENDIX A

ADDITIONAL INFORMATION ON WIND TUNNEL TESTS

This appendix gives more detail on the static, forced oscillation, and rotary balance wind tunnel tests and on the data reduction process.

A.1 Static Wind Tunnel Testing

The static wind tunnel data used in this research stems from a test completed in 2001[12]. Multiple configurations and control surface deflections were tested at a large range of angles of attack and sideslip angles. The data was reduced to an incremental coefficient buildup model stored in lookup tables. The table breakpoints for the static data are at the following values:

$$\begin{aligned}\alpha_{\text{Table Breakpoints}} = \big[&-5^{\circ}, 0^{\circ}, 2^{\circ}, 4^{\circ}, 6^{\circ}, 8^{\circ}, 9^{\circ}, 10^{\circ}, 11^{\circ}, 12^{\circ}, 13^{\circ}, 14^{\circ}, 15^{\circ}, 16^{\circ}, 18^{\circ}, 20^{\circ}, 22^{\circ}, 24^{\circ}, \ldots \\ &26^{\circ}, 28^{\circ}, 30^{\circ}, 35^{\circ}, 40^{\circ}, 45^{\circ}, 50^{\circ}, 55^{\circ}, 60^{\circ}, 65^{\circ}, 70^{\circ}, 75^{\circ}, 80^{\circ}, 85^{\circ}\big] \\ \beta_{\text{Table Breakpoints}} = \big[&-45^{\circ}, -40^{\circ}, -35^{\circ}, -30^{\circ}, -25^{\circ}, -20^{\circ}, -15^{\circ}, -12^{\circ}, -10^{\circ}, -8^{\circ}, -6^{\circ}, -4^{\circ}, -2^{\circ} \ldots \\ &0^{\circ}, 2^{\circ}, 4^{\circ}, 6^{\circ}, 8^{\circ}, 10^{\circ}, 12^{\circ}, 15^{\circ}, 20^{\circ}, 25^{\circ}, 30^{\circ}, 35^{\circ}, 40^{\circ}, 45^{\circ}\big]\end{aligned} \tag{A.1}$$

The breakpoints for the control surface deflections relevant to this research are given as follows:

$$\delta_{e,\ \text{Table Breakpoints}} = \left[-30^{\circ}, -20^{\circ}, -10^{\circ}, 0^{\circ}, 10^{\circ}, 20^{\circ}\right] \tag{A.2}$$

$$\delta_{a_L,\ \text{Table Breakpoints}} = \delta_{a_R,\ \text{Table Breakpoints}} = \left[-30^{\circ}, -20^{\circ}, -10^{\circ}, 0^{\circ}, 10^{\circ}, 20^{\circ}, 30^{\circ}\right] \tag{A.3}$$

$$\delta_{r,\ \text{Table Breakpoints}} = \left[-45^{\circ}, -30^{\circ}, -10^{\circ}, 0^{\circ}\right] \tag{A.4}$$

A.2 Forced Oscillation Wind Tunnel Testing

Forced oscillation testing normally consists of moving the model in a sinusoidal fashion independently about each of the roll, pitch, and yaw axes. The angle of attack, and amplitude and frequency of the oscillation are typically independent variables during the test. Additional variables may include sideslip angle, control surface deflections, and aircraft configuration.

Force and moment measurements are taken via a strain-gauge balance while the model is oscillated. Data is typically taken for a number of cycles with the wind on and the wind off. These cycles of data are then filtered using a low pass filter with a cutoff frequency of 4 Hz to remove sting structural dynamics and then averaged to form a single cycle of data. The wind off cycle is then subtracted from the wind on cycle to remove the gravitational and inertial effects.

At this stage, the data from forced oscillation testing can be used in several ways. The most common use is to derive the linear damping derivatives (e.g., C_{l_p}, C_{m_q}). Other methods seek to capture nonlinearities in angle of attack, frequency, amplitude, or nondimensional rate. This research utilized a variation of the single-point method to generate look-up tables of aerodynamic coefficient increments based on angle of attack and nondimensional rate. This process involves selecting only the data points where the model is at the nominal or zero-crossing position, as shown in Figure A.1.

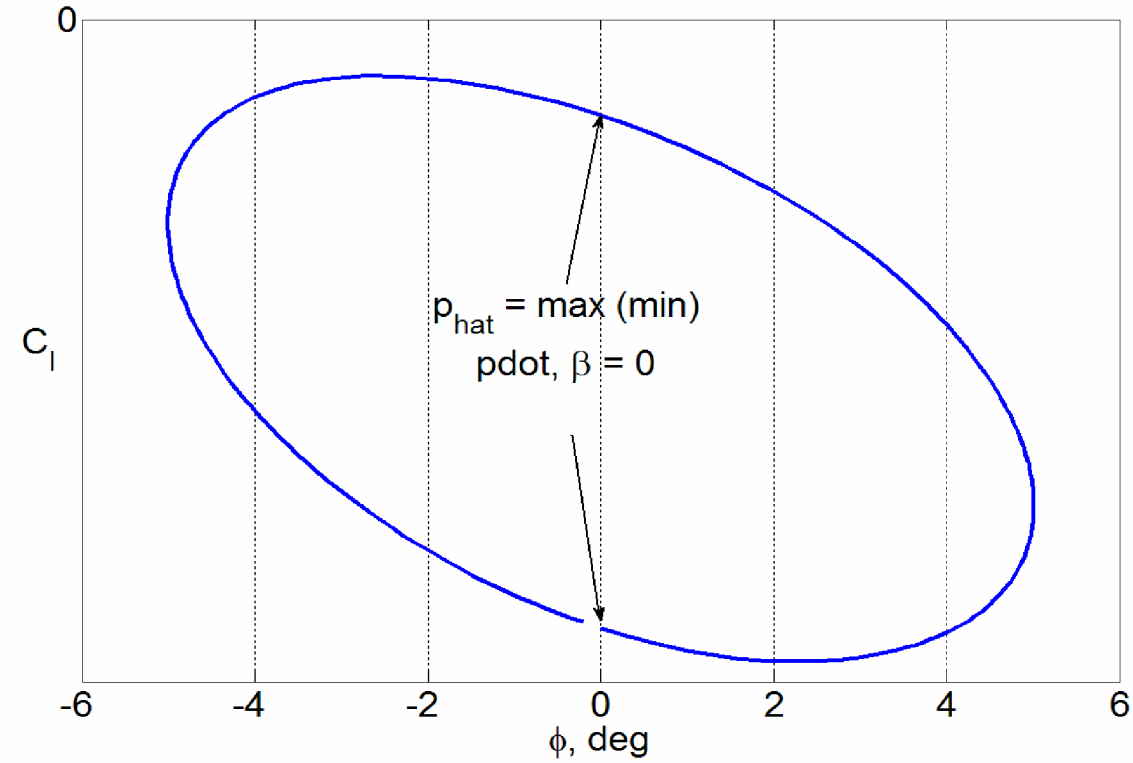

Figure A.1: Rolling moment from roll forced oscillation test, $\alpha = 8^{-}$, denoting zero crossing points where data is selected.

At this point the accelerations are zero, the nondimensional rate is at a maximum, and the angle of attack and sideslip angle are at their nominal values. The goal of this approach is to obtain only the effect of angular rate on the aerodynamic forces and moments.

Forced oscillation tests are normally conducted at a variety of oscillation frequencies and amplitudes. The nondimensional frequency, amplitude, and nondimensional rate are related by the following expression, using nondimensional roll rate as an example:

$$\hat{p} = kA \tag{A.1}$$

where *k* is the nondimensional frequency and *A* is the oscillation amplitude. Some forced oscillation data reduction methods use the frequency and/or amplitude as independent variables (e.g. the integrated method). However, for this research, in which forced oscillation data was combined with steady-rate rotary balance data, a frequency based data reduction method is not compatible with current dynamic data blending methods. For this reason, the forced oscillation data was reduced using nondimensional rate as the primary independent variable.

In addition, the single point method of reducing forced oscillation data is best used with nondimensional rate as the primary independent variable. Figure A.2 shows four forced oscillation data runs, all at the same nondimensional frequency, but at different nondimensional rates.

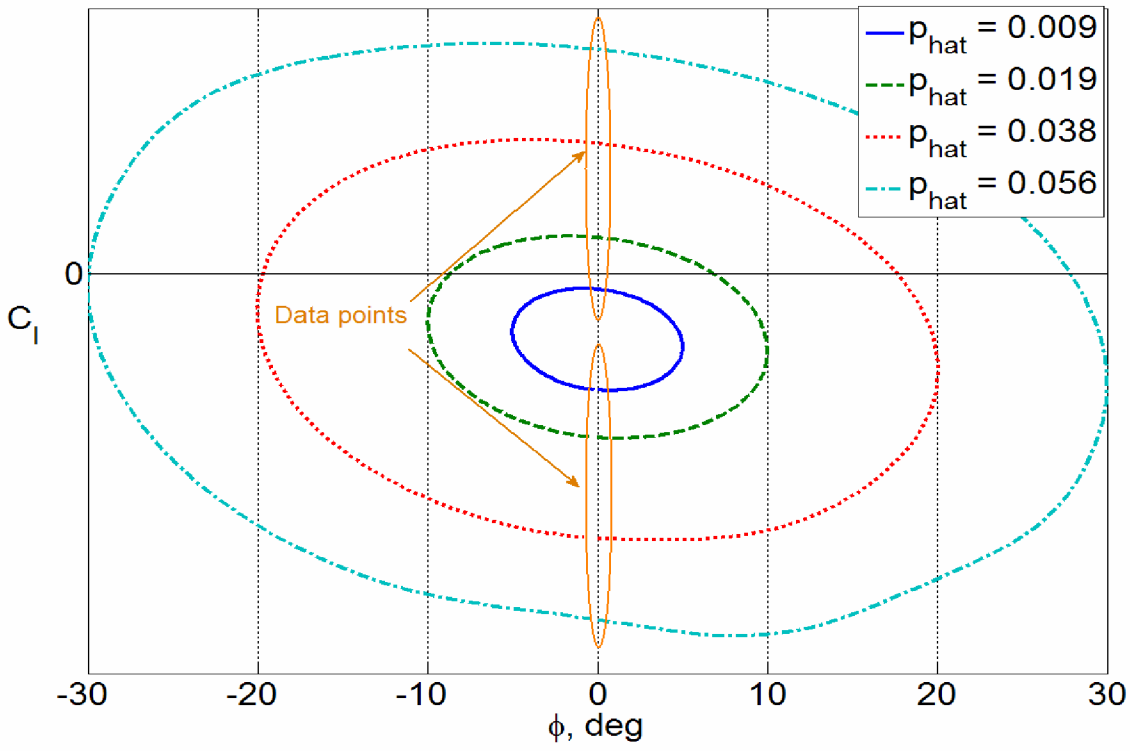

Figure A.2: Rolling moment from roll forced oscillation test, $\alpha = 4^{\circ}$, $k = 0.108$ denoting zero crossing points where data is selected.

The single point method only uses the data points within the orange ellipses. As can be seen, nondimensional rate is a good choice for an independent variable, as there is significant change in the data points with a change in nondimensional rate. In contrast, Figure A.3 shows three forced oscillation data runs, all at the same nondimensional rate, but at differing nondimensional frequencies.

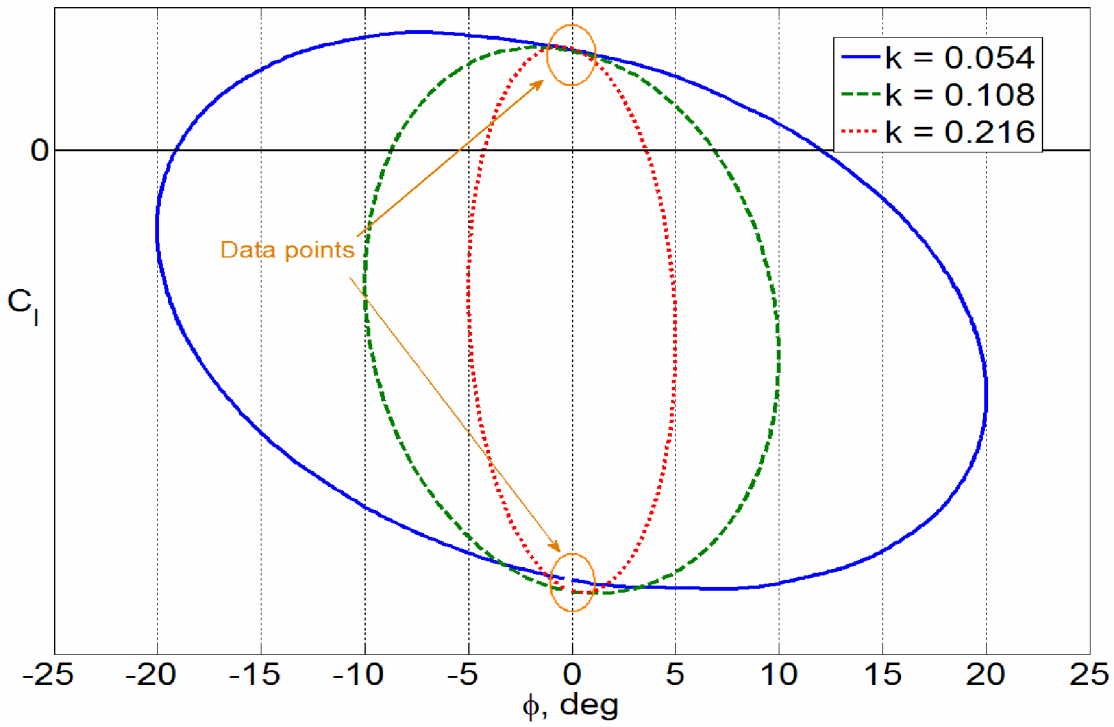

Figure A.3: Rolling moment from roll forced oscillation test, $\alpha = 4^{\circ}$, $\hat{p} = 0.019$ denoting zero crossing points where data is selected.

As can be seen in Figure A.3, using nondimensional frequency as the primary independent variable is not a good choice when using the single point method, as the data points chosen by the single point method, again denoted by the orange circles, would have very little change for different nondimensional frequencies.

The forced oscillation databases used in this research were created as lookup tables of incremental aerodynamic force and moment coefficients. All of the forced oscillation databases were forced through the zero angular rate point, to ensure that there was no coefficient increment at zero angular rate. The breakpoints for each table are given below.

Roll Axis:

$$\begin{aligned}\alpha_{\text{Table Breakpoints}} &= \left[-10^{\circ}, -5^{\circ}, 0^{\circ}, 4^{\circ}, 8^{\circ}, 10^{\circ}, 12^{\circ}, 14^{\circ}, 16^{\circ}, 18^{\circ}, 20^{\circ}, 22^{\circ}, 24^{\circ}, \ldots\right. \\ &\qquad \left. 26^{\circ}, 28^{\circ}, 30^{\circ}, 35^{\circ}, 40^{\circ}, 45^{\circ}, 50^{\circ}, 60^{\circ}, 70^{\circ}, 80^{\circ}, 90^{\circ}\right] \\ \hat{p}_{osc,\ \text{Table Breakpoints}} &= \left[-0.107, -0.075, -0.056, -0.038, -0.027, -0.019, -0.009, \ldots\right. \\ &\qquad \left. 0, 0.009, 0.019, 0.027, 0.038, 0.056, 0.075, 0.107\right]\end{aligned} \tag{A.2}$$

Pitch Axis:

$$\begin{aligned}\alpha_{\text{Table Breakpoints}} &= \left[-30^{\circ}, -25^{\circ}, -20^{\circ}, -15^{\circ}, -10^{\circ}, -5^{\circ}, 0^{\circ}, 4^{\circ}, 8^{\circ}, 10^{\circ}, 12^{\circ}, 14^{\circ}, 16^{\circ}, \ldots\right. \\ &\qquad \left. 18^{\circ}, 20^{\circ}, 22^{\circ}, 24^{\circ}, 26^{\circ}, 28^{\circ}, 30^{\circ}, 35^{\circ}, 40^{\circ}, 45^{\circ}, 50^{\circ}\right] \\ \hat{q}_{osc,\ \text{Table Breakpoints}} &= \left[-0.0075, -0.005, -0.0038, -0.0032, -0.0025, -0.0016, -0.0013, \ldots\right. \\ &\qquad \left. 0, 0.0013, 0.0016, 0.0025, 0.0032, 0.0038, 0.005, 0.0075\right]\end{aligned} \tag{A.3}$$

Yaw Axis:

$$\begin{aligned}\alpha_{\text{Table Breakpoints}} &= \left[-30^{\circ}, -25^{\circ}, -20^{\circ}, -15^{\circ}, -10^{\circ}, -5^{\circ}, 0^{\circ}, 4^{\circ}, 8^{\circ}, 10^{\circ}, 12^{\circ}, 14^{\circ}, 16^{\circ}, \ldots\right. \\ &\qquad \left. 18^{\circ}, 20^{\circ}, 22^{\circ}, 24^{\circ}, 26^{\circ}, 28^{\circ}, 30^{\circ}, 35^{\circ}, 40^{\circ}, 45^{\circ}, 50^{\circ}, 60^{\circ}\right] \\ \hat{r}_{osc,\ \text{Table Breakpoints}} &= \left[-0.112, -0.075, -0.056, -0.038, -0.028, -0.019, -0.009, \ldots\right. \\ &\qquad \left. 0, 0.009, 0.019, 0.028, 0.038, 0.056, 0.075, 0.112\right]\end{aligned} \tag{A.4}$$

A.3 Rotary Balance Wind Tunnel Testing

Rotary balance testing typically consists of measuring forces and moments on a model via a strain gauge balance while the entire model/balance assembly is rotated in a steady coning motion. Typically, the rotation axis is parallel to the free-stream tunnel

velocity, representing a steady velocity-vector roll. The independent variables are normally the angle of attack, sideslip angle, and rotation rate. Various control surface deflections and aircraft configurations are usually tested as well.

Similar to the forced oscillation test described in the previous section, wind-on and wind-off data are taken and subtracted to remove the mass and inertial effects. The data is also filtered to remove structural effects and averaged over multiple revolutions. The data provided to the analyst from the rotary balance test is normally one set of aerodynamic force and moment coefficients for each combination of the independent variables. These data represent the total aerodynamic forces and moments and must be manipulated to be used with an incremental aerodynamic model structure.

The incremental database was created by subtracting the zero-rate coefficient value (i.e., the static value) at a particular angle of attack and sideslip angle from the non-zero rate coefficient values at that same angle of attack and sideslip angle. In equation form, using rolling moment as an example, this process is simply

$$\Delta C_l\left(\alpha_i, \beta_j, \hat{\omega}_{ss}\right) = C_l\left(\alpha_i, \beta_j, \hat{\omega}_{ss}\right) - C_l\left(\alpha_i, \beta_j, \hat{\omega}_{ss} = 0\right) \tag{A.5}$$

Difficulties can arise with this method when there are asymmetries present in the static data. This topic was discussed in Section 4.2.1.

The independent variables used for this database were the angle of attack, sideslip angle, and nondimensional rotational rate. The breakpoints of the database are as follows:

$$\alpha_{\text{Table Breakpoints}} = \left[0^{\circ}, 4^{\circ}, 8^{\circ}, 10^{\circ}, 12^{\circ}, 14^{\circ}, 15^{\circ}, 16^{\circ}, 18^{\circ}, 20^{\circ}, 24^{\circ}, 26^{\circ}, 30^{\circ}, 35^{\circ}, \ldots \right.$$
$$\left. 40^{\circ}, 45^{\circ}, 50^{\circ}, 55^{\circ}, 60^{\circ}, 65^{\circ}, 70^{\circ}, 75^{\circ}, 80^{\circ}, 85^{\circ}, 90^{\circ} \right]$$
$$\beta_{\text{Table Breakpoints}} = \left[-45^{\circ}, -40^{\circ}, -35^{\circ}, -30^{\circ}, -25^{\circ}, -20^{\circ}, -15^{\circ}, -12^{\circ}, -8^{\circ}, -4^{\circ}, \ldots \right. \quad \text{(A.6)}$$
$$\left. 0^{\circ}, 4^{\circ}, 8^{\circ}, 12^{\circ}, 15^{\circ}, 20^{\circ}, 25^{\circ}, 30^{\circ}, 35^{\circ}, 40^{\circ}, 45^{\circ} \right]$$
$$\hat{\omega}_{ss,\ \text{Table Breakpoints}} = \left[-0.5, -0.3, -0.15, -0.05, 0, 0.05, 0.15, 0.3, 0.5 \right]$$

A.4 Free-Spin Test Data Post-Processing

The free-spin wind tunnel test technique was described in detail in Section 3.5. This section gives a detailed description of the post-processing of the digital and analog free-spin data.

A.4.1 Analog Data Processing

The only analog data of interest for this research was the wind tunnel velocity via a pitot-static probe located in the test section. The analog signal was measured at 1 Hz, but was sampled at 150 Hz in order to synchronize these data with the photogrammetry data. The resulting digitized signal was noisy, so a moving average was used to smooth these data. The result was a clean 1 Hz signal, which cannot be used directly with the 150 Hz photogrammetry data. A spline curve was fit to the beginning of each 1 second sample to create a smoothly varying signal. Figure A.4 shows the raw voltage signal, the moving average, and spline fit for the velocity signal from a free-spin test run.

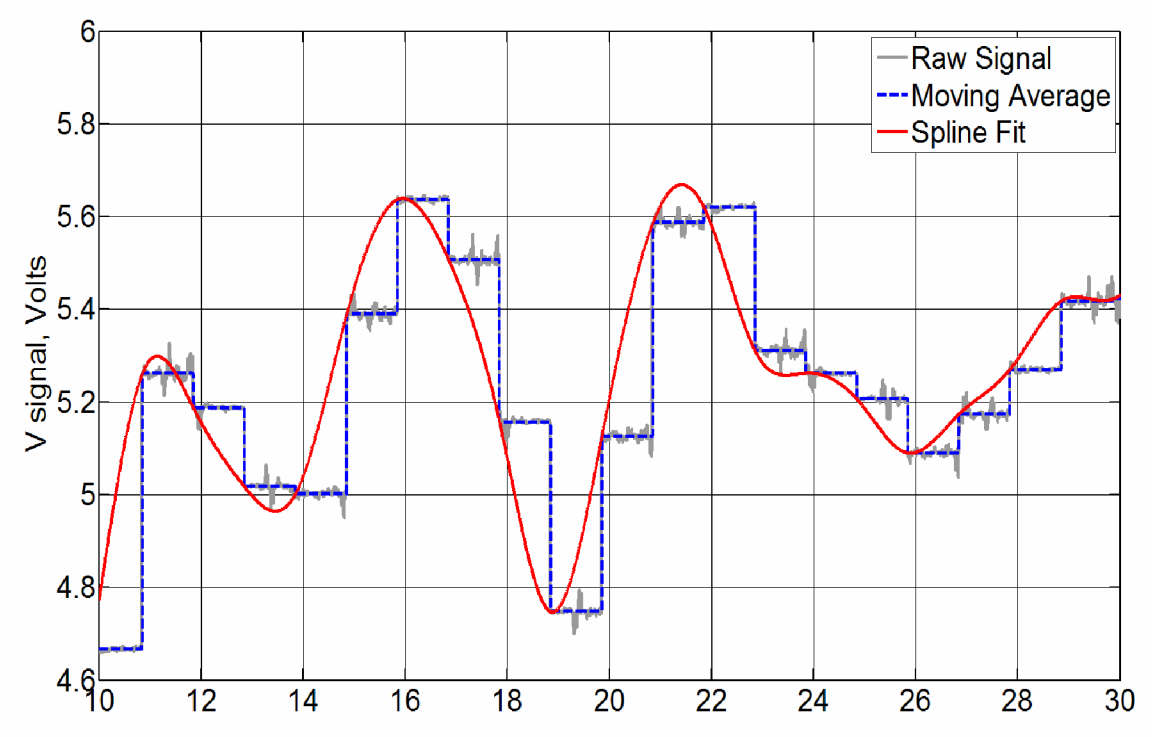

Figure A.4: Sample of analog velocity signal showing moving average and spline fit.

The voltage signal was then converted to the proper units using a calibrated conversion.

Finally, the velocity data from the tunnel pitot-static system was corrected based on a velocity anemometer survey conducted in the tunnel. A small scale factor and bias was needed to correct the pitot-static data, using the following relationship:

$$V_T = 1.0048 V_{p-s} - 0.9709 \qquad \text{(A.7)}$$

The maximum correction was about 2 feet per second.

A.4.2 Photogrammetry Data Processing

The following sections provide further detail of the post-processing that was performed on the photogrammetry position and orientation data.

A.4.2.1 Correction of Euler Angle Rotation Sequence

Due to technical difficulties with the photogrammetry data system software, the orientation angle data that was exported incorrectly assumed a 1-2-3 Euler angle rotation sequence, whereas the data was recorded using a 3-2-1 rotation sequence. For a variety of reasons, a timely fix of the software was not possible, and it was necessary to correct the orientation data. This was done prior to any smoothing or other processing of the data.

The first step in correcting the data was to compute the Direction Cosine Matrix (DCM), using the following equation, where 1, 2, and 3 represent the respective rotation angles.

$$DCM = \begin{bmatrix} \cos 3\cos 2 & \cos 3\sin 2\sin 1+\sin 3\cos 1 & -\cos 3\sin 2\cos 1+\sin 3\sin 1 \\ -\sin 3\cos 2 & -\sin 3\sin 2\sin 1+\cos 3\cos 1 & \sin 3\sin 2\cos 1+\cos 3\sin 1 \\ \sin 2 & -\cos 2\sin 1 & \cos 2\cos 1 \end{bmatrix} \quad \text{(A.8)}$$

(Note: 1, 2, and 3 are used here instead of ϕ , θ , and ψ to avoid confusion)

Recall that for any Euler angle rotation sequence, the DCM is the same regardless of the order of rotation. This fact was utilized to then back out what the 3-2-1 Euler angles were, using selected elements of the DCM. For a 3-2-1 rotation, the DCM is given by the following:

$$DCM = \begin{bmatrix} \cos\theta\cos\psi & \cos\theta\sin\psi & -\sin\theta \\ -\sin\psi\cos\phi+\sin\theta\cos\psi\sin\phi & \cos\psi\cos\phi+\sin\theta\sin\psi\sin\phi & \cos\theta\sin\phi \\ \sin\psi\sin\phi+\sin\theta\cos\psi\cos\phi & -\cos\psi\sin\phi+\sin\theta\sin\psi\cos\phi & \cos\theta\cos\phi \end{bmatrix} \quad \text{(A.9)}$$

From Equation(A.9), note that θ can be calculated using the (1,3) element of the DCM. Once θ is known, ϕ and ψ can be calculated using the (1,1), (1,2), and (3,3) elements of the DCM.

The above calculations are performed using inverse trigonometric functions, which present some challenges from a numerical standpoint. Specifically, the inverse sine function returns values on the interval $\left[-\pi/2, \pi/2\right]$ and the inverse cosine function is returns values on the interval $[0, \pi]$. This presents a problem since the desired interval for the yaw angle is $[0, 2\pi]$. This ambiguity can be resolved by using the fact that the derivative of the cosine function is the negative sine function. If the derivative of the cosine is negative, the angle is within the interval $[0, \pi]$ and conversely, if the derivative is positive, the angle is within the interval $[\pi, 2\pi]$. The sine and cosine of the yaw angle is present in the (1,1) and (1,2) elements of the DCM along with the cosine of θ, which is known.

A.4.2.2 Optimal Global Fourier Smoothing

Numerically differentiating noisy time series will amplify the noise in the data. For best results, the original time series should be smoothed. For this research, the entire time series is available for analysis so an optimal global Fourier smoothing algorithm[27] was used to remove the noise. This process essentially allows the analyst to remove all portions of a signal above a selected frequency. This process was implemented using SIDPAC functions in MATLAB and is described in Reference 27. For this research, the cutoff frequency was set to 7 Hz, the dynamically-scaled equivalent to 1 Hz at the full aircraft scale.

A.4.2.3 Numerical Differentiation

Even when using smoothed or filtered data, numerically differentiating time series can be problematic, especially when using the finite difference method. An alternative is to locally fit a second-order polynomial to the data which can be analytically differentiated. This process was implemented using SIDPAC functions in MATLAB and is described in Reference 27.

A.4.2.4 Body-Axis Angular Rates and Accelerations

The body-axis angular rates (p_b, q_b, r_b) can be calculated from the Euler angles and the Euler rates, using the following equations:

$$p_b = \dot{\phi} - \dot{\psi}\sin\theta \tag{A.10}$$

$$q_b = \dot{\theta}\cos\phi + \dot{\psi}\sin\phi\cos\theta \tag{A.11}$$

$$r_b = -\dot{\theta}\sin\phi + \dot{\psi}\cos\phi\cos\theta \tag{A.12}$$

Equations (A.10) - (A.12) can be analytically differentiated to obtain the body-axis angular accelerations, as shown below.

$$\dot{p}_b = \ddot{\phi} - \dot{\psi}\dot{\theta}\cos\theta - \ddot{\psi}\sin\theta \tag{A.13}$$

$$\dot{q}_b = \ddot{\theta}\cos\phi - \dot{\theta}\dot{\phi}\sin\phi + \dot{\psi}\left(\dot{\phi}\cos\phi\cos\theta - \dot{\theta}\sin\phi\sin\theta\right) + \ddot{\psi}\sin\phi\cos\theta \tag{A.14}$$

$$\dot{r}_b = -\ddot{\theta}\sin\phi - \dot{\theta}\dot{\phi}\cos\phi - \dot{\psi}\left(\dot{\phi}\sin\phi\cos\theta + \dot{\theta}\cos\phi\sin\theta\right) + \ddot{\psi}\cos\phi\cos\theta \tag{A.15}$$

A.4.2.5 Body-Axis Velocities and Accelerations

The body-axis velocities (*u, v, w*) can be calculated by summing together the model translation (obtained by numerically differentiating the position data) and the tunnel velocity. The tunnel velocity is assumed to be vertical, i.e. along the tunnel z-axis.

$$\mathbf{V} = L_{bT}\left(\mathbf{V}_T + \begin{bmatrix} \dot{X} \\ \dot{Y} \\ \dot{Z} \end{bmatrix}\right) \tag{A.16}$$

$$\mathbf{V} = L_{bT}\begin{bmatrix} \dot{X} \\ \dot{Y} \\ \dot{Z} + V_T \end{bmatrix} \tag{A.17}$$

Where L_{bT} is the transformation matrix for the 3-2-1 Euler angle rotation sequence from the wind tunnel reference frame to the aircraft body-axis frame, given by the following:

$$L_{bT} = \begin{bmatrix} 1 & 0 & 0 \\ 0 & \cos\phi & \sin\phi \\ 0 & -\sin\phi & \cos\phi \end{bmatrix}\begin{bmatrix} \cos\theta & 0 & -\sin\theta \\ 0 & 1 & 0 \\ \sin\theta & 0 & \cos\theta \end{bmatrix}\begin{bmatrix} \cos\psi & \sin\psi & 0 \\ -\sin\psi & \cos\psi & 0 \\ 0 & 0 & 1 \end{bmatrix} \tag{A.18}$$

$$L_{bT} = \begin{bmatrix} \cos\theta\cos\psi & \cos\theta\sin\psi & -\sin\theta \\ -\sin\psi\cos\phi + \sin\theta\cos\psi\sin\phi & \cos\psi\cos\phi + \sin\theta\sin\psi\sin\phi & \cos\theta\sin\phi \\ \sin\psi\sin\phi + \sin\theta\cos\psi\cos\phi & -\cos\psi\sin\phi + \sin\theta\sin\psi\cos\phi & \cos\theta\cos\phi \end{bmatrix} \tag{A.19}$$

Equation (A.19) can be analytically differentiated to obtain the body-axis accelerations, as shown below.

$$\dot{\mathbf{V}} = L_{bT}\begin{bmatrix} \ddot{X} \\ \ddot{Y} \\ \ddot{Z} + \dot{V}_T \end{bmatrix} + \dot{L}_{bT}\begin{bmatrix} \dot{X} \\ \dot{Y} \\ \dot{Z} + V_T \end{bmatrix} \tag{A.20}$$

The $\ddot{X}, \ddot{Y}, \ddot{Z}$, and $\dot{V}_T$ terms are calculated by numerical differentiation. The term $\dot{L}_{bT}$ can be calculated analytically, and for clarity is split into its component elements:

$$\dot{L}_{bT}(1,1) = -\dot{\psi}\sin\psi\cos\theta - \dot{\theta}\sin\theta\cos\psi \tag{A.21}$$

$$\dot{L}_{bT}(1,2) = \dot{\psi}\cos\psi\cos\theta - \dot{\theta}\sin\theta\sin\psi \tag{A.22}$$

$$\dot{L}_{bT}(1,3) = -\dot{\theta}\cos\theta \tag{A.23}$$

$$\dot{L}_{bT}(2,1) = \dot{\phi}\sin\phi\sin\psi - \dot{\psi}\cos\psi\cos\phi + \dot{\phi}\sin\theta\cos\phi\cos\psi - \dot{\psi}\sin\theta\sin\psi\sin\phi + \dot{\theta}\cos\theta\cos\psi\sin\phi \tag{A.24}$$

$$\dot{L}_{bT}(2,2) = -\dot{\phi}\sin\phi\cos\psi - \dot{\psi}\sin\psi\cos\phi + \dot{\phi}\sin\theta\cos\phi\sin\psi + \dot{\psi}\sin\theta\cos\psi\sin\phi + \dot{\theta}\cos\theta\sin\psi\sin\phi \tag{A.25}$$

$$\dot{L}_{bT}(2,3) = \dot{\phi}\cos\phi c\cos\theta - \dot{\theta}\sin\theta\sin\psi \tag{A.26}$$

$$\dot{L}_{bT}(3,1) = \dot{\phi}\cos\phi\sin\psi + \dot{\psi}\cos\psi\sin\phi - \dot{\phi}\sin\theta\sin\phi\cos\psi - \dot{\psi}\sin\theta\sin\psi\cos\phi + \dot{\theta}\cos\theta\cos\psi\cos\phi \tag{A.27}$$

$$\dot{L}_{bT}(3,2) = -\dot{\phi}\cos\phi\cos\psi + \dot{\psi}\sin\psi\sin\phi - \dot{\phi}\sin\theta\sin\phi\sin\psi + \dot{\psi}\sin\theta\cos\psi\cos\phi + \dot{\theta}\cos\theta\sin\psi\cos\phi \tag{A.28}$$

$$\dot{L}_{bT}(3,3) = -\dot{\phi}\sin\phi\cos\theta - \dot{\theta}\sin\theta\cos\phi \tag{A.29}$$

A.4.2.6 Wind Angles and Their Time Derivatives

The wind angles α and β and their time derivatives can be calculated directly from the body-axis velocities and accelerations.

$$\alpha = \tan^{-1}\frac{u_b}{w_b} \tag{A.30}$$

$$\beta = \sin^{-1}\frac{v_b}{|\mathbf{V}|} \tag{A.31}$$

$$\dot{\alpha} = -\frac{w_b\dot{u}_b - u_b\dot{w}_b}{w_b^{\,2} + u_b^{\,2}} \tag{A.32}$$

$$\dot{\beta} = \frac{|\mathbf{V}|\dot{v}_b - v_b|\dot{\mathbf{V}}|}{|\mathbf{V}|\sqrt{|\mathbf{V}|^2 - v_b^{\,2}}} \tag{A.33}$$

A.4.2.7 Aerodynamic Force and Moment Coefficients

The standard rigid-body equations of motion for an aircraft, assuming a flat, nonrotating earth, constant mass properties, and written in body-axes are given by

$$\mathbf{F} = m\dot{\mathbf{V}} + \boldsymbol{\omega} \times m\mathbf{V} \tag{A.34}$$

$$\mathbf{M} = \mathbf{I}\dot{\boldsymbol{\omega}} + \boldsymbol{\omega} \times \mathbf{I}\boldsymbol{\omega} \tag{A.35}$$

Where

$$\begin{aligned} \mathbf{V} &= \begin{bmatrix} u_b \\ v_b \\ w_b \end{bmatrix}, \quad \dot{\mathbf{V}} = \begin{bmatrix} \dot{u}_b \\ \dot{v}_b \\ \dot{w}_b \end{bmatrix} \\ \boldsymbol{\omega} &= \begin{bmatrix} p_b \\ q_b \\ r_b \end{bmatrix}, \quad \dot{\boldsymbol{\omega}} = \begin{bmatrix} \dot{p}_b \\ \dot{q}_b \\ \dot{r}_b \end{bmatrix} \\ \mathbf{I} &= \begin{bmatrix} I_{xx} & 0 & -I_{xz} \\ 0 & I_{yy} & 0 \\ -I_{xz} & 0 & I_{zz} \end{bmatrix} \end{aligned} \tag{A.36}$$

The right-hand side of Equations (A.34) and (A.35) are either measured or calculated quantities. The forces and moments on the left-hand side Equations (A.34) and (A.35) can be expressed in terms of nondimensional coefficients and gravity terms:

$$\mathbf{F} = \bar{q}S \begin{bmatrix} C_X \\ C_Y \\ C_Z \end{bmatrix} + mg \begin{bmatrix} -\sin\theta \\ \sin\phi\cos\theta \\ \cos\phi\cos\theta \end{bmatrix} \tag{A.37}$$

$$\mathbf{M} = \bar{q}S \begin{bmatrix} bC_l \\ \bar{c}C_m \\ bC_n \end{bmatrix} \tag{A.38}$$

Substituting Equations (A.37) and (A.38) into Equations (A.34) and (A.35) and solving for the aerodynamic coefficients yields the total aerodynamic coefficient acting on the body:

$$\begin{bmatrix} C_X \\ C_Y \\ C_Z \end{bmatrix} = \frac{1}{\bar{q}S}\left(m\dot{\mathbf{V}} + \boldsymbol{\omega} \times m\mathbf{V} - mg \begin{bmatrix} -\sin\theta \\ \sin\phi\cos\theta \\ \cos\phi\cos\theta \end{bmatrix} \right) \tag{A.39}$$

$$\begin{bmatrix} C_l \\ C_m \\ C_n \end{bmatrix} = \frac{1}{\bar{q}S} \begin{bmatrix} \frac{1}{b} \\ \frac{1}{\bar{c}} \\ \frac{1}{b} \end{bmatrix} \left(\mathbf{I}\dot{\boldsymbol{\omega}} + \boldsymbol{\omega} \times \mathbf{I}\boldsymbol{\omega} \right) \tag{A.40}$$

REFERENCES

[1] Anon., "Safety spotlight shifts on to loss of control", *Flight International*, January 11, 1995.

[2] "Dynamics Modeling of Large Transports for Upset Conditions", final report for NASA contract NAS1-00106, Task 1003, October 31, 2002.

[3] "Aerodynamic Modeling of Large Transports for Upset Conditions", Stage 2 EURS Progress Report for NAS1-00106 Task 1010, October 31, 2003.

[4] "Aerodynamic Modeling of Large Transports for Upset Conditions", 2004 EURS Progress Report for NAS1-00106, November 3, 2004.

[5] Foster, J. V., Cunningham, K., Fremaux, C. M., Shah, G. H., Stewart, E. C., Rivers, R. A., Wilborn, J. E., Gato, W., "Dynamics Modeling and Simulation of Large Transport Airplanes in Upset Conditions", AIAA 2008-5933, *AIAA Guidance, Navigation, and Control Conference and Exhibit*, San Francisco, CA, August 2005.

[6] Anon., "Burning issue", *Flight International*, April 4, 2006.

[7] Russell, P. D., Pardee, J. J., "Joint Safety Analysis Team – Loss of Control: Results and Analysis Final Report", Federal Aviation Administration, Commercial Aviation Safety Team, Washington, D.C., 2000.

[8] Wilborn, J. E., "An Analysis of Commercial Transport Aircraft Loss-of-Control Accidents and Intervention Strategies," final report for NASA contract NAS1-20341, Task 10, June 29, 2001.

[9] Wilborn,, J. E., and Foster, J. V., " Defining Commercial Transport Loss-of-Control: A Quantitative Approach," *AIAA Atmospheric Flight Mechanics Conference*, AIAA 2004-4811, Providence, RI, August 2004.

[10] Cunningham, K., Foster, J. V., Shah, G. H., Stewart, E. C., Rivers, R. A., Wilborn, J. E., and Gato, W., "Simulation Study of a Commercial Transport Airplane During Stall and Post-Stall Flight," *World Aviation Congress & Display*, SAE 2004-01-3100, Reno, NV, November 2004.

[11] Murch, A. M., Foster, J. V., "Recent NASA Research on Aerodynamic Modeling of Post-Stall and Spin Dynamics of Large Transport Airplanes", AIAA-2007-0463, *45th AIAA Aerospace Sciences Meeting & Exhibit*, Reno, NV, January 2007.

[12] Shah, G. H., Cunningham, K. Foster, J. V., Fremaux, C. M. Stewart, E. C., Wilborn, J. E., Gato, W., and Pratt, D. W., "Wind-Tunnel Investigation of Commercial Transport Aircraft Aerodynamics at Extreme Flight Conditions," *World Aviation Congress & Display*, SAE 2002-01-2912, Phoenix, AZ, November 2002.

[13] Kramer, B. R., "Experimental Evaluation of Superposition Techniques Applied to Dynamic Aerodynamics (Invited)," *40th AIAA Aerospace Sciences Meeting & Exhibit*, Reno, NV, January 2002.

[14] Kay, J.; "Acquiring and Modeling Unsteady Aerodynamic Characteristics," *AIAA Atmospheric Flight Mechanics Conference*, AIAA 200-3907, Denver, CO, August 2000.

[15] Dickes, E. G., Ralston, J. N., and Lawson, K., "Application Of Large-Angle Data For Flight Simulation," *AIAA Modeling and Simulation Conference and Exhibit*, AIAA 2000-4584, Denver, CO, August 2000.

[16] O'Connor, C. J., Ralston, J. N., and Fitzgerald, T., "Evaluation Of The NAWC/AD F/A-18 C/D Simulation Including Database Coverage And Dynamic Data Implementation Techniques," *AIAA Atmospheric Flight Mechanics Conference*, AIAA-1996-3365-874, San Diego, CA, July 1996.

[17] Ogburn, M. E., Nguyen, L. T., and Hoffler, K. D., "Modeling of Large-Amplitude High-Angle-Of-Attack Maneuvers," *AIAA Atmospheric Flight Mechanics Conference*, AIAA 88-4357, Minneapolis, MN, August 1988.

[18] Chambers, J. R., and Stough, H. P. III, "Summary of NASA Stall/Spin Research for General Aviation Configurations," *AIAA General Aviation Technology Conference*, AIAA 86-2597, Anaheim, CA, 1986.

[19] Brandon, J. M., Foster, J. V., Shah, G. H., Gato, W., and Wilborn, J. E., "Comparison of Rolling Moment Characteristics During Roll Oscillations for a Low and a High Aspect Ratio Configuration," *AIAA Atmospheric Flight Mechanics Conference*, AIAA-2004-5273, Providence, RI, August 2004.

[20] Jamarillo, P. T., Ralston, J., "Simulation of the F/A-18D 'falling leaf'," *AIAA Atmospheric Flight Mechanics Conference*, AIAA 96-3371, San Diego, CA, July 1996.

[21] Birhle, W. Jr., and Barnhart, B., "Spin Prediction Techniques," *Journal of Aircraft*, Vol. 20, No. 2, February 1983.

[22] Kalviste, J., "Use of Rotary Balance and Forced Oscillation Test Data in a Six Degrees of Freedom Simulation," *AIAA Atmospheric Flight Mechanics Conference*, AIAA 82-1364, San Diego, CA, August 1982.

[23] Polhamus, E. C., "Effect of Flow Incidence and Reynolds Number on Low-Speed Aerodynamic Characteristics of several noncircular cylinders with applications to directional stability and spinning," NACA TN 4176, January 1958.

[24] Polhamus, E. C., "A Survey of Reynolds Number and Wing Geometry Effects on Lift Characteristics in the Low Speed Stall Region," NASA Contractor Report 4745, June 1996.

[25] Jordan, T. L., Langford, W. M., Belcastro, Christine M., Foster, J. M., Shah, G. H., Howland, G., Kidd, R., "Development of a Dynamically Scaled Generic Transport Model Testbed for Flight Research Experiments", *AUVSI Unmanned Systems North America 2004*, AUVSI, Arlington, VA, 2004

[26] Jordan, T. L., Langford, W. M., Hill, J. S., "Airborne Subscale Transport Aircraft Research Testbed: Aircraft Model Development," *AIAA Guidance, Navigation, and Control Conference and Exhibit*, AIAA 2005-6432, San Francisco, CA, August 2005.

[27] Klein, V., Morelli, E. A., *Aircraft System Identification: Theory and Practice*, AIAA Education Series, AIAA, Reston, VA, 2006.